UNIVERSITY OF SOUTHAMPTON

Space charge in XLPE under dc and ac electric stress

by

Yeng Leong Chong

A thesis submitted for the degree of
Doctor of Philosophy.

School of Electronics and Computer Science,
University of Southampton

June, 2005

UNIVERSITY OF SOUTHAMPTON
ABSTRACT
FACULTY OF ENGINEERING, SCIENCE AND MATHEMATICS
SCHOOL OF ELECTRONICS AND COMPUTER SCIENCE

Doctor of Philosophy
Space charge in XLPE under dc and ac electric stress
By Yeng Leong Chong

There are growing evidences that space charge plays an important role in electrical performance of polymeric high voltage cables. The main objectives of the present work were to evaluate the influence of various factors such as heat treatment (degassing), temperature, electric stress level and frequency on space charge characteristics. Both the Laser Induced Pressure Pulse (LIPP) and the Pulsed Electroacoustic (PEA) methods were used to measure space charge in cross-linked polyethylene (XLPE) samples.

The effect of heat treatment on space charge in XLPE under dc electric stress was conducted. The results showed that more volatile crosslinked by-products can be removed from the sample by increasing the length and temperature of degassing and that it is also easier to remove the by-products from thinner samples.

Degassing also has another effect on the material in that its morphological structure is changed. Results from the differential scanning calorimetry (DSC) and the transmission electron microscope (TEM) indicate changes in the morphological structure when degassing parameters change. It was also found that the threshold stresses at which space charge initiates and space charge evolution are highly dependent on samples' by-product concentrations while changes in the morphological structure have only minimal impact.

The testing temperature, apart from affecting the threshold stresses at which space charge initiates, also increases charge energy and mobility which generally result in less space charge trapped in the samples. It was found that at elevated temperature positive charge propagation enhances which eventually result in the space distribution being dominated by positive charge and takes the same form regardless of whether the sample is degassed or as-received.

The experiment on XLPE samples subjected to ac electric stress shows that the amount of charge trapped in samples subjected to ac electric stress is always much smaller than when subjected to dc electric stress of the same magnitude. It was also demonstrated that frequencies and applied stress of the ac electric stress affect the amount of charge trapped in a sample.

Deep traps were generated in samples that were electrically stressed under ac condition. The frequencies and magnitude of the applied ac electric stress seems to have a definitive effect on the depth of the traps. It was found that the higher the frequencies and/or magnitude of the ac stress, the deeper the trap depth.

The effect of ac ageing on space charge in XLPE under dc electric stress was also investigated. It was discovered that the higher the frequency and/or magnitude of the pre-aged ac stress, the more dominant the positive charge which in some cases led to formation of positive packet charge that propagates into the samples. The experiment also confirmed that ac electrical ageing causes the formation of deeper traps particular for negative charge carriers.

Contents

Appendix C   Ci

.

List of figures

Principle notations

ΔT	Electric pulse duration (PEA)
A	Surface area of measurement
c, u	Velocity of sound
C_a	Capacitance of the measurement circuit,
C_b	Capacitance of blocking capacitor,
d	Sample thickness
D	Coefficient of diffusion
D_0	Temperature independent constant
ε_0	Permittivity of free space
ε_r	Relative permittivity
$e_p(t)$	High voltage narrow electric pulse (PEA)
$E(z,t)$	Electric stress distribution
$E_{applied}$	Applied electric stress
E_{cal}	Electric stress for calibration
$E_e(x)$	Effective electric stress
$E_c(x)$	Electric stress from space charge
eV	Electron volt
$G(\varepsilon)$	Coefficient that depends on the relationship between the permittivity and the pressure wave
$I_{space}(z,t)$	Current output from the testing sample
$I_{cal}(0,t)$	Calibrated current at the target interface
k	Boltzman constant
$n(x,t)$	Concentration of by-products at location x and time t
N	Laser shot number
p_0	is the maximum amplitude of the pressure wave at the target interface
$p_z(z)$	is the amplitude of the pressure wave at location z
$p(z,t)$	Pressure wave profile
$\rho(z)$	Space charge density distribution

$\rho_{accumulated}(x)$ Accumulated space charge distribution

$\rho_{calibrate}(x)$ Space charge distribution for calibration

$\rho_{fast}(x)$ Fast charge distribution

$\rho_{no-charge}(x)$ Volt-on space charge distribution with no charge

$\rho_{volt-off}(x)$ Volt-off space charge distribution

$\rho_{volt-on}(x)$ Volt-on space charge distribution

ρ The density of liquid

Q Integration of charge density

Q_d Activation energy for diffusion

δ The amount of mechanical displacement carried by the pressure pulse

R_a Resistance of the measurement circuit,

S Electrode area

$\tau(z)$ Width of the pressure wave at location z

τ_{rise} Typical rise time of the LIPP current pulse

u_{al} Speed of acoustic in the aluminum

u_{sa} Speed of acoustic in the sample

V_s Voltage measurement by the oscillscope

ω Angular frequency

χ Pressure independent compressibility of the sample

z Distance through the testing sample

$z_f(t)$ Position of the pressure wave front at time t

Ω Ohms (Resistance)

Abbreviations

Ac	Alternating current
Dc	Direct current
DCP	Dicumyl peroxide
DSC	Differential scanning calorimetry
FTIR	Fourier transform infra-rd
GPIB	General purpose interface bus
H_2O_2	Hydrogen peroxide
HV	High voltage
Hz	Hertz
LDPE	Low density polyethylene
LIMM	Laser intensity modulation method
LIPP	Laser induced pressure pulse
PE	Polyethylene
PEA	Pulsed Electroacoustic method
SF_6	Sulfur Hexafluoride
SNR	Signal to noise ratio
TPM	Thermal Pulse method
TSC	Thermally stimulated current method
TSM	Thermal Step method
V	Voltage
XLPE	Crosslinked polyethylene

Publications

1) Y.L. Chong, Y.F.F. Ho and G. Chen, "Automation of space charge measurement by using LIPP technique.", In Proceedings Of The 2nd International Conference On Insulation Condition Monitoring Of Electrical Plants, 2003, pp. 168-171.

2) Y.F.F. Ho, Y.L. Chong and G. Chen, "Effect of the length of degassing period on the space charge dynamics in XLPE insulation under dc stressing condition.", In Proceedings Of The 2nd International Conference On Insulation Condition Monitoring Of Electrical Plants, 2003, pp. 160-163.

3) Y.L. Chong, Y.F.F. Ho and G. Chen, "Optimization of the aluminium target thickness on the space charge measurement using LIPP technique.", In Proceedings Of IEEE Conference On Electrical Insulation And Dielectric Phenomena, 2003, pp. 237-240.

4) Y.F.F. Ho, Y.L. Chong and G. Chen, "Temperature effect on the space charge characteristics in as-received and degassed XLPE insulation under dc stressing condition.", In Proceedings Of IEEE Conference On Electrical Insulation And Dielectric Phenomena, 2003, pp. 241-244.

5) Y.L. Chong, Y.F.F. Ho and G. Chen, "The effect of degassing on morphology and space charge.", In Proceedings Of IEEE Conference On Solid Dielectrics, 2004, pp.162-165

6) Y.L. Chong, H. Miyake, Y. Tanaka, T. Takada, H. Nakama and G. Chen, "Space charge in polyethylene under ac electric stress using the pulsed eletroacoustic method.", In Proceedings Of IEEE Conference On Electrical Insulation And Dielectric Phenomena, 2004, pp. 77-80.

7) Y.L. Chong, G. Chen, H. Miyake, Y. Tanaka and T. Takada, "Effect of ac ageing on space charge evolution in XLPE.", In Proceedings Of IEEE Conference On Electrical Insulation And Dielectric Phenomena, 2004, pp. 81-84.

8) Y.L. Chong, G. Chen, I.L. Hoiser, A.S. Vaughan and Y.F.F. Ho, "Heat treatment of cross-linked polyethylene and its effect on morphology and space charge evolution.", IEEE Transactions On Dielectrics And Electrical Insulation (Accepted)

Acknowledgement

Completion of this thesis would not have been possible if I were to do everything without help. A lot of people have contributed to this work and without them, I, most definitely, wouldn't be where I am now. I would like to take this opportunity express my gratitude to them.

First and foremost, I would like to sincerely thank Dr. George Chen, my project supervisor, for his valuable advices, encouragement and patience throughout the project. I would also like to thank my ex-colleague, Dr. Fred Ho for explaining the principle of the LIPP system and giving me a good head start to the project.

There are lot of people from Musashi Institute of Technology in Japan whom I wished to express my heart felt gratitude, none more so than Professor Yasuhiro Tanaka and Dr. Hiroaki Miyake for their warm hospitality, advices and engineering support during my stay in Japan. My sincere appreciation also goes to Mr. Kohei Matsui, my exchange student counterpart, for designing a high resolution PEA which helped me immensely in this project. I would also like to express my heartfelt thanks to Professor Tatsuo Takada for unselfishly imparting his brilliant engineering knowledge and Ms. Maki Hayashi for handling of all the administrative work necessary for the student exchange programme.

Dr. Ian Hosier and Dr. Alun Vaughan's help and advice with the TEM micrographs along with engineering support from Mr. Michael Smith, Mr. Stephen Harrison, Mr. Neil Palmer and Mr. Richard Howells were also gratefully acknowledged.

I believe that opportunities are as important as hard work. For that, I owe a great deal to the late Professor Tony Davies for offering me the opportunity to embark in this research.

I would also like to thank my family- my parents Ah Chye Chong and Nai Ling Wong and my elder brother Yeng Keat Chong, for being extremely supportive and understanding throughout my studies. Equally important are my friends- Mr. Chek Meng Tan, Mr. Tack Boon Yee, Mr. Ryan Jong and Mr. Paul Lee for being there for me whenever I am down, disappointed and depressed. Finally, I would like to thank my confidant- Miss Julie Leong for her introduction into my life has brought me memories which I will cherish and treasure for years to come.

1   Introduction

1.1   Background

Electrical power from power plants to consumers is transmitted at very high voltages. This is especially important for long distance power transmission where copper losses become significant. While there are advantages of transmitting electrical power at high voltages, there are however numerous practical factors that limit the voltage level. One such factor is imposed by the transmission media- overhead lines and underground cables.

Overhead lines have been preferred over underground cables for transmitting large amount of electrical powers. This is because the cost of installing an underground cable system averages about 10 times more than that of a overhead lines system of the same rated capacity [1].

The high cost of underground system is attributed to various reasons. One of the reasons is because the cost of manufacturing underground cables is much higher than overhead lines since the latter does not require any additional insulating medium. In addition, the installation process of an underground system, which involves digging a trench and jointing the cables, is much more complex and thus more expensive than for an overhead system [1].

The cost of maintenance for an underground system is also considerably higher. With an overhead line, it is relatively quicker and easier to locate and repair faults. Therefore, it is possible to restore the line back to service in a matter of a few hours. It will, however, be very much less so for a cable since it is buried underground. In extreme cases, the cable maybe out of service for weeks.

Since the cable is buried underground, it is to all intents and purposes placed in a thermal blanket. As such, underground cables have lower thermal ratings due to lower heat loss to surroundings and melting temperature of insulation when compared to overhead lines.

Despite all the advantages of overhead transmission system over underground system, the latter is still preferred in certain instances. One such example is in densely populated urban and suburban areas. This is because the cost of purchasing land in order to build pylons to support the overhead lines has increased dramatically in recent years, hence making overhead transmission system prohibitively expensive.

Underground systems are also used where circumstances dictate that the installation of overhead line would not be possible, such as in the vicinity of airports and across wide water areas. Furthermore, underground system has relatively minor aesthetic impact on our living environment and is therefore used in areas of particular environmental sensitivity, such as national parks.

Apart from the economical and environmental reasons, the underground system does have one technical advantage over their overhead counterparts. With it being totally enclosed, it is not exposed to environmental conditions and all the detrimental factors associated with it, such as wind and direct lightning strikes.

1.2   Development of underground cables

When Edison and Ferranti first used underground power transmission system in the 1880's, the cables used were solid copper rods, insulated with jute wrapping. Currently, there are two predominant types of solid insulation used for underground cables, namely taped paper/oil and polymeric. Other more specialised types of insulation including compressed SF_6 gas and superconducting cryogenic cables.

In recent years the traditional paper/oil insulated cables are being replaced by their polymeric insulated counterpart as the preferred type for underground high voltage power transmission. There are various kinds of polymeric materials, but crosslinked polyethylene (XLPE) is most widely used in cable industry.

Polyethylene was first produced in 1936 and is now one of the cheapest and most widely used plastics [2]. In the 1940's attempts were made to use low density polyethylene as an insulating material for power cables but it was not until the late

1950's and early 1960's that the use of polyethylene as insulation for power distribution applications became established.

The advantages of polyethylene insulation systems over the paper/oil insulation systems are their lower manufacturing cost, ease of installation and handling , high dielectric strength of up to 10^9 V/m , high electrical resistivity (>10^{16} Ωm) and low dielectric loss factor (tan δ = 0.0001 to 0.001) [1]. They also have good physical properties such as resistance to cracking and good moisture resistance. However, with the average operating temperature of underground cables being up to 90 °C and the maximum rated temperature of polyethylene being only 70 °C, the sustained current rating, overload and short-circuit temperatures of this kind of underground cables system are limited.

In the 1960's, the temperature stability was improved by converting the polyethylene into crosslinked polyethylene (XLPE). This type of insulation has improved physical properties over the uncrosslinked type, while the electrical properties were reported to be unaffected [3]. XLPE, which can operate continuously at a maximum temperature of 90 °C, is now the most widely accepted polymeric material for cable manufacturing industry.

1.3   Space charge in polymeric insulation

The development of polymeric insulated cables for high voltage power transmission has not been without problems. Due to imperfection in manufacturing, its premature failure rate was reported to be as high as 20 failures for every 100 kilometres of cable per year [4]. While polyethylene cables are widely accepted at voltages of 60 kV and 132 kV, at extra high voltages such as 230 kV to 750 kV the insulation is still predominately paper/oil.

Studies have shown that almost three quarters of cables that have failed in their first few years of service were caused by some sort of internal defects [5]. In order to reduce the failure rate of the cables, the quality of polymer used to make the cable and

the care and cleanliness with which the cable is manufactured are of paramount importance [6, 7].

While there are many reasons which lead to premature failures of the insulation, there has been an increasing belief that trapped charges, also known as "space charges" play an important role in ageing of polymer.

Space charge is the result of trapped or low mobility charges within the insulation bulk when the polymeric insulating material is subjected to high electric stress for a certain period of time. This causes localised electric stress enhancement beyond the electric breakdown strength, which leads to further degradation of the insulating material and eventually premature failure of the cable at an applied electric stress well below its intrinsic breakdown strength.

In recent years, significant effort has been devoted on investigating the formation and evolution of space charge within the bulk of insulating material when subjected to high electric stress. Two of the most commonly used techniques in space charge measurement are the Pulsed Electroacoustic (PEA) and the Laser Induced Pressure Pulse (LIPP). These techniques have been reported to have good spatial resolution of the concentration of space charge and being non-destructive to the insulating material being tested.

2   Space charge in polyethylene and crosslinked polyethylene

2.1   Introduction

Polyethylene (PE) is an organic chemical, based upon carbon and hydrogen elements. It is synthesised through the process of polymerisation whereby ethylene gas molecules are linked in a chain to form a polymer. The polymer is named by adding the prefix 'poly' to the name of the monomer from which it is derived and hence polyethylene from ethylene [8]. Ethylene can be made from ethane or propane extracted from natural gas, naphtha or atmospheric or even directly from crude oil itself [9].

In principle, ethylene can be made practically from any source of hydrocarbon. However, impurity content is a very important consideration, especially in the production of cable grade polymers. For example, ethylene made from extracts of natural gas produces very high grade ethylene with very few impurities and would hence be idea for manufacturing cable grade polymer if not for its high cost.

As mention earlier, polymerisation is the process whereby ethylene gas molecules are linked together to produce polyethylene chains. There are two principle processes for polymerisation namely addition and step growth. Step growth polymerisation describes the process where smaller molecules are linked together to form larger molecules. These larger molecules can then link further monomer or polymer molecules. Addition polymerisation describes the process where the polymer chain is formed by successive addition of monomer units onto the end of the chain. This type of polymerisation process is employed in the production of polyethylene.

2.2   Crosslinked polyethylene

The main drawback of polyethylene as an electrical insulation for underground cables is its upper operational temperature of about 70 $^{\circ}$C. This constraint has limited the use of polyethylene as insulation for power transmission cables, which may operate at temperatures above 70 $^{\circ}$C. To remove this constraint, polyethylene can be converted

into crosslinked polyethylene. Crosslinking is the process whereby the polymer structure is modified through the formation of chemical bonds between the polymer chains. Not only can crosslinked polyethylene operate at a maximum of 90 °C, it also has better mechanical and chemical properties as compared to its uncrosslinked counterpart.

Crosslinked polyethylene (XLPE) can be produced either by chemical reaction or through ionizing radiation. It is however not practical to crosslink thick insulation with the latter due to the expensive equipment and elaborate radiation shielding required for such a process. Furthermore, using radiation to form the crosslinks will cause bond scissions of the polymer chains, which themselves do not form crosslinks and hence weaken the polymer.

The most common method of chemical crosslinking is to trigger a thermally activated catalyst by subjecting the polymer to high temperatures. Dicumyl peroxide is the most widely used catalyst in the cable industry to give fast crosslinking without pre-curing in the extruder. This peroxide remains inactive at the cable insulation extrusion temperature (130-150 °C), but decomposes to initiate the crosslinking reaction at a temperature typically around 180 °C.

The electrical properties of the polymer were reported to remain relatively unaltered by the crosslinking process [3]. On the other hand, there are also reports that the crosslinking could act as localised charge trapping centres [10]. The additives and by-products of the crosslinking reaction will act as impurities and significantly affect the electrical properties of the insulation.

2.3   Structure and morphology of polymers

Generally, polymers can be classified into 3 categories, namely elastomers, thermosets and thermoplastics [11].

Elastomers are crosslinked rubbery polymers that can be stretched and rapidly recover their original state when the applied force is released. This is attributed to its molecular structure in which the network is of low crosslink density

On the other hand, thermosets are rigid polymers in which chain motion is greatly restricted by a high degree of crosslinking. Thermosets are intractable once formed and degrade under application of sufficient amount of heat.

Of particular interest to this project are thermoplastics; PE falls into this group of polymer. Thermoplastics are linear or branched polymers which melt upon application of heat. They generally do not crystallize upon cooling to the solid state. For crystallization to occur the polymer molecules must be able to adopt an ordered configuration in which adjacent chains lie parallel to one another. This, however, requires that, in the liquid of molten state, the molecular chains are ordered and are capable of relative motion to one another. Those which do not crystallise completely invariably form semi-crystalline material with both crystalline and amorphous regions.

The crystalline phases of semi-crystalline polymers are characterised by their melting temperature while the amorphous phases are characterized by their glass transition temperature. The melting temperature is the temperature at which the solid polymer changes to the liquid state. The glass transition temperature is the temperature at which the polymer changes from the hard glassy state to the soft rubbery state. This transition corresponds to the onset of bond rotation along the main chain.

The structural ordering in a solid polymer exists over a wide range of dimensional levels. They can be loosely classified into three levels, the lowest being the regularity of the molecular chain. The intermediate level is that of a single crystal known as lamella, while the highest in the hierarchy are poly-crystalline aggregates known as spherulites [12].

2.4   Charge transportation and trapping in PE and XLPE

Since this project concerns space charge formation and evolution in XLPE samples, it is, therefore, essential to have some basic concepts regarding the possible mechanisms of space charge formation and transportation.

There are several physical processes that need to be considered in the study of space charge formation and transportation in XLPE. They consist of injection and extraction of electrons or holes at the polymer/semicon electrode interface, ionisation of crosslinked by-products or additives in the polymer, hopping/tunnelling and trapping of charge within the polymer.

Heterocharge and homocharge are terms often used to describe the nature of space charge. Heterocharge refers to charge of the opposite polarity to the adjacent electrode while homocharge refers to charge of same polarity.

Heterocharge   Homocharge
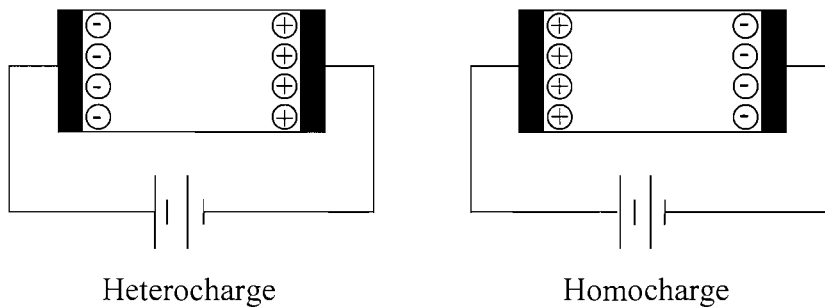
Figure 2.1   Heterocharge and homocharge

When an insulating material is subjected to an electric field, small molecules may be ionised and dissociated species will migrate towards the electrode with the opposite polarity. Such a process usually produces heterocharge which increases the stress at the electrode interface but reduces the electric stress in the insulating bulk.

On the other hand, homocharge is normally formed by trapping of the injected and/or extraction of charge near the electrodes. Homocharge, generally, results in reduced interfacial stress but enhanced bulk stress.

8

2.4.1 Charges at electrode

The nature of the electrode interface plays a vital role in the electrical behaviour of the dielectric material [13]. The energy equilibrium of the contact will be of paramount importance in determining whether the conduction process will be electrode or bulk limited [14].

In the case of a XLPE insulated underground cable, semiconducting screens or semicons are normally used to provide an equipotential surface on both sides of the insulation, eliminating any electric discharge arising from air gaps adjacent to the cable insulation. Without the semicon, mismatch between coefficient of thermal expansion for the conductor and insulator will result in the formation of air gaps when a cable experiences loading cycles.

Depending on the nature of the semicon/polymer interface contact, charge will transfer across the interface even without the application of an external electric stress [15]. This charge transfer at the interface of the electrode occurs by either Schottky injection or Fowler-Nordheim tunnelling [16].

Electrons can gain enough energy to literally 'hop' over the potential barrier at the interface when subjected to thermal excitation. This is known as the Schottky injection process [17]. On the other hand, since electrons exhibit a particle-wave duality, there is a finite possibility of them tunnelling through the potential barrier despite not having sufficient energy to surmount it. This is known as the Fowler-Nordheim tunnelling process. Fowler-Nordheim tunnelling is a quantum mechanical effect and is dependent on the width of the potential barrier.

Studies have shown that conduction and emission of charge in PE are dominantly electrons; not ions [5]. In other words, injection of electrons at the cathode and extraction of electrons at the anode are the main mechanism normally used for charge emission in PE. This is however not necessarily the case for all polymers as studies by Ieda [5] suggest that some polymers may emit and conduct holes across the electrode interface. It must be stressed that, determining the type of charge carriers is

fraught with complexities due to the complex physical and chemical structure of polymer.

Charge injection at polymer/semicon interface can also be affected by surface states. Surface state is the result of physical imperfections such as broken bonds, oxidation products and additives. These imperfections may lead to the formation of trap or donor states at the electrode interface.

2.4.2 Charges in bulk

As mentioned before, the XLPE used for cable insulation contains impurities such as catalysts, antioxidants, voltage stabilizers, crosslinking agents and by-products from the production process [18]. Under the application of a high electric field, these impurities can be dissociated into ion pairs- positive and negative ions. These ions will then migrate to the electrode of the opposite polarity; that is negative ions or electrons will move to the anode while positive ions will move to the cathode.

The charge movement within the insulating bulk is greatly affected by the localised states. Localised states are formed as a result of various physical attributes such as broken bonds within the crystalline structure, chain branches, dislocations foreign particles, oxidation products, polarised states, crosslinking impurities and additives [13, 19-22]. These localised states will act as traps to charge carriers at energies below the conduction band of the polymer. Generally, traps for electrons are known as acceptors while traps for holes are known as donors. There are traps that may act as recombination centres by trapping for both electrons and holes.

These traps can be broadly classified into two groups based on their depths; shallow and deep. The depth of a trap is defined as the energy required to liberate the trapped charge. Shallow traps are energetically located in the region of 0.1 to 0.3 eV below the conduction band. Deep traps are energetically located at 0.8 to 1.4 eV below the conduction band. The concentration of shallow traps has been found to be in the region of 10^{18} traps/cm^3, significantly higher than deep traps which is the in the region of 10^{14} traps/cm^3 [5, 10].

(a)

With electric
stress application

$-eEx$

Bottom of
conduction band

$\Delta \delta$

Without
electric
stress

D

trap

Reduced
potential barrier

(b)

hopping process   trap

Electrode   Dielectric   Electrode
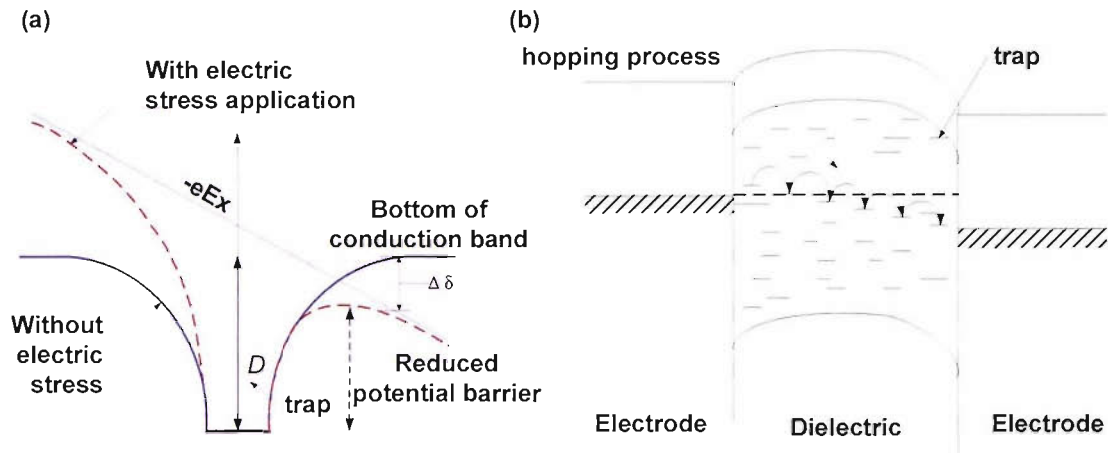
Figure 2.2 Schematic diagrams of the (a) Poole-Frenkel effect and
(b) hopping process in the dielectric material

An occupied electron trap can be viewed in term of an ideal energy diagram called the potential well. The slope of the bend in the walls will depend on the force of attraction between the trap and the electron according to Coulomb's Law. Referring to figure 2.2(a), the trap depth 'D' below the conduction band can be considered to be equal to the barrier height inhibiting the movement of the electrons, which is therefore equal to the energy required for the electron to be liberated from the trap.

From figure 2.2(a), it can be seen that the electric stress has had the effect of reducing the height of the potential barrier. This is known as the Poole-Frenkel effect. It is noteworthy that the barrier width has also been reduced by the electric stress. This will also help promote charge tunnelling effect (only at high fields). Hence the Poole-Frenkel effect increases probabilities of charge tunnelling and hopping. Figure 2.2(b) illustrates the hopping process of a charge under the influence of electric stress.

2.5   Conclusion

This chapter provided some basic background on polyethylene and crosslinked polyethylene. The advantages and disadvantages of PE and XLPE are also highlighted. Finally, some fundamental concepts of space charge mechanism are reviewed.

3   Laser Induced Pressure Pulse Technique

3.1   Introduction

Several methods have been developed in an attempt to study space charge within solid insulation. There are indirect methods such as measuring the current and voltage in external circuits [23]. There is also the simple but destructive method of cutting the solid insulation and measuring the charge in each slice of the material. Other destructive methods include the field probe techniques [24] and diffusion processes [25, 26].

However, to have a better understanding of space charge dynamics, direct and non-destructive methods of quantitively measuring space charge are required. While methods like the laser intensity modulated [27, 28] and thermal pulse/step method [29-31] are non-destructive, they deplete the sample of its trapped charges. There are, of course, methods which are non-destructive and do not deplete the sample of its trapped charge. They include electron spin resonance [32], stark spectroscopy [33], Kerr electro-optic field mapping [34, 35] and optical molecular probe technique [36].

One of the techniques of space charge measurement used in this study is the Laser Induced pressure pulse technique (LIPP). This technique, developed by Laurenceau et al [37] in 1977, is a laser based pressure wave propagation system (PWP). This non-destructive method, which directly measures the internal charge distribution of dielectrics, has been used and reviewed by many workers [12, 38-68].

This chapter reviews the basic principle of the LIPP system that was purchased and modified at the University of Southampton. This LIPP system can be used to measure space charge distribution of insulating material under both dc and 50 Hz ac conditions.

3.2   Principle of dc LIPP system

The main idea of PWP methods is simply to generate a pressure wave which propagates through the dielectric material. In LIPP, this pressure wave is induced by irradiating the sample with a very short laser pulse, and hence the name of laser induced pressure pulse.

Figure 3.1 shows a sample of dielectric material with an electric stress applied between semicon electrodes 'A' and 'B'. A very short laser pulse, typically of the order of nano seconds, is used to rapidly heat the surface of electrode 'A'. This causes the surface of the target electrode to expand as it heats and then relax as it cools, thus initiating an acoustic pressure wave which will traverse the sample at the velocity of sound 'u' [50].
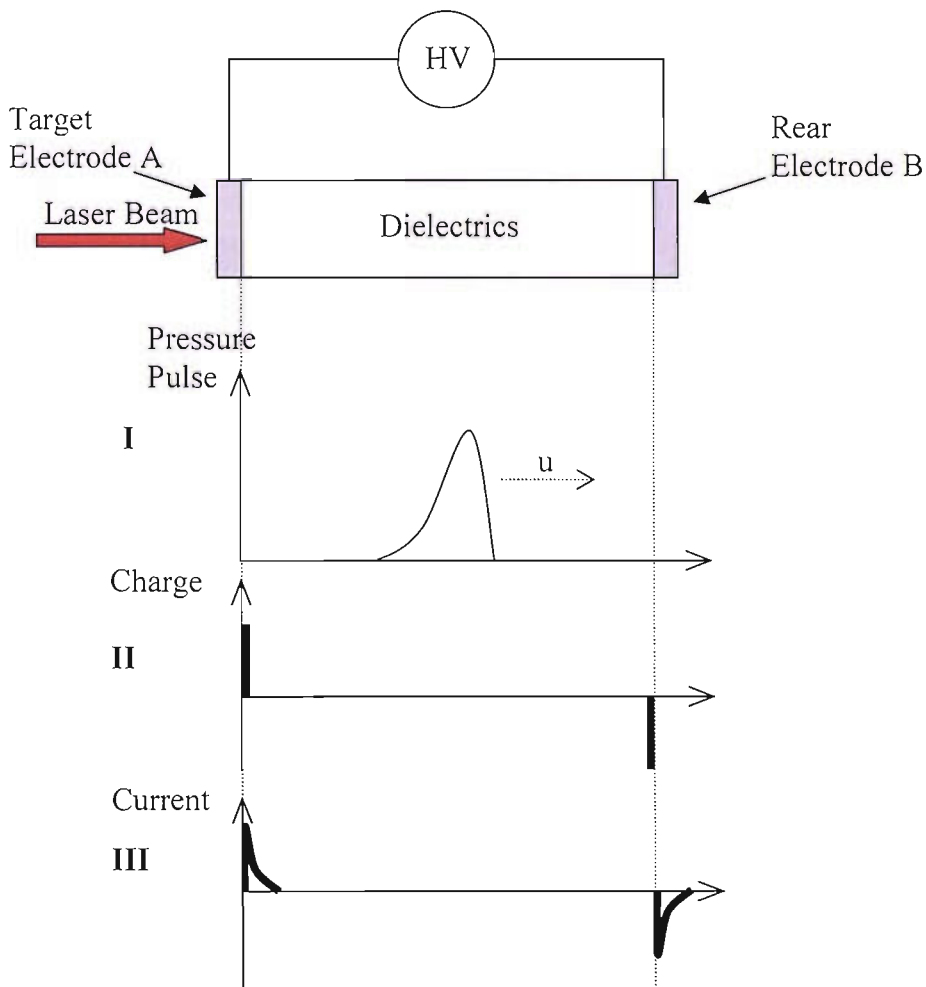
Figure 3.1: Principle of Laser Induced Pressure Pulse Method

As the sample is compressed by the leading edge of the pressure wave, its atomic structure is compressed and two effects are observed. Any charge attached to the local atomic structure is displaced and the relative permittivity (ε_r) is modified due to the local variation in dipole and charge concentration.

These two effects create a variation in the induced charges on the electrodes, which then produces a short-circuit current $I(t)$. The evolution of current as the pressure wave propagates through the material is directly related to the space charge within the material. The pressure wave can therefore be viewed as a virtual probe travelling through the material at the velocity of sound, sensitive to the local charge distribution within the material. Assuming that the dielectric material is homogenous throughout, then the short-circuit current can be defined in terms of the pressure wave profile $p(z,t)$ and the electric stress distribution within the sample $E(z)$ as [37, 69]:

$$I(t) = u_{sa}\chi C_0 G(\varepsilon) \int_{z_f}^{d_0} E(z,t) \frac{d}{dz} p(z,t) dz \qquad (3.1)$$

$$\text{where } C_0 = \frac{\varepsilon S}{d}$$

where χ Compressibility of the sample,

C_o Capacitance of the non-compressed material,

$z_f(t)$ Position of the wave front at time t,

$E(z,t)$ Electric stress distribution,

$p(z,t)$ Pressure wave profile,

z Distance through the sample,

u_{sa} Acoustic speed in the sample,

$G(\varepsilon)$ Coefficient that depends on the relationship between the permittivity and the pressure wave.

Details of equation 3.1 can be found in the literature [38-40, 42, 52, 69] and hence will not be discussed in this report.

As the pressure pulse propagates into the sample, it crosses the front electrode interface; the charge on the surface of electrode 'A' is moved and recorded as a

current pulse. If there is no space charge in the material, then no further current will be recorded until the pressure wave reaches the rear electrode, whereby charge at electrode 'B' will be displaced and recorded as the second current pulse. Ideally, this should produce an output waveform similar to that shown in Trace II of Figure 3.1 but such a waveform is never obtained in reality.

In practice, no matter how short the laser pulse is used, the pressure wave is not an impulse but a compressed fast leading edge followed by a gradual relaxation. As such, the surface charge which the pressure wave passes will not be seen as a current impulse but, instead, a current waveform as shown in Trace III of Figure 3.1. This waveform shows that the two equal and opposite surface charge produces two equal and opposite current peaks at the interface. In a practical case, however, the typical output current waveform will be similar to that shown in Figure 3.2. The third peak is not an indication of the space charge but rather a result of reflected wave caused by the mismatch in acoustic impedance between the dielectric material (XLPE) and the high voltage electrode (brass) of the LIPP system.
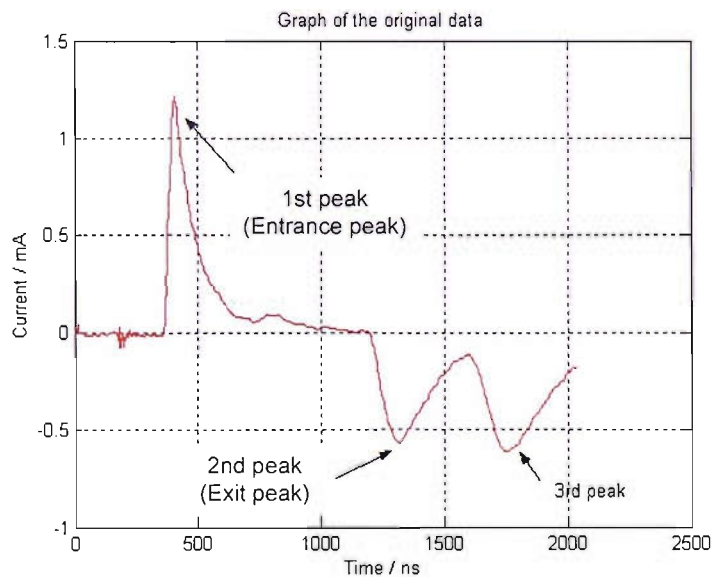
Figure 3.2 Typical current signal of a 1.8 mm XLPE sample

Due to the imperfect elastic properties of the insulation material, the amplitude and profile of the pressure wave will be attenuated and dispersed. As such, the charge distribution from the output current waveform cannot be calculated directly by using equation 3.1. A deconvolution of the recorded output current is required and equation

3.1 must be solved taking into account the form of the pressure wave, $p(z,t)$ at all points throughout the sample.

3.3   Principle of ac LIPP system

Over the years, space charges within dielectrics under dc electric stress have received much interest and numerous publications regarding their evolution and activities in different types of materials were published [27, 29, 31, 38, 40, 44, 66, 70-93]. On the other hand, space charge under 50 Hz ac condition has only received limited attention [35, 69, 94-103]. Since electrical power is usually transmitted at 50 Hz ac, there is a cause for more investigations of space charge under such condition. And hence, the main aim of this project is to investigate space charge dynamics of cable rated XLPE under both dc and ac conditions.

For space charge measurement under dc condition, the applied electric stress across the dielectric material is constant and does not change with time. However for space charge measurement under ac condition, the applied electric stress is time dependent. Hence it is important to have a good correlation between the measurement taken and the amplitude of the electric stress at that instant of time. This is best achieved with point-on-wave control of the applied voltage [69, 95, 97, 98]. Since the time taken for the propagation of the pressure pulse is small (of the order of μsec) as compared to a 50 Hz (period of 20 msec) ac voltage, the applied stress can be assumed to be constant during the period of measurement. Therefore, by measuring space charge at equal intervals over an ac voltage waveform as shown in Figure 3.3, an ac LIPP system is, in principle, feasible.
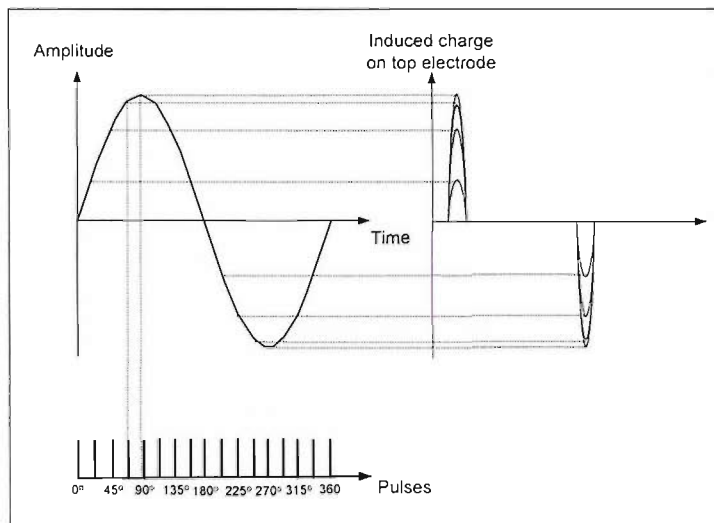
Figure 3.3 Point-on-wave on an AC waveform

3.4   Experimental setup of ac LIPP system

Figure 3.4 shows the block diagram of the LIPP system arrangement. The laser used to generate the acoustic pressure wave is a Q-switched 1.064 μm Nd/YAG laser system. This is a high power laser system capable of producing laser output power of up to 350 mW.
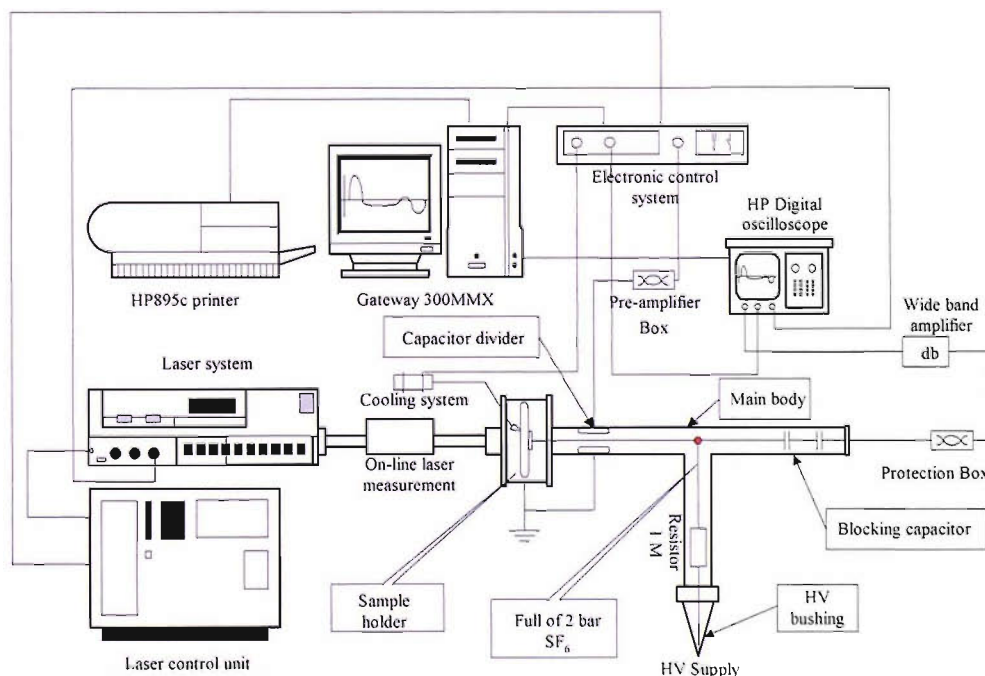
Figure 3.4 Block diagram of ac LIPP system with plaque sample holder

As mentioned before, the point-on-wave technique, which requires numerous laser shots to be irradiated on the target electrode, is employed for ac space charge measurement. It is obvious that repeated shots of the laser on the target semicon electrode within a very short interval, coupled by the high output power of the laser, will cause damage hence change its acoustic properties [54, 69, 98].

Two measures were taken in an attempt to minimise this effect. Firstly, a target protection system based on the concept of using an aluminum disc block as a target for the laser since ablation caused by laser on aluminum was reported to be insignificant [65]. More details on target protection system will be discussed in later in the next section.

Secondly, rather than performing successive measurements on the same cycle of an ac waveform, space charge measurements are performed over a series of ac cycles. This is achieved by firing successive laser shots at time intervals based on an algorithm described below:
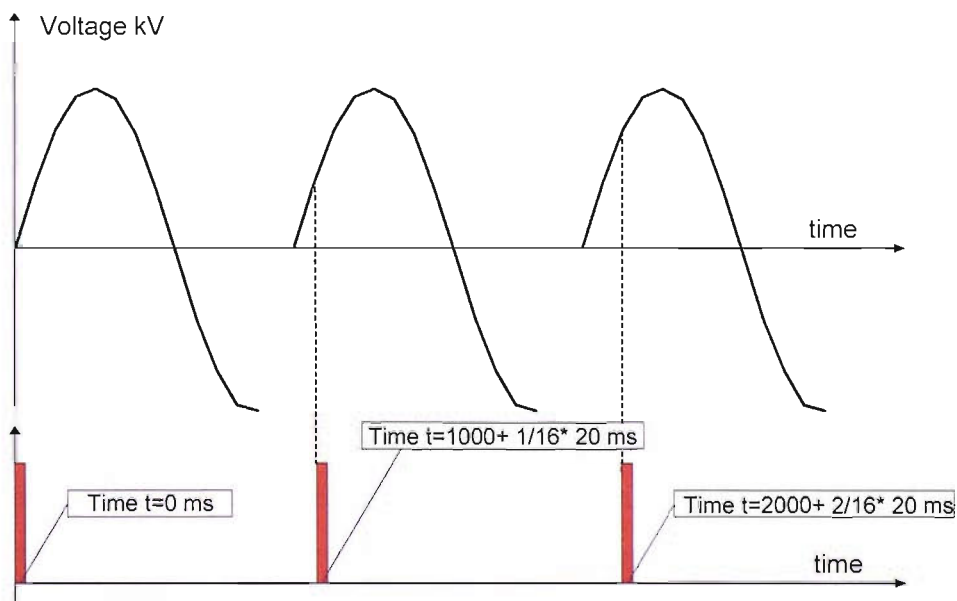
Figure 3.5 AC Space charge measurement at successive phases of different cycles

A time delay between successive pulses is imposed based on the following algorithm:

$$1000ms + \frac{1}{(N-1)} * 20ms \qquad \text{where N = number of measurements} \qquad (3.2)$$

For example figure 3.5 illustrates an example of achieving 17 measurements at different points on an ac wave. The time delay will hence be:

$$1000ms + \frac{1}{(17-1)} * 20ms \quad = \quad 1001.25ms$$

This has the advantage of allowing the target electrode more time to cool down thereby reducing the ablation on its surface and at the same time, it also provides more leeway on the performance of the instruments used.

3.5 Target protection system

The target protection system consists of 2 parts- a liquid cooling system and aluminum disc block.

3.5.1 Liquid cooling system

Initially, the main purpose of the liquid cooling system is to inject a thin layer of cooling liquid on to the surface of the semicon target electrode just before firing the laser pulse. This thin layer of liquid is supposed to absorb most of the energy of the laser to generate a pressure pulse and, at the same time, prevents the target electrode from getting damaged.

A pressure pump would be one mean to achieve consistency in the amount of cooling liquid injected on to the target surface for each measurement. However, the main drawback of this is that the pump creates bubbles inside the liquid, which can deposit on to the target. If the laser pulse lands on the liquid film containing bubbles an unexpected loss of laser energy may arise.

Utilising gravitational force rather than electric pump to inject the liquid eliminates the possibility of air bubbles being created in the injected liquid. A schematic diagram of the liquid cooling system is shown in figure 3.6.

It is impossible to synchronise the laser firing timing algorithm with the injection of cooling liquid manually. Hence, an electronic control system was designed for this purpose. The electronic control system, originally designed by the "HLP technologies", was modified by the University of Southampton. Details on the circuit design of the electronic control system can be found in Appendix A.
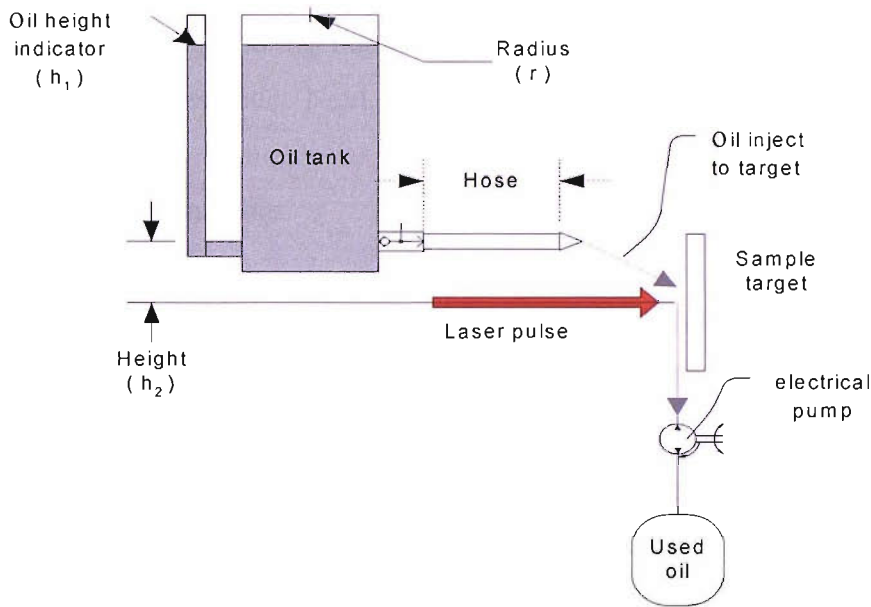
Figure 3.6 The schematic diagram of the target cooling system using gravitational force

This electronic control board allows the user to preset the number of shots for each ac space charge measurement. The number of readings over one complete cycle of ac space charge measurements is an important factor of consideration. While a more accurate representation of the space charge characteristic can be obtained, more readings also imply that the target electrode will be subjected to more laser pulses. This has the effect of ablating the material of target electrode more rapidly, thereby affecting its ultrasonic properties. This problem can be largely overcome by placing an aluminum disc in front of the target electrode. More details of this will be discussed in section 3.5.2. The selectable preset values for number of readings for one complete cycle of ac space charge measurements are 9, 17, 33 and 65.

As mentioned earlier, the semicon target ablation caused by the laser will result in significant error in the measurement. Ho et al [65] reported that the efficiency of the laser absorption of the semicon target surface will degrade after experiencing >40 laser shots, even with the liquid cooling system, and consequently affect the pressure wave profile and the calibration for the space charge measurement.

A few factors need to be considered when deciding on the choice of cooling liquid. First and foremost, the cooling liquid must be slightly viscous so that it is able to 'stick' on the target electrode. Next, for the laser to induce a consistent pressure wave, the liquid on must be homogenous and particle-free. Lastly, for safety reasons, the liquid must not be flammable.

Silicone oil was chosen as it satisfies all the above criteria and is cheap and easily available. It will be interesting to investigate how much of the laser's power is actually absorbed by the oil to generate the pressure pulse. The wavelength of the laser used is 1060 nm. An ultra-violet spectrum of the silicon oil, as shown in figure 3.7, indicates up to 95.2% of the laser's power is transmitted. This suggests that only less than 5% of the laser's power is actually absorbed by the silicone oil. This absorption may be due to the silicon-oxygen backbone (Si-O-Si bond) of the silicone oil.

Initially, the oil was thought to have absorbed most of the laser's power to generate the pressure wave; however, this is clearly not the case. Further investigation is required in order to fully understand the relation between the laser, the silicone oil and the generation of pressure wave. Nevertheless, for the purpose of this project; it is sufficient that the silicone oil helps to amplify the pressure wave induced by the laser.
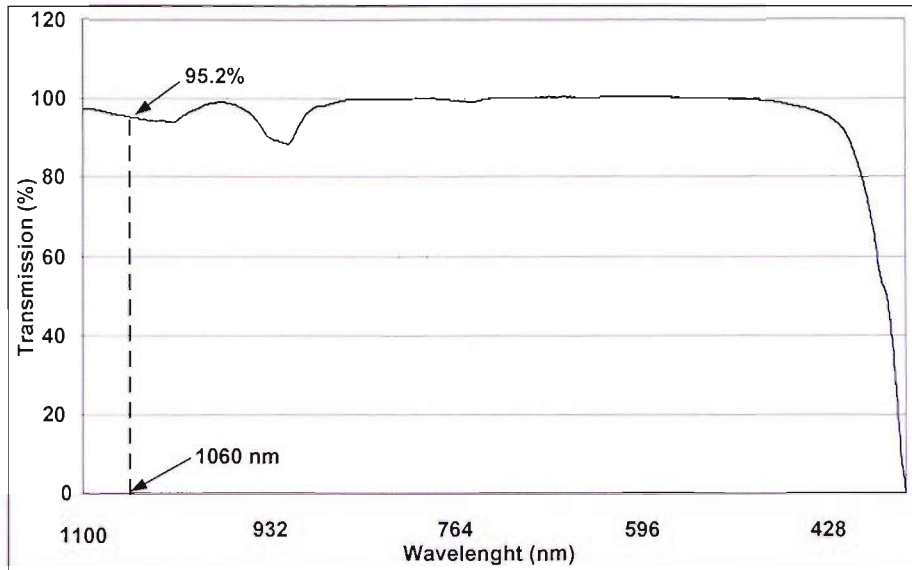
Figure 3.7 Ultra-violet spectroscopy of silicone oil

3.5.2   Aluminum target electrode

To prevent any error caused by the target degradation, a correction factor was initially introduced to modify the raw current data before any data processing was performed [69]. However, as the correction factor for semicon target degradation is dependent on both the semicon material and thickness of the sample, it will vary from sample to sample. In order to eliminate this problem, a metal target can be placed in front of the front semicon electrode and acting as the laser target. Due to the intrinsic hardness of metal, the ablation of the target as a result of the short pulse laser is negligible.

Also, the layer of cooling liquid will possibley affect the relaxation time of the pressure wave. In some cases the leading edge of the current pulse at the rear interface will interact with the tail of the current pulse from the front interface, causing an incorrect space charge distribution indicated as a "signal offset" towards the rear of the sample as shown in figure 3.8(a).
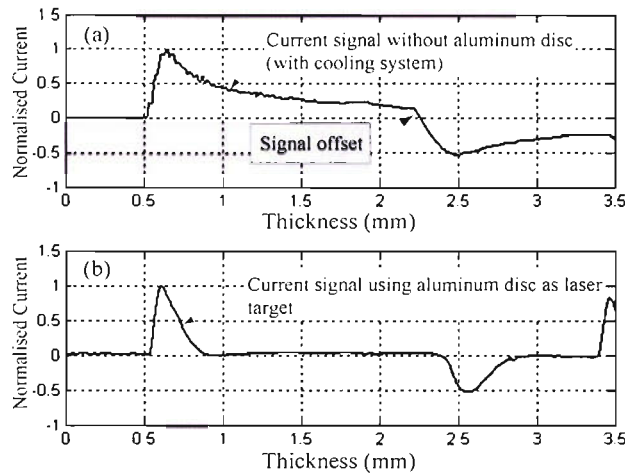
Figure 3.8. Normalised current signals without using (a) and with using (b) aluminum disc as laser target (third shot measurement)

An obvious way to eliminate this effect is to spray a thinner layer of cooling liquid. However, this is extremely difficult to achieve in practice. Another way to go about this is to irradiate with another laser shot about one second after the first, only this time without spraying a layer of liquid on the surface. For the sake of convenience, this shall be referred to as second-shot measurement. By the same argument, a third-shot measurement can also be obtained again with two additional laser shots after the first. This is made possible because the effect of ablation caused by the laser on aluminum is much less significant than on semi-con electrode. A second, let alone a third, shot measurement will result in major degradation on the semicon electrode. After some consideration, aluminum was chosen because of it availability and machinability. It should be pointed out, however, that the method of taking a second/third shot measurement is not suitable to be used on to the point-on-wave technique during ac space charge measurement as repeated measurements are required within a very short duration of time.

The acoustic velocity in the aluminum target disc and the XLPE sample are $6500ms^{-1}$ and $2000ms^{-1}$ respectively. The mismatch in acoustic impedance between aluminum and XLPE may result in interference of reflected waves as shown in figure 3.9. Hence, the thickness of the aluminum disc relative to the sample becomes a factor for consideration.
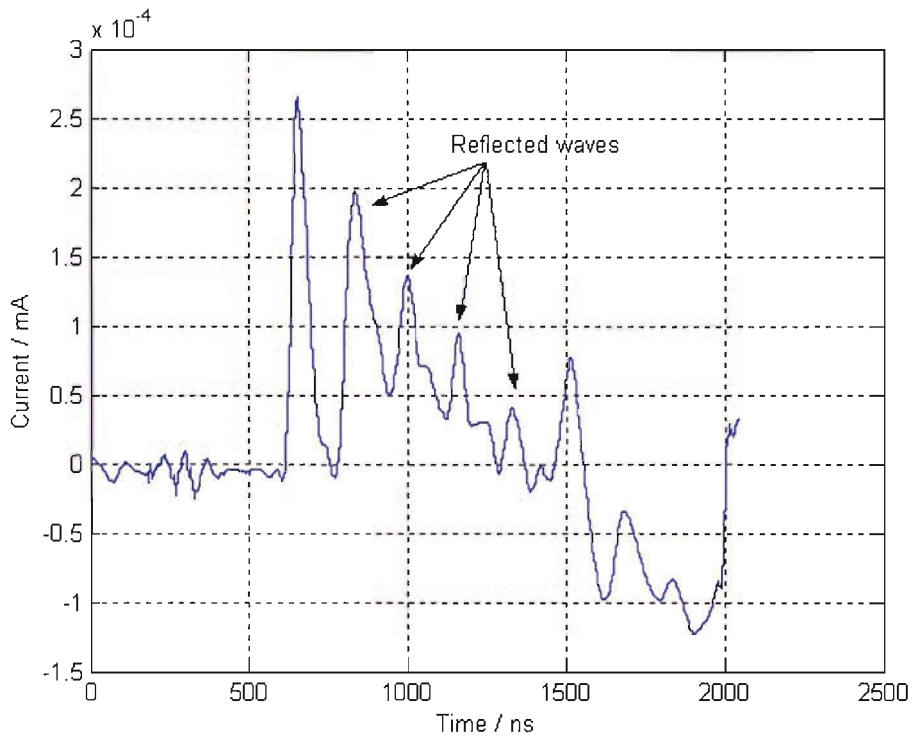
Figure 3.9: Space charge profile of a 3.10 mm (including semicon electrodes) thick XLPE sample using 0.5 mm thick aluminum plate as the target.

The effect of the thickness of the aluminum block is directly dependent on the thickness of the test sample. Referring to the Figure 3.10, if the thickness aluminum disc (X) is too small, the reflected pressure wave (P2 in figure 3.10) created at the aluminum/semicon interface will bounce back through the aluminum disc and is then reflected from the front of the aluminum disc back towards the sample. This second pressure wave (P3 in figure 3.10) will then pass through the sample/semicon interface with a short delay time (t), after the original pressure wave (P1 in figure 3.10) and create a reflected current signal as shown in figure 3.9. This could be mistakenly interpreted as a layer of charge within the sample.
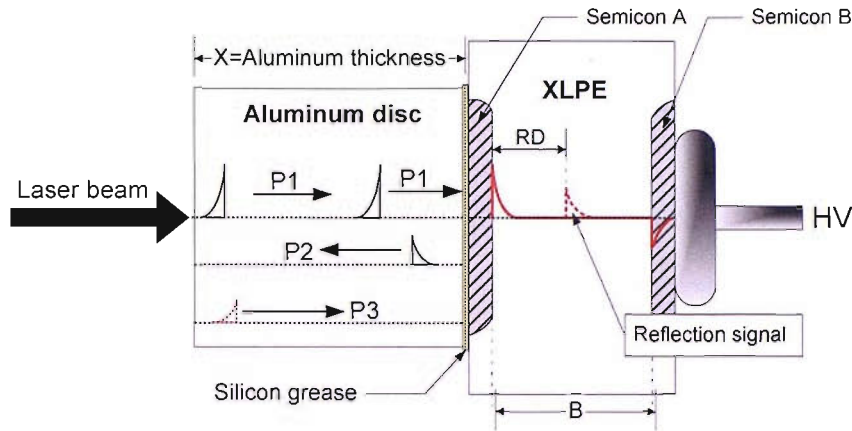
Figure 3.10: Schematic diagram showing how the reflection signal created in the LIPP system by using aluminum disc target

In order to eliminate the error created by the reflection current signal, the time delay (t) of the second pressure wave (P3) must be greater than the time required for the original pressure wave to completely transverse through the dielectric sample at the velocity of sound.

$$t = \frac{2X}{\mu_{Al}} > \frac{B}{\mu_{XLPE}} \tag{3.3}$$

where $\mu_{al} \approx 6500 ms^{-1}$ and $\mu_{XLPE} \approx 2000 ms^{-1}$

One way to satisfy equation 3.3 is to make the aluminum disc (X) very much thicker than the sample (B). While this may hold true mathematically, practical constraints and the direct effect of the thickness of aluminum has on the spatial resolution of the system set a limitation to the aluminum thickness.

The spatial resolution of the LIPP can be determined by measuring the rise time of the current pulse from the electrode/sample interface and multiplying the velocity of sound for the material being tested. An illustrative diagram of a typical current pulse recorded from a front sample/electrode interface is shown in figure 3.11.
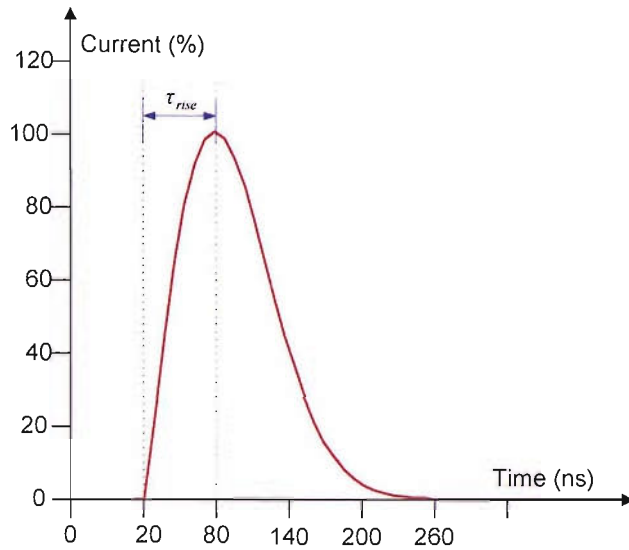
Figure 3.11 Illustrative diagram of the current pulse at the front sample/electrode interface (target) for the resolution calculation

The typical rise time "τ_{rise}" of the current pulse in the LIPP system with target cooling system (i.e. silicone oil) is around 60ns, hence giving a spatial resolution of 120μm as the velocity of sound in crosslinked polyethylene is about $2000ms^{-1}$.

3.5.3 Optimisation of aluminum target electrode thickness

The details of the aluminum disc thicknesses used are shown in Table 3.1. The test sample is approximately 2mm thick (bulk) made by the cable grade crosslinked polyethylene with semicon electrodes hot pressed on both sides at $200\,^{O}C$ for about 10 minutes. The semicon electrodes were made of the same grade of polyethylene material, but were loaded with carbon black to increase its conductivity.

Space charge build up near the vicinity of the electrode may affect the rise time of the current pulse at the electrode. This will result in misinterpretation of the spatial resolution of the system. Hence, it is important to prevent charge build-up during the experiment and one way of doing so is to degass the sample at 90°C in a vacuum oven for 48 hours. In a later part of the thesis, it was reported that no significant charge was built up in sample of this composite even at an applied stress level of 35kV/mm for short duration.

Sample	Thickness
A	1.25
B	1.45
C	1.98
D	2.45
E	3.10
F	3.70
G	4.12
H	4.59
I	5.15
J	6.14

Table 3.1. Details of the aluminum disc

Figure 3.12 illustrates the graph of spatial resolution against the thickness of the aluminum disc using in the LIPP system. It is obvious that the spatial resolution of the system decreases with the thickness of the aluminum disc. By comparing the spatial resolution between the measurement signals using (i.e. better than 100μm when the aluminum disc is less than 7mm thick) and without using (i.e. 120μm with target cooling system) an aluminum disc as the laser target, it is evident that the aluminum disc has improved the spatial resolution of the LIPP system by maximum 33% using 1mm aluminimum disc. As mentioned eatlier, the aluminum thickness will also create pressure wave reflection, therefore it also is equally important to investigate the effect of thickness of the aluminum disc on the reflected pressure wave.

Figure 3.13 shows two examples of the current signal obtained from 2mm XLPE plaque sample by using two different thickness of aluminum discs (i.e. disc C and disc H). The graph of the reflected current peak position within the bulk insulation against the entire series of aluminum disc thickness is shown in figure 3.14.
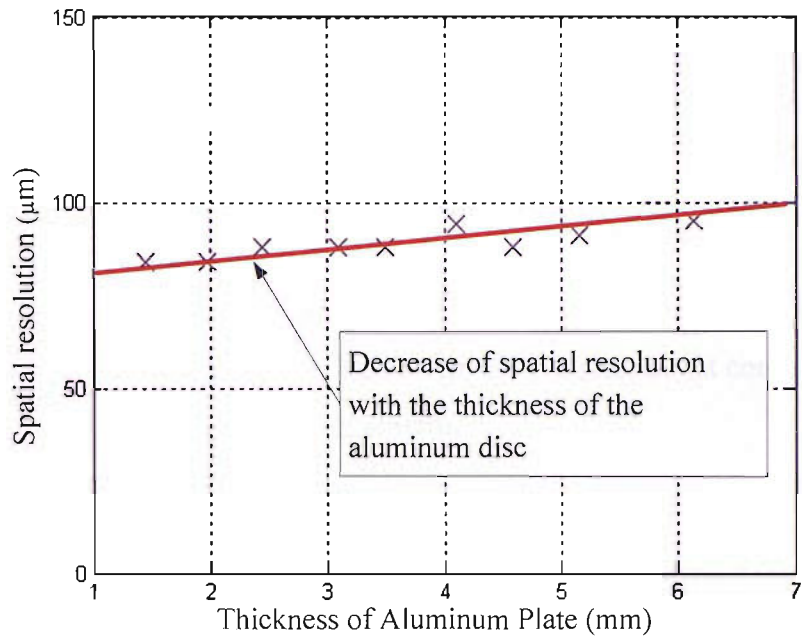
Figure 3.12: Spatial resolutions against aluminum disc thickness in the LIPP system
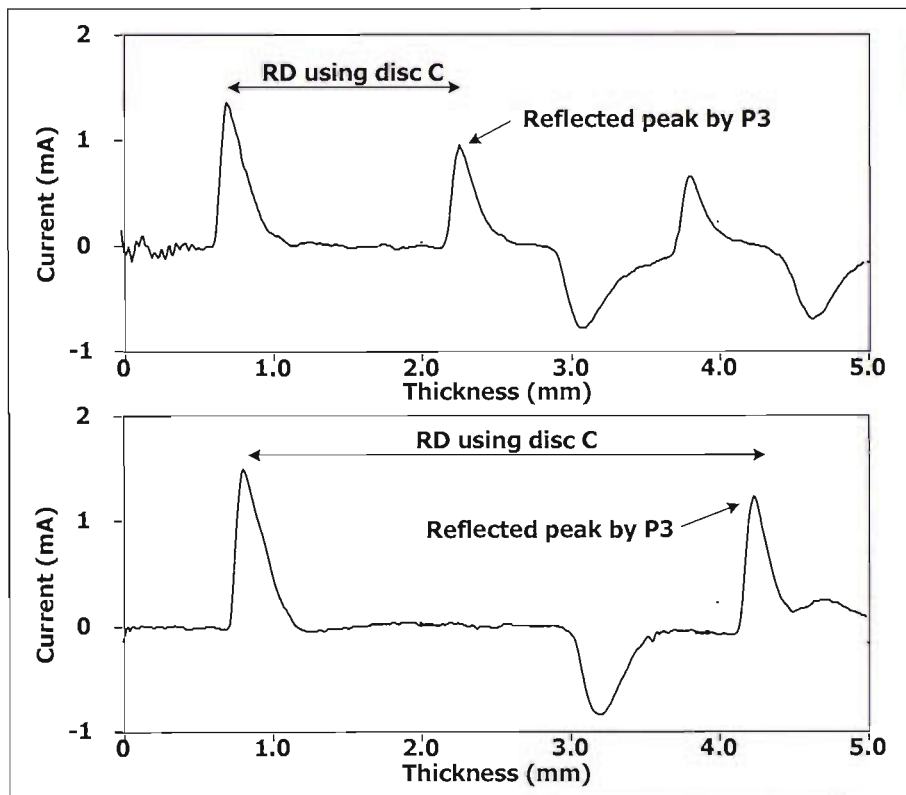
Figure 3.13 Current signals obtained by using (a) aluminum disc C and (b) aluminum disc H in the LIPP system

According to figure 3.14, the threshold thickness of the aluminum disc to 2mm XLPE plaque sample is around 3.10mm. However, in most of the cases the exit peak of the current signal will be used to determine the interfacial stress on the XLPE/semicon interface, therefore the exit peak of the current signal is best left undisturbed by the reflected current signal. In order to achieve this condition, the distance of the reflected current signal (RD) suggests to be greater than 2.5mm (i.e. RD=3mm), hence the aluminum disc H with thickness 4.59mm is recommended and the spatial resolution of the measurement will be around 90μm with 25% improvement compared to 120μm using only the semicon target cooling system.

The implementation of the aluminum disc block as a target for the laser is also instrumental for ac space charge research. This is due to the limitation imposed by the HV ac transformer (30kV), giving a maximum electric stress of only 15kV/mm for a 2mm plaque. In order to achieve a stress level of 30kV/mm, it is necessary to reduce the bulk thickness of the plaque sample to 1mm. Along with this reduction in bulk thickness, it is also necessary to reduce the thickness of the semicon electrode in order to maintain an acceptable spatial resolution. Formerly, with the semicon acting as a direct target, there is a limitation as to how thin the semicon electrode should be. However, utilising the aluminum disc as the target almost completely lifts this constraint. According to figures 3.12 and 3.14, the optimum thickness of the aluminum disc suggested for 1.2mm XLPE plaque is 2mm and this will give 85μm in spatial resolution.

It should be pointed out that even with the implementation of the aluminum target disc, the liquid cooling system is still required. However, the primary, and probably the only, reason for this is to generate the pressure wave induced by the laser rather than to reduce target ablation effect when the semicon electrode was used as the direct target.
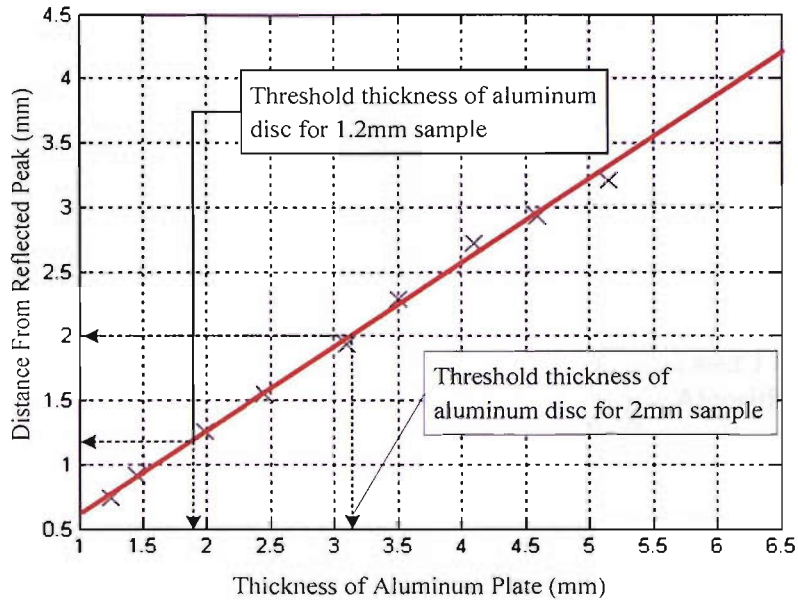
Figure 3.14 The distance between the reflected current peak signal (RD) and the entrance peak against the thickness (X) of aluminum disc

3.6   Automation of the LIPP using LabVIEW

An automation programme, using LabVIEW, was developed in an attempt to improve on the performance of data acquisition in the LIPP system. This is especially important during ac space measurement as a considerable amount of data is generated over a short period of time.

Although the task of programming was made easier with the laser pulse triggering algorithm and synchronisation of the liquid cooling system being controlled by the electronic board, much of the system automation still depends on the programme itself. The programme is required to:

a)   configure the digital oscilloscope (HP 54510)

b)   send a 'start' bit to the electronic board to initiate data acquisition

c)   capture waveforms displayed on the oscilloscope and store them for data processing

d)   send a 'stop' bit to the electronic board to terminate data acquisition.

A block diagram representing the automated data acquisition system is shown in Figure 3.15.
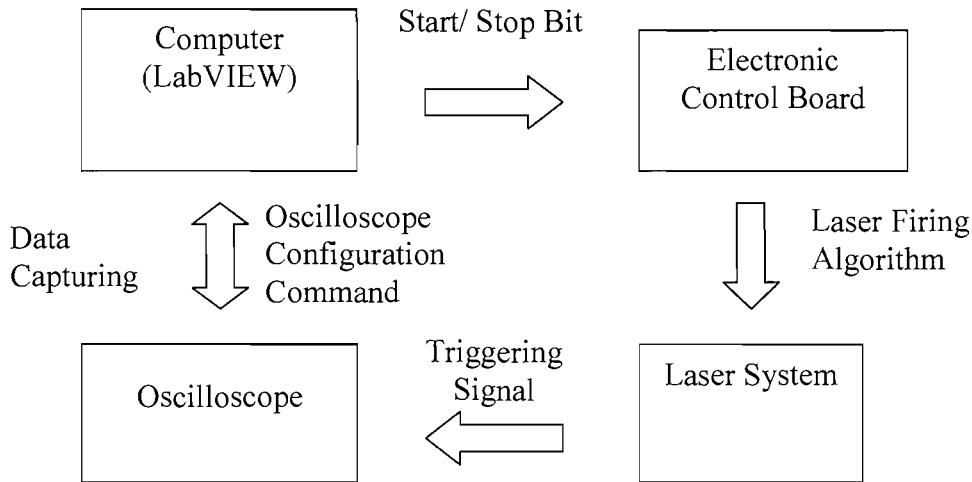
Figure 3.15: Automated Data Acquisition System

Communication with the oscilloscope is established using a General Purpose Interface Bus or GPIB (IEEE 488.2) card. It is noteworthy that GPIB is a serial bus, therefore, the sending of commands to and the collection of data from the oscilloscope cannot be done simultaneously.

A digital input/output card was installed on the computer to facilitate the transmission of the start and stop bits to the electronic board. The interval between the start and stop bits is determined by the number of successive space charge measurements input by the user.

The operation of the programme can be summarised by the flow chart shown in Figure 3.16.
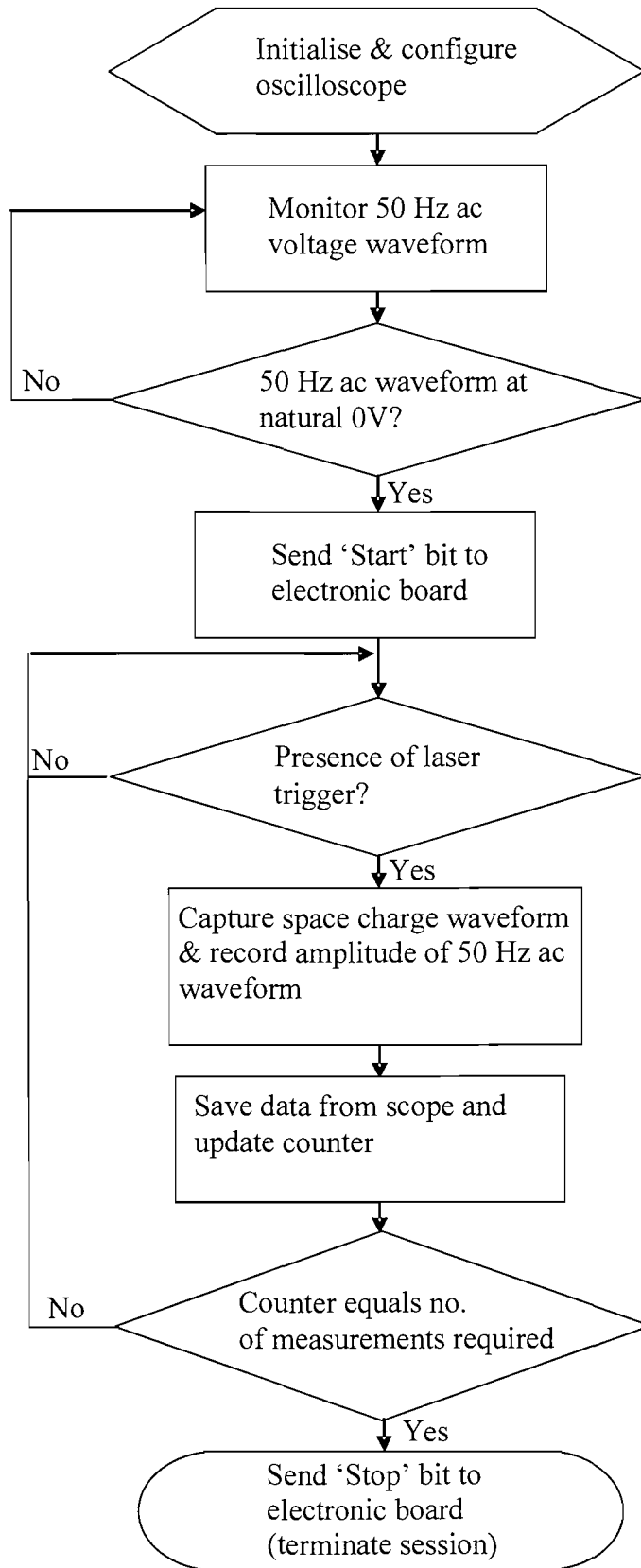
Figure 3.16: Flowchart of automated data acquisition programme

The automated data acquisition programme can also be used as a sub-routine to perform space charge measurements of a dielectric material at different times of its ageing period. This can be accomplished simply by implementing the above programme with the various repetitive loops inherent in LabVIEW. This reduces the monotonous nature of having to manually operate the system each time a space charge measurement is required.

3.7   Data Processing

The raw space charge data obtained directly from the LIPP bears little meaning when used for quantitative studies. Data processing such as filtering, calibration, signal recovery and compensation is required.

3.7.1   Calculation and calibration of space charge in planar sample

With reference to Equation 3.1, it can be shown that the space charge distribution within the XLPE is given by Equation 3.4 [69]:

$$\rho(z) = f(I_{space}, I_{cal}) = \frac{I_{space}(z,t)}{I_{cal}(0,t)} \cdot \frac{P_0}{P_z(z)} \cdot \frac{\varepsilon_0 \varepsilon_r E_{cal}}{u_{sa} \tau(z)} \tag{3.4}$$

where $\rho(z)$ is the charge density at location z,

$I_{space}(z,t)$ is the current recorded at location z,

$I_{cal}(0,t)$ is the calibration current at the target interface,

P_0 is the amplitude of the pressure wave at the target interface,

$P_z(z)$ is the amplitude of the pressure wave at location z,

ε_0 is the permittivity of free space,

ε_r is the relative permittivity,

E_{cal} is the electric stress used for calibration,

u_{sa} is the velocity of acoustic wave in the sample,

$\tau(z)$ is the width of the pressure wave at location z.

Therefore the space charge density distribution can be calculated providing the following information is known:

- Calibration electric stress E_{cal},

- Calibrated peak current $I_{cal}(0,t)$ at the target interface during the application of E_{cal},

- The pressure wave profile (i.e. magnitude and width) at all positions of "z".

In principle, the calibration electric stress E_{cal}, can be any stress level lower than the threshold stress value whereby space charge initiates in the insulating material. In practice, however due to poor signal-to-noise ratio at low level stress, the choice E_{cal} is often chosen to be as close to the threshold stress as possible.

3.7.2 System response and signal recovery

The typical output signal from a LIPP system without target cooling system is shown in figure 3.17.
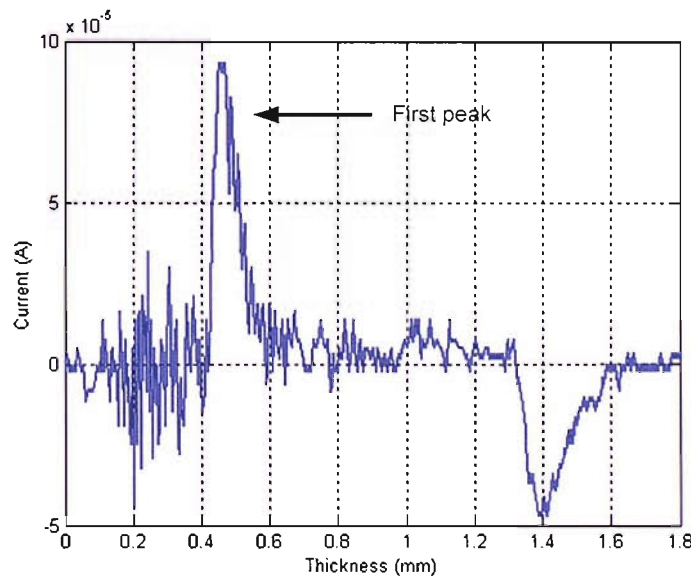
Figure 3.17: Typical output signal without target cooling

When a very short laser pulse irradiates and heats the surface of the semi-conducting electrode, it expands rapidly and relaxes as it cools, forming an acoustic pressure wave similar to that shown in figure 3.17. Notice that the first peak has a rapid rise

time and slightly more gradual relaxation time. This is because the rate at which the electrode heats up and cools down is different.

The signal above has very high spatial resolution but rather poor signal-to-noise ratio. This poor signal-to-noise ratio is even more pronounced at low levels of electric stress, although this can be improved with wavelet packet filters.

The introduction of target cooling significantly improves the signal-to-noise ratio, however, at the expense of signal distortion as shown in figure 3.18. The interaction between the first and rear peaks is due to incomplete relaxation of pressure pulse which may be mistakenly interpreted as charge.
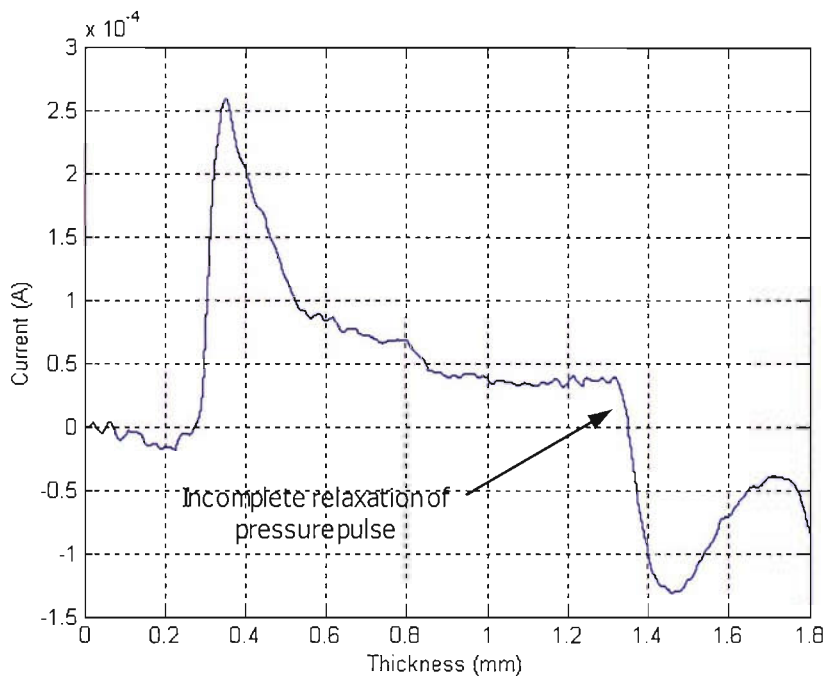
Figure 3.18: Typical output signal with target cooling

As mentioned in section 3.5, a second or third shot measurement, as shown in figure 3.19 and 3.20, reduces this effect.
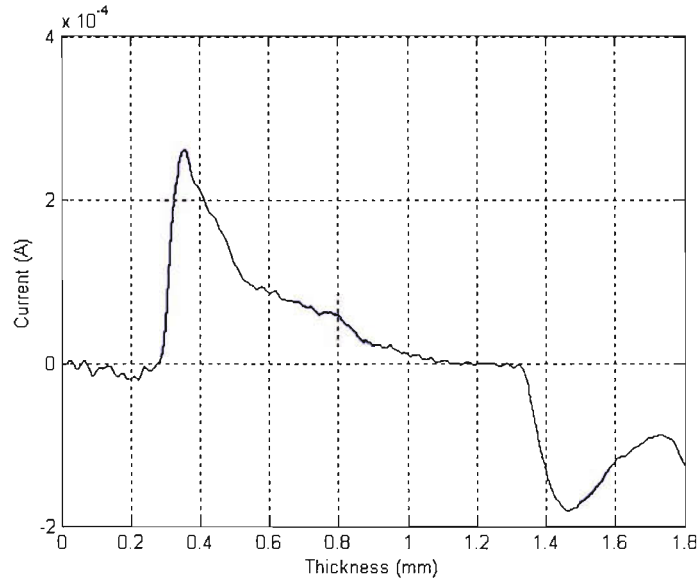
Figure 3.19: Second-shot measurement
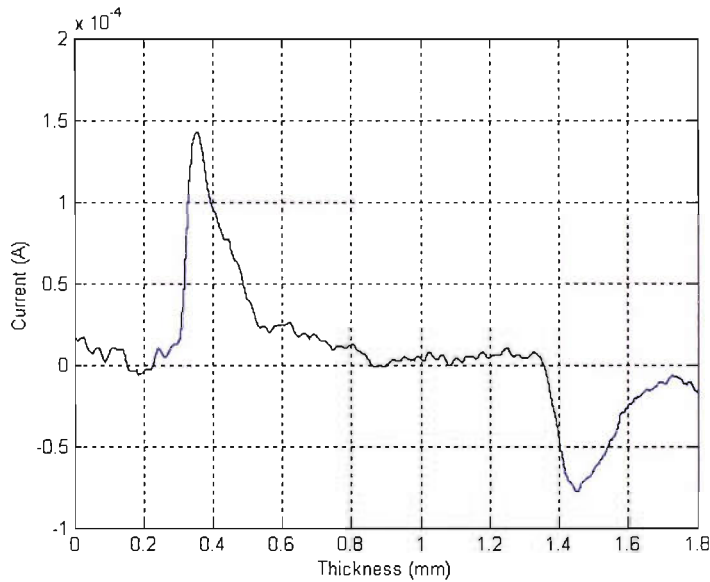
Figure 3.20: Third-shot measurement

It can be seen from the graphs above that the third-shot measurement is the closest approximation to the ideal output signal shown in figure 3.17.

Measurements beyond the third-shot measurement or using aluminum block without cooling liquid, yields outputs with signal-to-noise ratios that are too low for practical consideration.
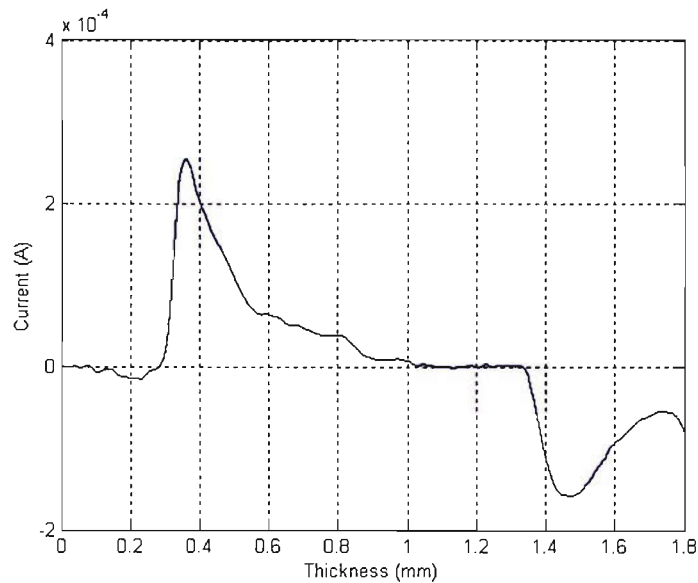
Figure 3.21: First-shot measurement removing low frequency component.

The implementation of cooling liquid together with the applied DC high voltage is understood to affect the low frequency element. The signal shown in figure 3.21 is a result of passing the first shot measurement through a high pass filter. Notice the interaction between the first peak and the second peak is reduced significantly.

It is noteworthy that the rear peak of the waveform did not relax to zero as shown in figure 3.20. As mentioned before, this peak is not a correct representation of the charge distribution in the sample but rather interference of a reflected wave from the metal electrode of the system due to impedance mismatch. This peak, however, can be recovered either with polynomial or exponential extrapolation.

3.7.3   Attenuation and dispersion

As mentioned in section 3.2, the amplitude and the pulse width of the pressure wave tends to reduce and broaden respectively as it propagates through the sample. This is caused by attenuation and dispersion of the pressure wave as it transverses through the dispersive material, accounted for by the P_z and τ terms in Equation 3.4.

The profile of the pressure wave at any point within the material can be calculated using Fourier analysis of the first peak and rear peak of a charge-free output signal.

Figure 3.22 shows the profile of pressure wave propagation of the first shot measurement. The values of P_z and τ can hence be calculated.
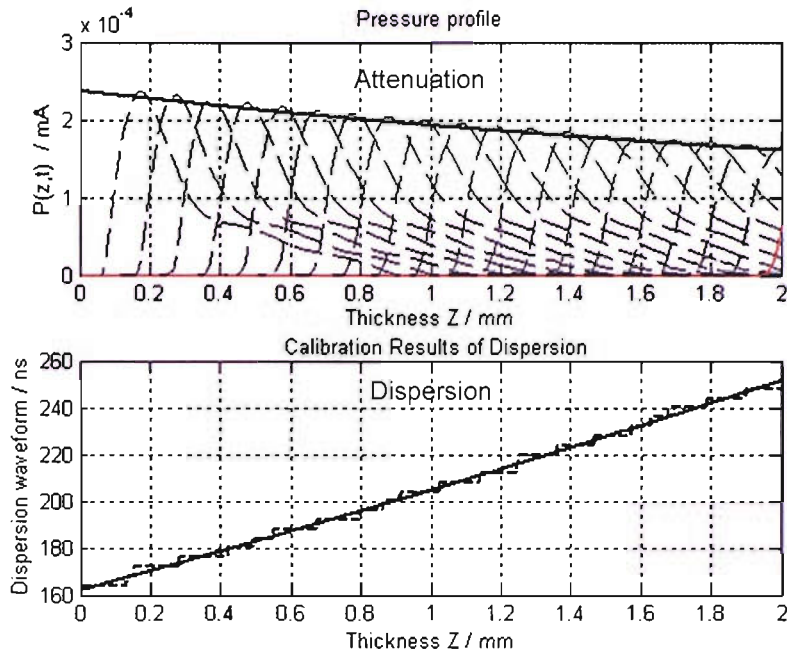
Figure 3.22: Profile of pressure wave propagation

3.8   Conclusion

This chapter reports a LIPP system that is capable of measuring space charge in a dielectric sample under both dc and 50 Hz ac electric stress. The basic principles behind dc and ac space charge were reviewed. The technique employed for ac space charge measurement is the point-on-wave.

In order to perform the successive measurements at different precise point on the ac wave, an electronic board was designed. In addition to provide the firing algorithm for the laser system, this electronic board also synchronises the triggering of the cooling liquid to reduce the ablation of the target electrode.

The significance of target ablation during ac space charge measurement was discussed along with some proposed solution to minimise it. The adopted solution of this project is to implement an aluminum disc which acts as a direct target for the laser to be irradiated on.

The thickness of the aluminum disc chosen is of major importance. This is dependent directly on the thickness of the sample that is being tested. A good compromise is one that is thin enough to give the highest possible spatial resolution but at the same time thick enough to prevent reflected pressure wave from interfering with the space charge signal.

A programme using LabVIEW was developed in an attempt to automate the LIPP system. This has been done with considerable success although further improvements are still needed before the LIPP system can be fully automated.

This chapter also covered on the data processing methodology such as calculation and calibration of space charge density. The distortion of output signal as a result of system response was also dealt with.

4 Pulsed Electroacoustic Technique

4.1 Introduction

The principle of the LIPP technique was briefly covered in chapter 3. While the LIPP technique is used by many researchers for space charge measurement, the pulsed electroacoustic (PEA) method is by far the most popular method used in most parts of the world.

The PEA method was developed by T. Takada of the Musashi Institute of Technology in Japan in 1983 [86, 104]. The basic idea behind the PEA is similar to that of the LIPP in that both techniques use ultrasonic waves to obtain the space charge profiles. The fundamental difference between the two is that, unlike the LIPP where the acoustic wave is induced externally, the PEA generates its acoustic wave internally.

Both techniques have their advantages and disadvantages and the choice of technique depends solely on measurement conditions and requirements. This chapter reviews the basic principle of the PEA technique, the signal processing algorithm (deconvolution) and a comparison with the LIPP from a practical standpoint.

4.2 Principle of the PEA technique

Figure 4.1 shows the principle of the PEA technique. As seen in the figure, two charge layers are formed at the electrode as a result of the high voltage dc supply. For the sake of simplicity, it is assumed that no space charge is formed in the bulk of XLPE sample.

When an external high voltage pulse Vp(t), typically amplitude of 0.1 to 2 kV and pulse width of 5-200ns, is applied between the electrodes, acoustic pulsed pressure waves governed by Lorentz's Law, are produced at the charge layers [105].
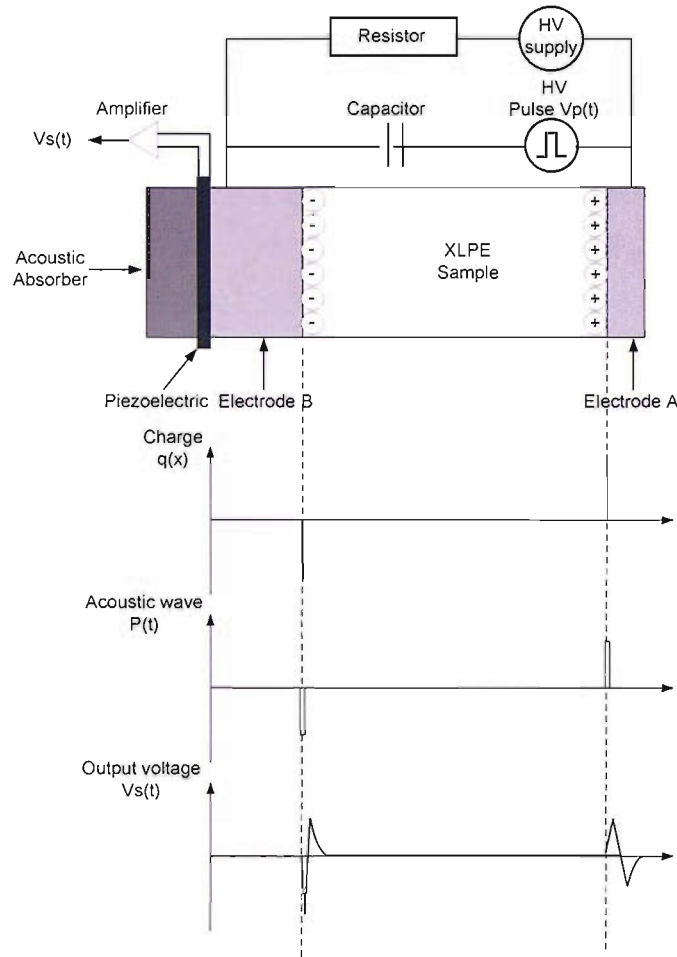
Figure 4.1: Basic principle of PEA

Consider the pressure pulse travelling from the electrode A. The pressure wave will travel through the sample and into the electrode B. The pressure wave is then transmitted to the piezoelectric transducer whereby the mechanical signal is converted into electrical signal. This signal is then amplified and captured with a digital oscilloscope.

However, the measured voltage signal from the PEA system is small, resulting in poor signal-to-noise ratio. As such, an averaging approach is necessary for the PEA technique to reduce the random noise level by a factor of $\sqrt{n}$ where n is the number of measurements signal for averaging and is normally >200.

4.3 Signal processing - calibration and deconvolution

From the Poisson's equation for quasi-static field in a dielectric with relative permittivity ε_r,

$$\nabla .E = \frac{\rho(x)}{\varepsilon_0 \varepsilon_r} \tag{4.1}$$

It can be deduced that for a flat sample with electrode charges σ_1 and σ_2 are given by

$$\sigma_1 = -\sigma_2 = \varepsilon_0 \varepsilon_r E \tag{4.2}$$

The value of σ_1 is equal to the integral of the region of the front peak in $\rho(x)$ distribution,

$$\sigma_1 = \int_{z=0}^{z=front\ peak} \rho(x).dx \tag{4.3}$$

However, due to the high capacitance (typically 0.1-5 nF) of the piezo-electric transducer and the low input impedance of the amplifier (50 Ω), they act as a high pass filter, resulting in distortion of the output signal occurs as shown in figure 4.2.
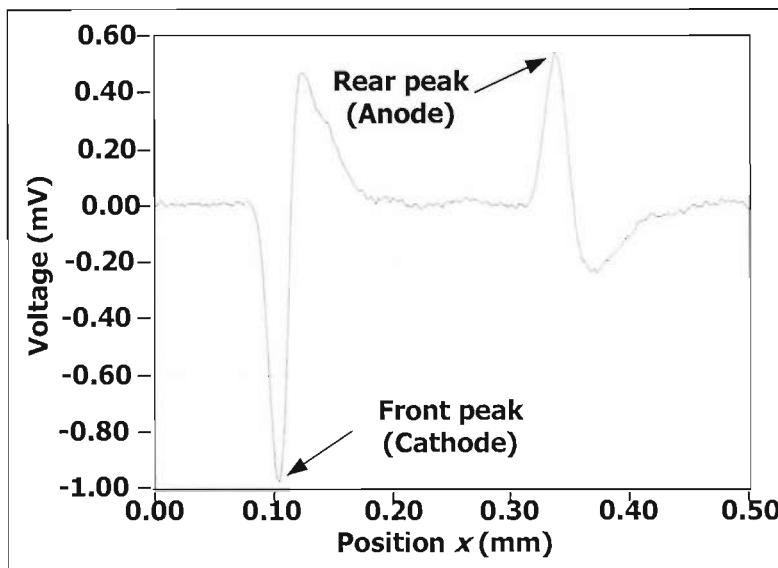
Figure 4.2: A typical PEA output signal

The peak between the cathode and anode, as seen in figure 4.2, is not due to space charge but rather the frequency response of the system. In order to recover the distorted signal a process known as deconvolution is required.

The full mathematical principle behind deconvolution is well documented [105] and will not be presented here. In summary, assuming that the transfer function of the system is $G(f)$, the output signal in frequency domain, can therefore be described as

$$V(f) = G(f)\, \rho(f) \qquad\qquad\qquad (4.4)$$

The system's transfer function, $G(f)$, encompassed not only the high pass filter effect as mentioned earlier but also the piezoelectric strain constant of the transducer. Hence, if $G(f)$ can be found, the actual space charge distribution can be easily computed using Fast Fourier transform (FFT), division, software filtering and inverse Fast Fourier transform (IFFT). The concept of the whole process is illustrated in figure 4.3.
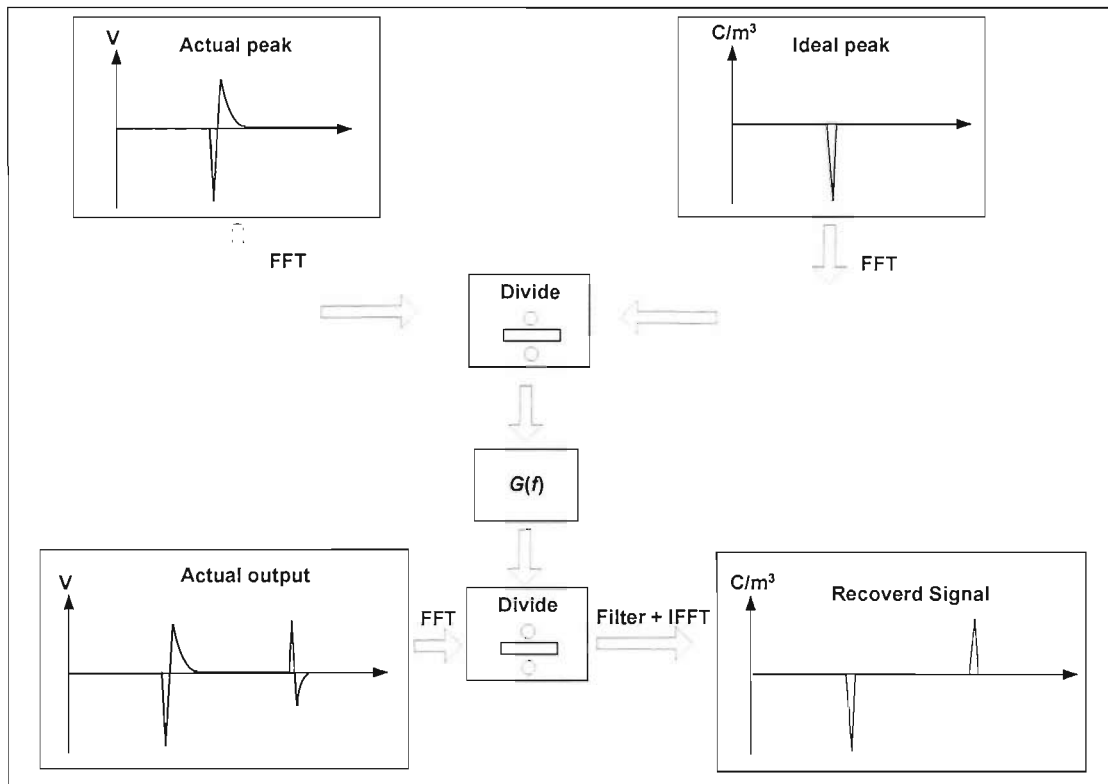
Figure 4.3: Block diagram representation of deconvolution

Furthermore, as the acoustic wave propagates through a material, the absorption and dissipation of the acoustic energy into heat and other forms of energy causes attenuation of the signal. On the other hand, the inhomogeneities and frequency dependence of the material constants such as Young's modulus may result in dispersion of the acoustic signal. A signal compensation algorithm involving Fourier transform has been successfully employed to compensate such effects in thick samples [106]. However, such signal compensation is usually achieved at the expense of reduced spatial resolution. As such, it will only be applied to thick samples (>1 mm) where attenuation and dispersion of the signal are rather substantial.

4.4 Automated PEA system
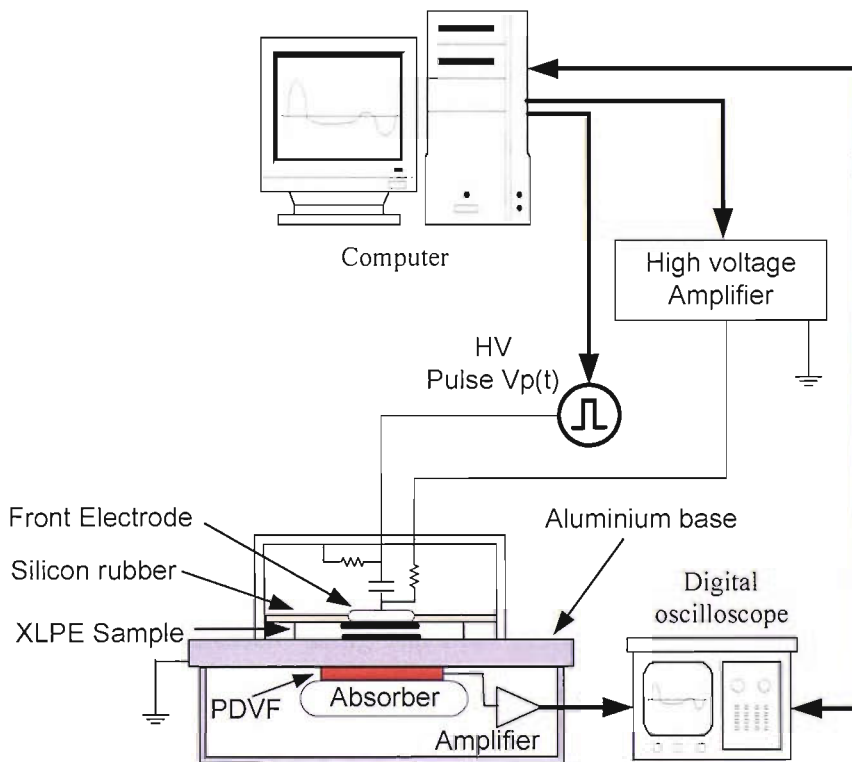
Figure 4.4: Schematic diagram of the pulsed electroacoustic method

A schematic diagram of the PEA system built by the Musashi Institute of technology is shown in figure 4.4. Just like the LIPP system described in chapter 3, this PEA system is also automated with a programme written in LabVIEW platform.

Similar to the programme used in the LIPP system, this programme allows the user to preset the settings of the digital oscilloscope. The user can also preset the time interval between each space charge measurement and the computer will send a triggering signal to the high voltage impulse generator accordingly.

The main difference between the LIPP system and this PEA system is the source of high voltage supply. In the LIPP system, the high voltage supply comes from an external high voltage generator that links directly to the sample. The PEA system, however, uses the computer and a digital to analogue converter to generate voltages that range from +5V to -5V. This voltage is then amplified by a high voltage amplifier. Similar system has been established in the Tony Davies high voltage laboratory in Southampton.

With this approach, the PEA system, unlike the LIPP, can be considered fully automated since it is possible to control the high voltage supply simply by changing the settings on the automation programme. Another advantage of this PEA system is that it is possible to not only generate dc and 50 Hz ac (sinusoidal) voltage, but also voltages of various nature (such as square or triangular) at different frequencies. The downside of this PEA system, however, is that the maximum output voltage from the high voltage amplifier is only ± 20kV.

4.4.1 Point-on-wave

AC space charge measurement using this PEA system is also achieved by the point-on-wave approach. As the computer has direct control over both the high voltage supply and the triggering of the high voltage impulse, it is therefore possible to synchronise the measurement of space charge at the specific point of the ac waveform. This eliminates the need to monitor the ac waveform as in the case of the LIPP system which requires a capacitor divider to achieve this.
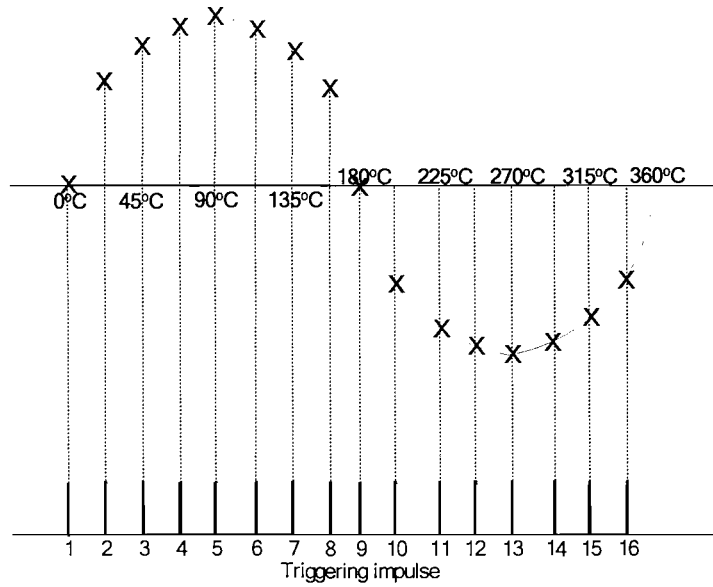
Figure 4.5: Point-on-wave for AC PEA system

Measuring on different phase of the ac waveform will yield output of different magnitude. Consider a 50 Hz ac wave,

Period = 1/freqency

= 1/50 Hz

= 20 msec,

and if a measurement is required at every $22.5°$, a total of 16 points on the ac wave are needed. As such, the time interval between each point, τ will be

τ = 20 msec/16

= 1.25 msec

This suggests that the voltage pulses must be applied with precision during ac space charge measurement as only mere 1.25 msec separates the adjacent points.

As mentioned before, the output of a PEA system has poor SNR and hence requires averaging of a number of measurements. For 50 Hz ac sinusoidal waveforms, the number, say 500, means that it will take 8000 cycles of the waveform for a 16 points measurement (16 points x 500 =8000 cycles), which translate to 160 seconds (8000 cycles x 20 msec). It should be noted that because of the averaging, the point at $0°$

and 360 $^{\circ}$ are effectively the same, which explains why the LIPP has 17 points of measurement while the PEA has one point less as shown in figure 4.5.

4.5   Comparison between PEA and LIPP

Both techniques have their advantages and disadvantages. For example, the PEA system has an advantage in that the output signal is electrically isolated from the sensing and measuring circuit. This protects the amplifier and measuring devices from sudden surge in output signal in the event of electrical breakdown. Indeed, it is this factor that made it possible to measure the space charge in samples before, during and after electrical breakdown [107]. Furthermore, as the acoustic pulse is generated internally, there is no problem associated with target ablation as in the case of the LIPP. Perhaps the biggest advantage of the PEA is the cost of the system which is substantially cheaper than LIPP.

On the other hand, the main advantage of LIPP lies in that the actual distribution of a space charge profile can be analysed directly from the output signal of the LIPP, while the output signal of the PEA system, as discussed earlier, requires the deconvolution process. Another advantage of the LIPP system is due to its high power laser, it is a "one-trigger one-measurement", while the PEA requires the averaging of a number of measurements to obtain a good signal-to-noise ratio output.

In recent years, there has been on going research in improving the performance of PEA systems, so much so that some of the typical short-comings which were mentioned above has been lifted. The most common criticism of PEA is the time it takes to get a clear averaged signal. The earlier PEA system requires about 30 seconds to obtain such an averaged signal which is considered too long to observed dynamic change in space charge distribution [108]. However, it has been reported a system developed by Maeno et al was able to obtain a clear averaged signal with just an averaging number of 64 which translate to approximately 0.4 seconds [108].

As mentioned earlier, with the point-on-wave technique, the time taken for the measurement of ac space charge is about 160 seconds. It can be argued that any space

charge trapped in the bulk would likely to have changed in magnitude and position during this 160 seconds time span, rendering the method inappropriate. Wu et al, have developed a system with a measurement time of merely 4 seconds [109].

In addition to the above mentioned improvements, Fukunaga et al has successfully developed a PEA system capable of measuring charge in three dimensional space [81], while Maeno [110] has developed a portable PEA system which has the added bonus of obtaining the space charge profile without the need of the deconvolution process.

It is important to recognize that both the LIPP and PEA techniques have their pros and cons and the choice of which technique to use depends solely on measurement conditions and requirements. A detailed comparison between these two methods can be found in [111].

4.6   Conclusion

This chapter reports on a PEA system that is capable of measuring space charge in a dielectric sample under both dc and ac electric stress of various frequencies. The concept of point-on-wave measurement as applied to measurement of ac space charge was also presented.

As a result of the system response of the PEA system, there is distortion to the output signal. A data processing treatment known as deconvolution is required to recover the original signal. The concept of deconvolution was also briefed in this chapter.

Finally, this chapter gave comparison between the PEA and LIPP system and some of the improvements made in the development of the PEA system in recent years. It was concluded that both the LIPP and PEA has their strengths and short-comings and the choice of technique solely depends on measuring conditions and requirements.

5 Space charge in planar samples using the LIPP (Part 1): Heat treatment of crosslinked polyethylene and its effect on morphology and space charge evolution

5.1 Introduction

Space charge is a phenomenon normally associated with insulation under high dc electric stress. Space charge formation in polyethylene (PE) may result in local enhancement of electric stress which in turn alters the internal electric field distribution from the anticipated value. Accumulated space charge can also result in stored electromechanical energy. All these processes may produce damage through increased number of hot electrons generation, reduction of energy barrier of degradation reaction, bond dissociation, micro-cavity enlargement and internal strains. This may lead to breakdown of the insulation at a stress level below the designated values.

PE has an upper operational temperature of about $70\,^{\circ}C$. This limits its application as an insulating material for underground cables since it is not uncommon for the cables to operate at temperature as high as 90 $^{\circ}C$ [112]. This problem can be largely overcome by crosslinking PE to form crosslinked polyethylene (XLPE).

However, the additives and by-products of the crosslinking reaction will act as impurities and significantly affect the electrical properties of the insulation. One common method adopted by cable manufacturers to remove crosslinked by-products is to subject the XLPE to moderately high temperature, otherwise known as degassing.

In the past two decades, numerous efforts have been carried out to study the build up of space charge within as-received and degassed XLPE under dc electric stress. However, the majority of work to date has involved comparing the space charge characteristics of as-received and degassed samples [113, 114]. Limited attention has been given to the effect of the length of degassing period and temperature on the dynamics of space charge under dc electric stress.

Apart from removing volatile residual by-products and additives, degassing will also inevitably anneal the material resulting in a change of its morphology [66].

The effects of additives on morphological structure [115] and space charge evolution [90, 92] have been reported by other workers. However, the samples used were procured through careful experimental procedure. This study takes a more practical consideration whereby morphological change is an inevitable result of degassing. This work demonstrates that factors such as degassing temperature, duration and thickness of material can influence the morphology of XLPE insulation and space charge characteristics in the material under dc electric stressing condition.

5.2   Sample details

The samples used for all the experiments are planar samples made using cable grade XLPE material (Borealis XL4201S). The electrodes used were made from XLPE loaded with carbon black (LEO592). Detailed information of Borealis XL4201S and LEO592 can be found in Appendix B.

Firstly, the insulating bulk and semi-con electrodes were made, uncrosslinked, by hot pressing the respective pellets at about 150 ^{O}C. Next, both the front and the rear electrodes were hot pressed into the plaque sample at about 200 ^{O}C for 10 minutes to ensure crosslinking. The samples were subsequently quenched to room temperature with cold water (<10 ^{O}C) running through the hot press.

All degassing was done in a vacuum oven (pressure of 1 bar), after which the samples were cooled, at room temperature for 15 minutes. Details of the samples are shown in table 5.1. It should be mentioned that the term 'thickness', as used in table 5.1, refers to total thickness, i.e. the combined thickness of semi-conducting electrodes and insulating bulk.

	Thickness (mm)	Degassing temperature	Degassed period	Applied Stress (kV$_{dc}$ /mm)
A	3.50	NA	0 hour	33.33
B	3.45	60 ^{O}C	6 hours	34.15
C	3.43	60 ^{O}C	12 hours	34.48
D	3.43	60 ^{O}C	24 hours	34.48
E	3.41	60 ^{O}C	48 hours	34.90
F	3.39	90 ^{O}C	48 hours	30.09
G	1.61	NA	0 hour	28.93
H	1.60	60 ^{O}C	48 hours	29.17
I	1.54	90 ^{O}C	48 hours	30.81

Table 5.1 Sample details

5.3   Experimental protocols

5.3.1   Sample weight measurement

One way to quantify the amount of by-products left in a sample is to determine its weight. Prototypes of samples E, F, H and I were made for this purpose. Their weights were measured at one hour interval during the first 6 hours. After which the weights were only measured at selected intervals of 8, 12, 24, 36 and 48 hours of degassing duration. Weight measurements obtained from each sample were then normalised by its initial weight (i.e. its weight before degassing). As the cooling and re-heating of the samples between each measurement may result in unpredictable changes in morphology, these samples were not used for subsequent tests.

5.3.2   Differential scanning calorimetry (DSC)

The effect of degassing time and temperature on the morphological structure was examined by differential scanning calorimetry (DSC). DSC is a tool used for thermal analysis of various materials. The instrument used, Perkin Elmer DSC7, was calibrated using high purity Indium each time it was used. This is required to prevent possible errors as a result of instrumentation errors such as drift. The temperature was

held constant at 25°C for 1 min and the melting endotherms were collected at a heating rate of 10 °C/min.

5.3.3 Transmission electron microscopy (TEM)

A range of samples were chosen, based on the DSC results, for further morphological examination with transmission electron microscopy. TEM operates on the same basic principles as a light microscope but uses electrons instead of light.

When the electrons travel through a material, some electrons will be scattered and disappeared depending on density of the material. The unscattered electrons then hits a fluorescent screen which gives a shadow image of the material with different parts displayed in varied darkness according to their density.

As TEM uses electrons as its "light source", which has much lower wavelength than visible light, it has a resolution thousand times better than light microscope.

Since TEM works on the principle of electrons transmitting through the material, the samples used must be specially prepared to thickness which will allow electrons to be transmitted through them. For this, the samples were first microtomed at -90 °C to expose a smooth internal surface, then etched with 1% solution of potassium permanganate in an acid mixture composed of 1:4:10 parts of water, phosphoric and sulphuric acids for 4 hours. The etched sample was subsequently quenched in H_2O_2 in mixture of 2 parts sulphuric acid and 7 parts water. The samples were finally rinsed repeatedly in distilled water.

Two replicas of each sample which were prepared separately were examined to ensure that any artefacts introduced by sample preparation could be identified and eliminated.

5.3.4   Space charge measurements

The space charge experiments conducted consists of two parts. First, a step voltage test was conducted to determine the voltage level at which the space charge effect initiates. This is referred to as the threshold voltage or simply V_{th} of the sample.

Voltages were applied from 0 to -70 kV for samples A to E, to -60 kV for sample F and to -35 kV for samples G to I, with a voltage step of -5 kV every 5 secs. The entrance peak was then plotted against the applied voltage.

Immediately following the step voltage test, the samples were stressed under dc voltage conditions at the stress level shown in table 5.1 for a duration of 24 hours at room temperature (25 °C). Space charge profiles, both with and without voltage application, were measured at various times during the ageing period. For smiplicty, they will be termed volt-on and volt-off space charge profiles respectively.

5.4   Results and discussion

5.4.1   Sample weight measurement results and discussion

Figure 5.1 shows the normalised weight of samples of different thickness subjected to different degassing temperatures and durations.

It can be seen that both degassing temperature and sample thickness directly affect the amount of volatile by-products that can be removed. Broadly speaking, it is more difficult to remove volatile additives and by-products from thicker samples. This is evident by comparing line 1 with line 2 and line 3 with line 4. It is worth pointing out that the weights of both 3.4 mm thick samples (lines 2 and 4) continue to reduce even after 48 hours of degassing.
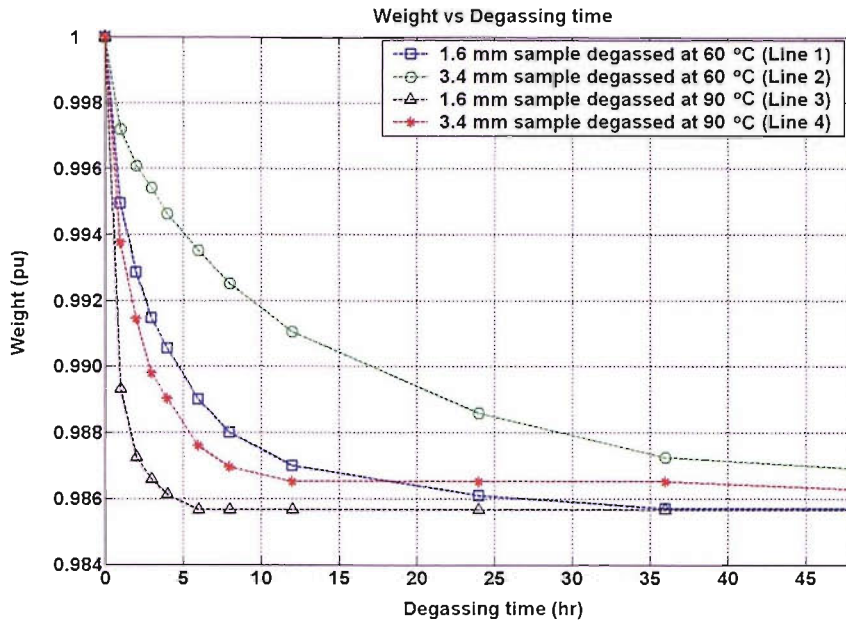
**Figure 5.1: Weight loss to degassing duration ratio of different samples thickness
and degassing temperature**

The degassing process is believed to be governed by Fick's second law which
describes non-steady state diffusion process. From the diffusion equation:

$$\frac{\partial n(x,t)}{\partial t} = D \frac{\partial^2 n(x,t)}{\partial x^2} \tag{5.1}$$

where: n – the concentration of by-products

t -- time

x -- position within the bulk

D -- coefficient of diffusion,

It can be seen that the amounts of by-products at a particular location in the bulk is
dependent on the degassing time. It is perhaps safe to assume that most of the
remaining by-products are located in the middle of the bulk assuming that the initial
by-product distribution is uniform across the sample.

The weight of the 1.6 mm thick sample stabilised after about 6 hours when degassed
at 90 $^{\circ}$C whereas it took about 36 hours for the weight of a sample of the same
thickness to stabilise when degassed at 60 $^{\circ}$C. This is because the diffusion is

thermally activated process driven by the concentration gradient. The thermal activation is reflected by temperature dependence of the diffusion coefficient D in equation 5.1 which can be expressed as [116]:

$$D = D_0 \exp(-\frac{Q_d}{kT}) \tag{5.2}$$

where D_0 – temperature independent constant

Q_d – the activation energy for diffusion

k – Boltzman constant

T – absolute temperature

Both D_0 and Q_d are dependent of host matrix and individual by-product. The diffusion rate increases rapidly with increasing temperature. The weights of both 1.6 mm samples are approximately the same after 36 hours of degassing; suggesting that the amount of volatile by-products left is comparable in both.

It should be mentioned that the diffusion coefficient of the semi-con electrodes and insulating bulk may most probably be different and as such equations 5.1 and 5.2 may not be perfectly applicable throughout the entire sample. Furthermore, the diffusion coefficient of different by-products of crosslinking agent such as acetophenone, alpha methylstyrene, cumyl alcohol and water may also be different.

It is possible that, due to the geometry of the samples, a non-null steady state concentration of by-products was reached even after degassing for 48 hours. However, for simplicity, when solving equation 5.1, a few assumptions were made:

1) Diffusion coefficient between semi-con electrodes and insulating bulk is assumed to be constant for all crosslinking by-products.

2) The DCP content in semi-con electrode is assumed negligible. Any crosslinked by-products present in the semicon is assumed to be due to matrix crosslinking or diffused from insulation.

3)   There exist a null steady state weights for both 1.6 mm and 3.4 mm samples; the ratio of their initial to null steady state weights are assumed (from figure 5.1) to be 0.9858 p.u. and 0.9862 p.u. respectively.

Based on these assumptions the concentration of by-products in the insulating material was estimated to range between 1.41 to 1.43%. This is a fairly reasonable number compared to the typical 2% of DCP content in cable graded XLPE [59-60]. The diffusion coefficients of degassing temperature at 60 ^{O}C and 90 ^{O}C were found to be approximately 0.08000 m^2/s to 0.38626 m^2/s respectively. It should be pointed out that the diffusion coefficient is not thickness dependent. Derivation and solution of the diffusion equation can be found in Appendix C.

The discrepancy in the concentration of by-products and DCP content may suggest that there is a non null steady state concentration of by-products in the samples. Indeed, there has been reported that by-product from crosslinking still exist in much thinner XLPE samples (< 200 μm thick) even after degassing at 80 ^{O}C for 7 days [113].

The weight loss to degassing curves based on the diffusion equation is shown in figure 5.2.
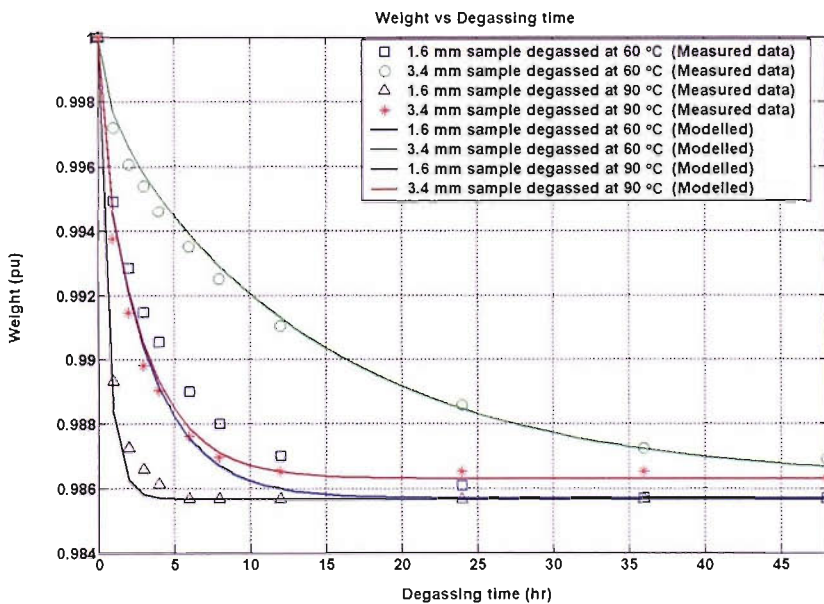
Figure 5.2: Weight loss to degassing duration curves based on the diffusion equation

As seen in figure 5.2, the curves fit very well for the 3.4 mm thick samples but not so for the 1.6 mm thick samples. The exact reason for this is not known and further investigation is required. Nonetheless, for the purpose of this study, a sufficiently good fit was obtained for the 3.4 mm thick sample degassed at 60 $^{\circ}$C and also the final weight per unit of all the samples matches the measured values for those samples on which space charge experiments were undertaken. Using the diffusion coefficient of 0.08 m^2/s, the distribution of by-product concentration of samples A to E were modelled and shown in figure 5.3.

It can be seen that apart from sample A, the rest the samples takes a sinusoidal-shaped distribution, symmetrical about the middle of the sample. The amount of by-product concentration decays exponentially with degassing duration. It must be noted that the distribution is the combination of all the components of crosslinked by-products. Attempt made to estimate concentration of individual crosslinked by-products components with the Fourier Transform Infra-Red (FTIR) spectroscopy was unsuccessful. This is probably due to the samples being too thick for the FTIR spectroscopy.
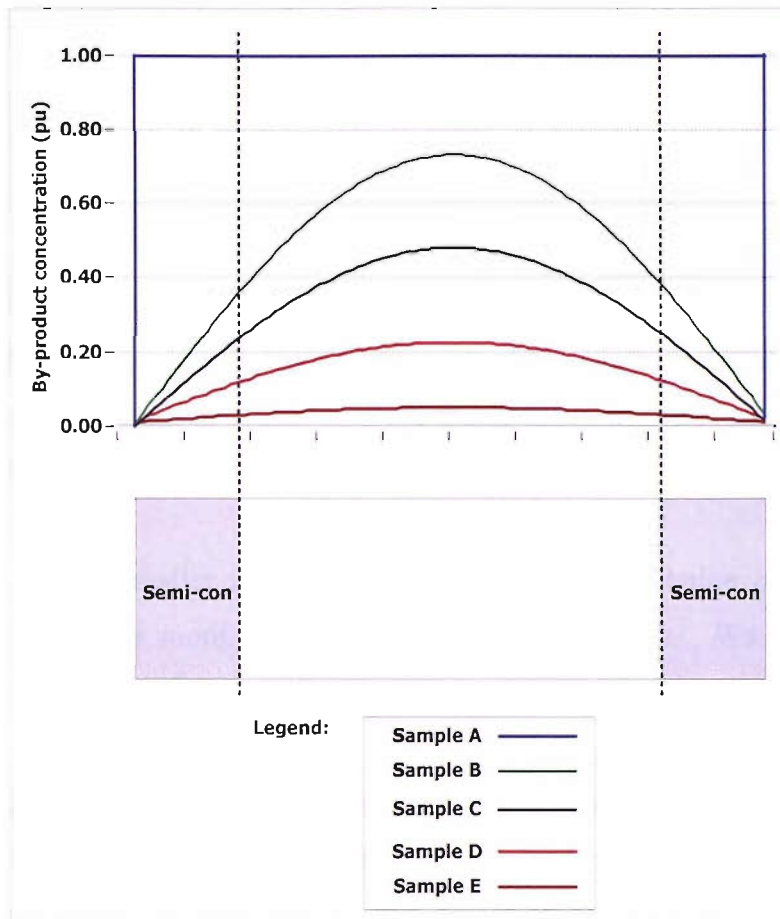
Figure 5.3: Estimation of by-product distribution in samples A to E based on the diffusion equation

5.4.2 DSC results and discussion

From the previous section, it is obvious that subjecting the samples to moderate heat removes volatile by-products. What is less apparent, however, is that the morphology of the sample may also be modified due to an inevitable annealing effect. Annealing results in modification of the microstruture of a material by heat treatment. This usually involves the melting and recrystallization of smaller crystallities into bigger crystals or thickening of the crystals that were already formed. Generally, annealing result in softening of materials through removal of crystal defects [116].

Figure 5.4 compares the DSC melting behaviour of as-received samples (samples A and G) and the samples that were degassed at 60 °C for the periods indicated in table 5.1.

Apart from samples A and G, whose melting behaviour is indicative of quenched polymer, the other samples all exhibit a number of features, i.e. a small endothermic peak, between the 73 to 78 $^{\circ}$C temperature range, is superimposed on the quenched peak at about 103 $^{\circ}$C.

Comparing the melting traces of samples A to E, it can be seen that the temperature at which the smaller peak occurs tends to increase with length of degassing. This is because with increasing degassing duration, the time for re-organization of crystals also increases.

The addition of the smaller peak suggests that another population of crystals was formed and it became more perfect with degassing duration. We can, therefore conclude that annealing of the samples has occurred.

The DSC trace of sample H is rather similar to that of sample E. This is unsurprising considering that they were both degassed at the same temperature (60 $^{\circ}$C) for 48 hours. A closer comparison of the two traces does, however, indicate subtle differences. The first peak is difficult to compare as it largely depends on how it is perceived to be deconvoluted. Nonetheless, the main (second) peak of sample H occurs at a slightly lower temperature of 102 $^{\circ}$C while that of sample E occurs at 103 $^{\circ}$C. This may be due to sample H being quenched more efficiently during cooling to room temperature, as it is thinner than sample E. However, this could be either due to quenching from crosslinking or degassing processes. A quick comparison between the DSC traces of samples A and G indicates similar difference in the occurrence of the main peak. This may suggest that the quenching after the crosslinking process is responsible for the difference observed.

Nevertheless, these results need to be treated with caution as the differences are small and may be due to slight inconsistency in sample preparation and/or measurement artefacts. Examination of the lamellar morphology should shed more light on it.
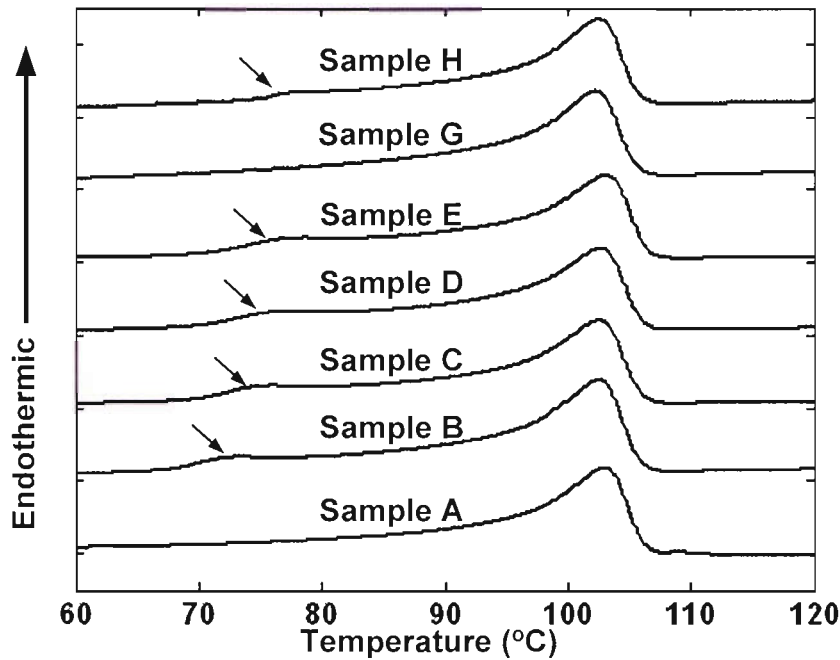
Figure 5.4: DSC melting traces of samples A to E, G and H – samples degassed at 60 °C
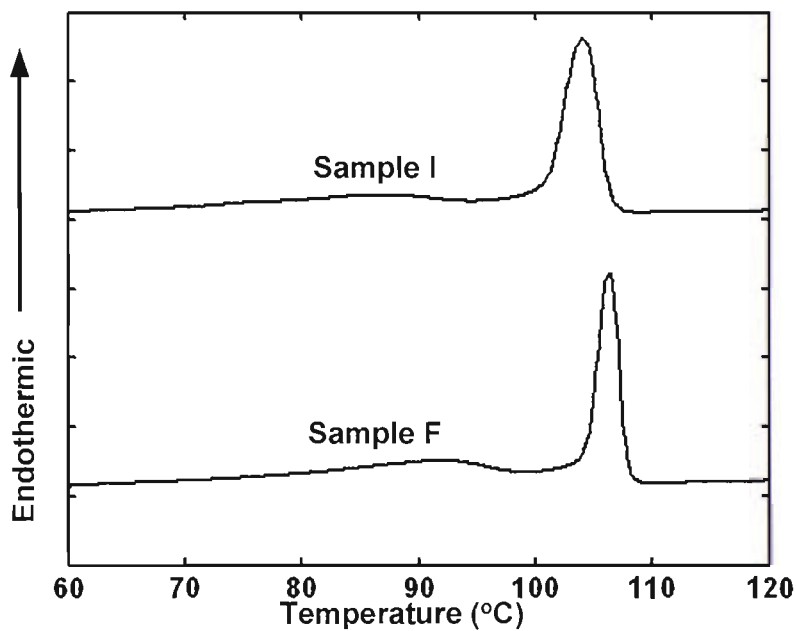
Figure 5.5: DSC melting traces of samples F and I - samples degassed at 90 °C for 48 hours

Figure 5.5 shows the DSC melting behaviour of samples F and I. These are samples degassed at 90 °C. Similar to samples B to E, the DSC scan of samples F and I also exhibits two transitions. However, the smaller peak occurs at a higher temperature of

60

about 91 and 87 °C respectively. The temperature at which the main peak occurs also shifted to about 106 and 105 °C respectively. This may be due to the thickening of the existing crystals. The lower melting peaks of sample I suggest faster quenching as it is thinner than sample F.

These higher transition temperatures suggest that the crystals formed within samples F and I are of thicker quality as a thicker crystal generally has a higher melting temperature. It is noteworthy that degassing samples at 90 °C modifies the DSC traces more significantly than when degassed at 60 °C.

5.4.3   TEM results - Lamellar morphology

Based on the DSC results, a few samples were selected for detailed morphological examination.

5.4.3.1 Sample A - Untreated sample

Figure 5.6 shows TEM micrographs of sample A. As it is an untreated sample, it can serve as a reference for all the samples that follow.
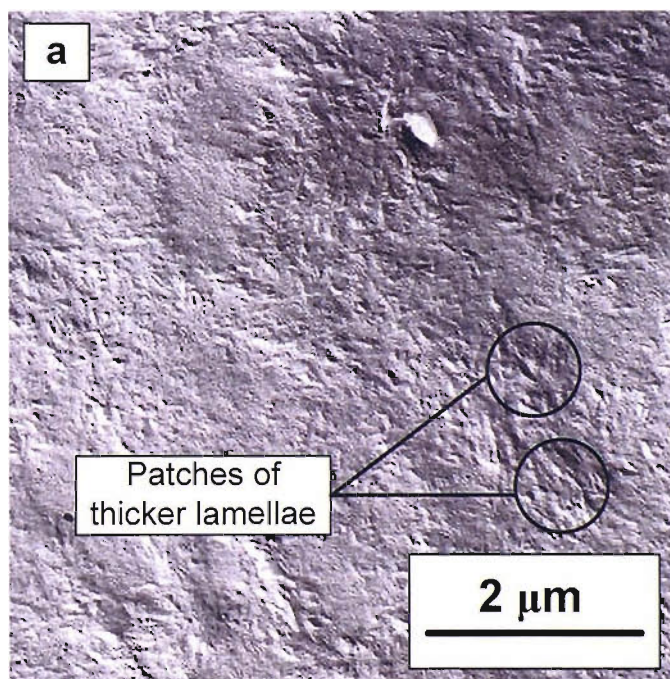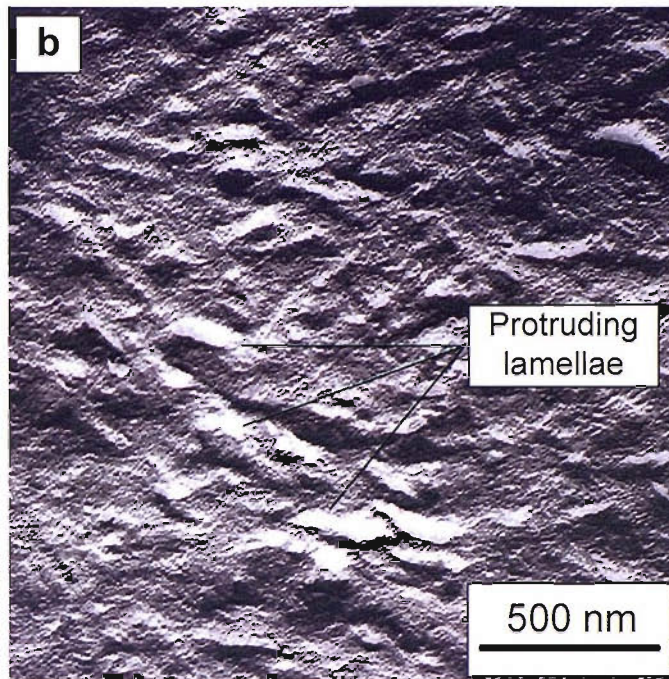
Figure 5.6: Transmission electron micrographs of sample A - untreated

With reference to figure 5.6(a), it can be seen that the patches of apparently thicker lamellae are dominant together with a smaller number of less textured regions. There is no obvious spherulitical structure, suggesting rapid quenching without annealing.

On closer inspection, the patches appear to be lamellae protruding from the surface, as shown in figure 5.6(b). The underlying texture is rather uniform with distinct small lamellar crystals.

Overall, the texture of the sample is consistent with that of a rapidly quenched polyethylene [117], but with a slight inhomogeneity in the microstructure evident by a minority population of larger, and possibly thicker, crystals.

5.4.3.2 Sample E – Degassed at 60 $^{\circ}$C for 48 hours

Figure 5.7 shows TEM micrographs of sample E, which was degassed at 60°C for 48 hours.
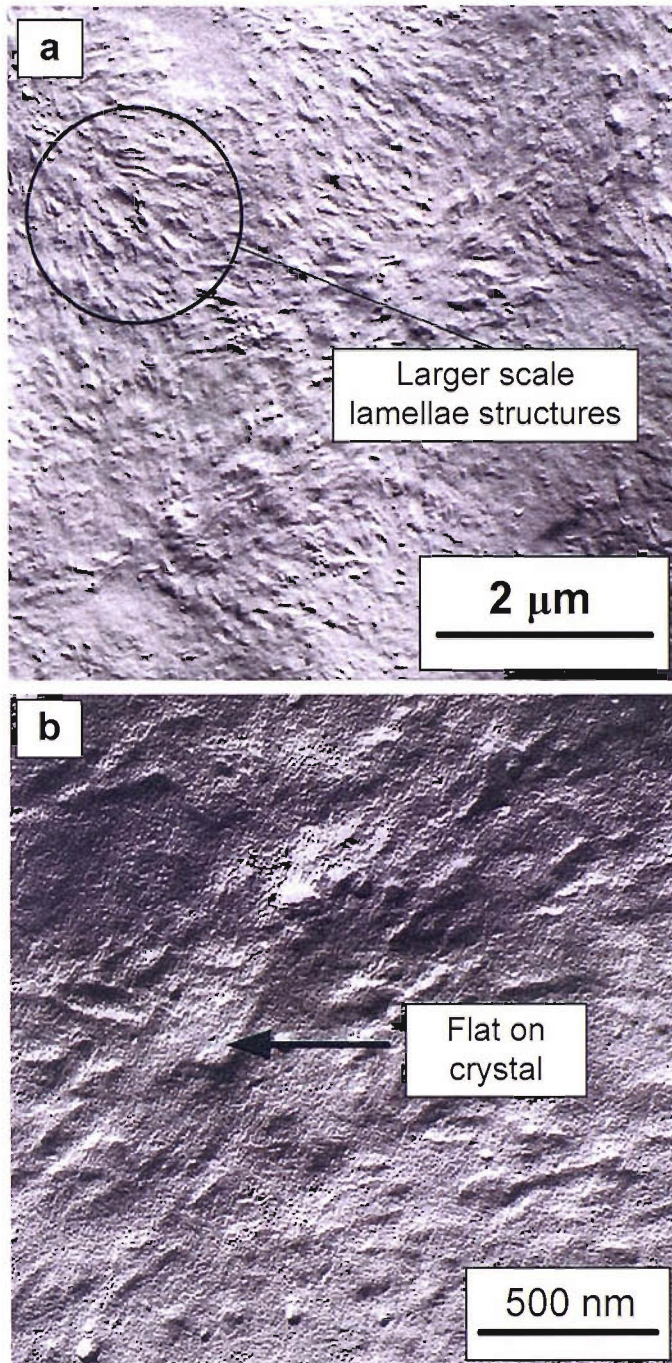
Figure 5.7: Transmission electron micrographs of sample E – degassed at 60 °C for 48 hours

With reference to figure 5.7(a), the texture of sample E is generally similar to that of sample A. However, the larger lamellae appear to be more prominent than those in sample A and, overall, there is increased evidence of lamellae being organised into larger scale structures. Both these features provide evidence a degree of annealing having taken place.

63

Figure 5.7(b) shows that the underlying texture consists of very small crystals punctuated by a small number of larger crystals, some of which appear to be flat on as arrowed.

Overall, the microstructure appears to be similar to that of sample A with a little more distinction between the larger crystals and the underlying material.

5.4.3.3 Sample F – Degassed at 90 °C for 48 hours

Open sheaf-like structures are seen in sample F, as illustrated in figure 5.8(a). There are two distinct populations of lamellae- the coarser and larger lamellae, which are organised into clusters, and the underlying texture of finer lamellae.

A quick comparison with figure 5.6(a) clearly shows that sample A does contain some indication of such features, they are by far less distinct. Figure 5.8(b), further emphasises the clear distinction between the two types of crystals.

Figure 5.8(c) shows the edge of an open crystalline aggregate in which the lamellae appear to diverge from the bottom of the left of the figure. As in sample E, many of the larger lamellae appear to lie flat on, within the plane of view.

Overall, the microstructure of sample F shows thicker lamellar texture with a higher degree of local organization than that of samples A and E. This and the clear distinction between two populations of lamellae suggest that annealing has indeed taken place.
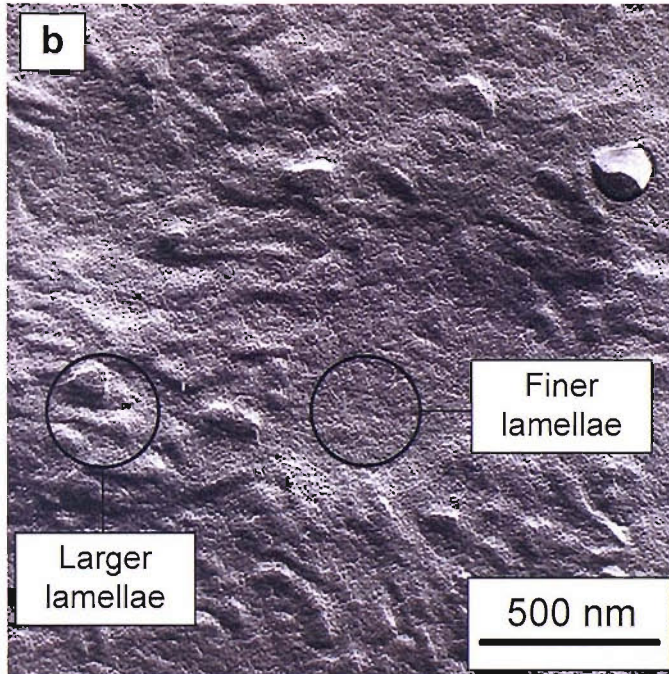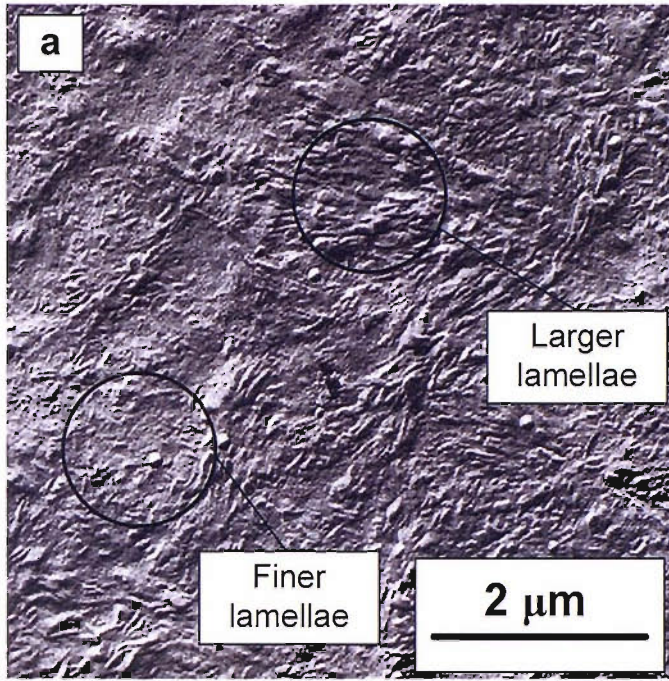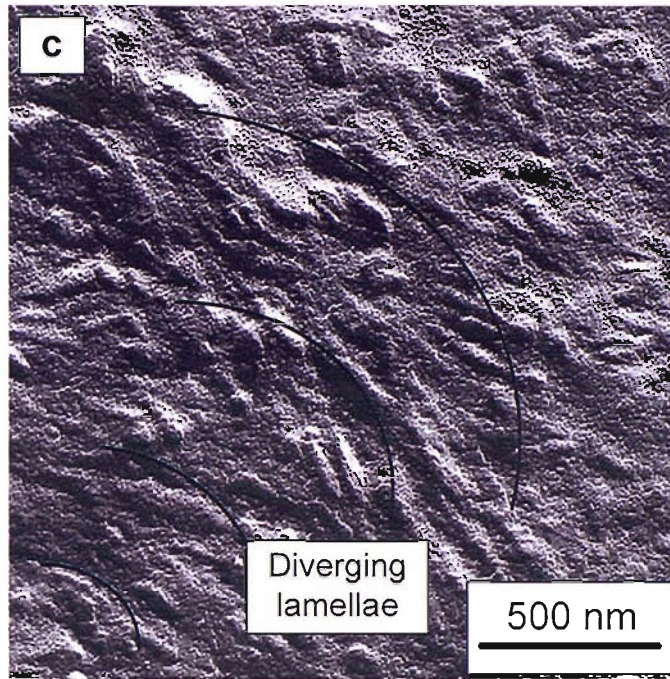
Figure 5.8: Transmission electron micrographs of sample F – degassed at 90 °C for 48 hours

5.4.3.4 Sample H – Thinner sample degassed at 60 °C for 48 hours

Figure 5.9 shows TEM micrographs of sample H which was degassed at 60°C for 48 hours.
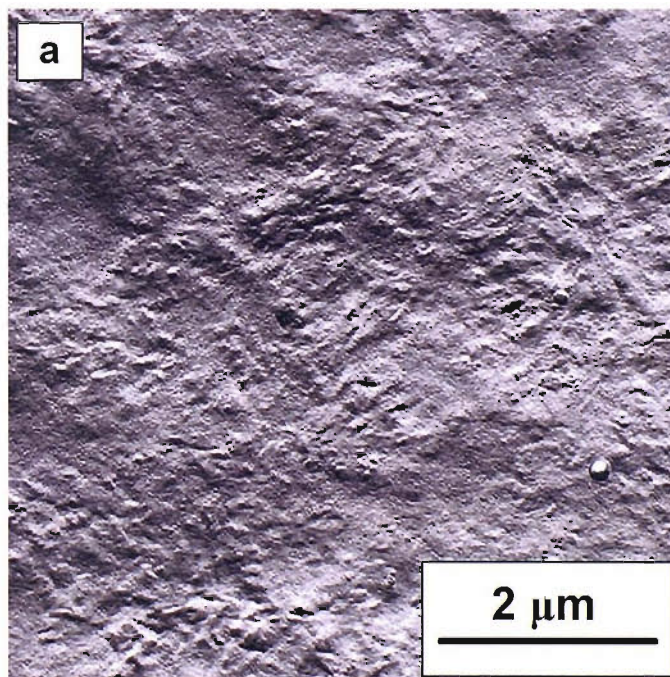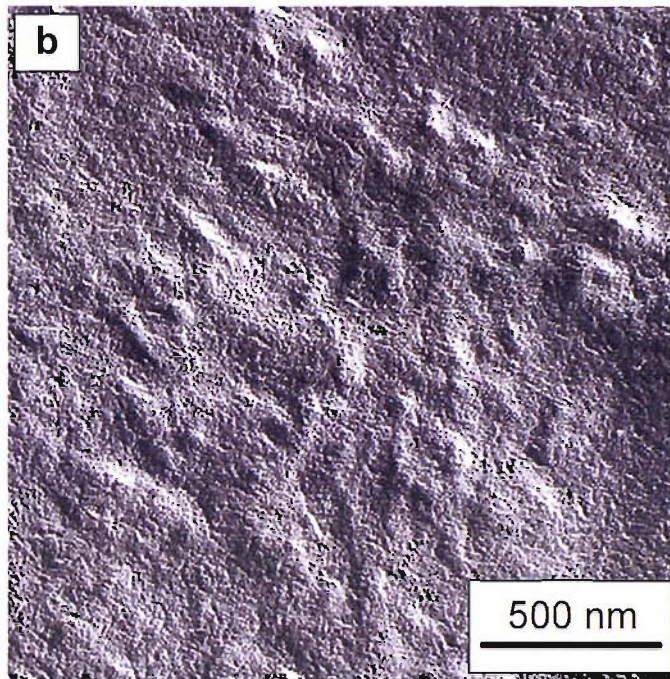
Figure 5.9: Transmission electron micrographs of sample H (thinner) – degassed at 60 °C for 48 hours

A comparison of figures 5.8 and 5.9, suggests coarsening of texture has not occurred to the same extent in sample H as in sample F. The demarcation between the two types of crystals is much less obvious in the current sample and, while there is clustering of more extensive lamellae, the resultant structures cannot be described as spherulitic.

A careful comparison of microstructure of this sample with the three previous ones seems to indicate a better match with sample E, in terms of the overall clarity of the lamellar types, which is unsurprising given the identical processing route employed.

To summarise, the length and temperature of which degassing is carried out have a direct effect on the morphology of the XLPE material. The thickness of the samples, while subtle, may also play a small role in the morphology of the XLPE material, through changes in quench rate.

5.4.4 Space charge results

5.4.4.1 Step voltage test

Figure 5.10 illustrates the entrance peak current of the volt-on space charge signal from the LIPP against the applied voltage during the step voltage test for all samples listed in Table 5.1.
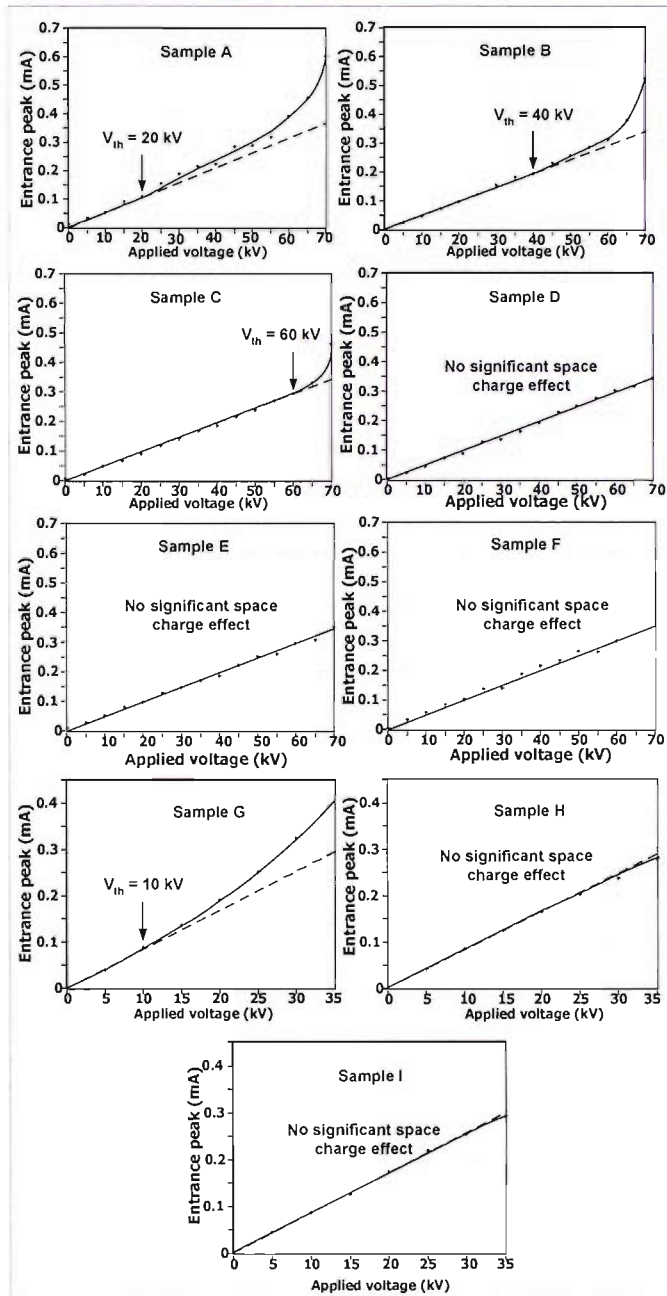
Sample	A	B	C	D	E	F	G	H	I
V_{th}/kV	20	40	60	>60	>60	>60	>35	>35	>35

Figure 5.10. Results of step voltage test of samples A to I.

In the absence of space charge in the bulk, the current amplitude of the entrance peak and exit peak should be proportional to the applied electric field or voltage [68].

The curves of the entrance peak current for samples A to C all deviate positively from the extrapolated trend line. This suggests that heterocharge (or charge of the opposite polarity) has accumulated near the anode, causing an increase in interfacial stress. It can be seen that the longer the sample was degassed, the higher the threshold voltage, V_{th}. This is because longer degassing periods remove more crosslinking by-products, as indicated by figure 5.1. Figure 5.3 further illustrates that with increasing degassing duration the amount of by-products, particularly near to the insulation/semicon interface, reduces. These result in an increase in the threshold stress for ionic dissociation processes (i.e. heterocharge formation) in the bulk insulation as not only the amount of by-product concentration reduces but, perhaps more importantly, the reduction is mainly at the insulation/semicon interfaces.

On the other hand, in samples D to F, the plot of entrance peak current against the applied dc stress follows the extrapolated straight line, indicating that no significant charge has been formed close to the anode. This is probably because the amount of by-product left in samples D and F were largely removed by degassing and whatever was remaining were mainly at the middle of the samples as shown in figure 5.3. As such, it may take a longer time or higher stress before any appreciable heterocharges can be formed.

The V_{th} of sample G was observed to be about 10 kV. With its thickness reduced by approximately half, the V_{th} of sample G has also reduced by half as compared to sample A. This is unsurprising, since both samples were made from same material and processed identically.

Just like samples E and F, no significant space charge effect can be observed in samples H and I, due to the removal of most of the by-products.

5.4.4.2 DC ageing test

All the samples were electrically aged for 24 hours after the ramp tests, and the volt-off space charge profiles are shown in figure 5.11. It can be seen from the 0 hour volt-off space charge profiles of samples A to C (i.e immediately after the step voltage test), heterocharges can be seen at both ends of the electrodes. These charges were accumulated during the step voltage test. The fact that no charge is seen during 0 hour in samples D and E further verifies the results of the step voltage test.
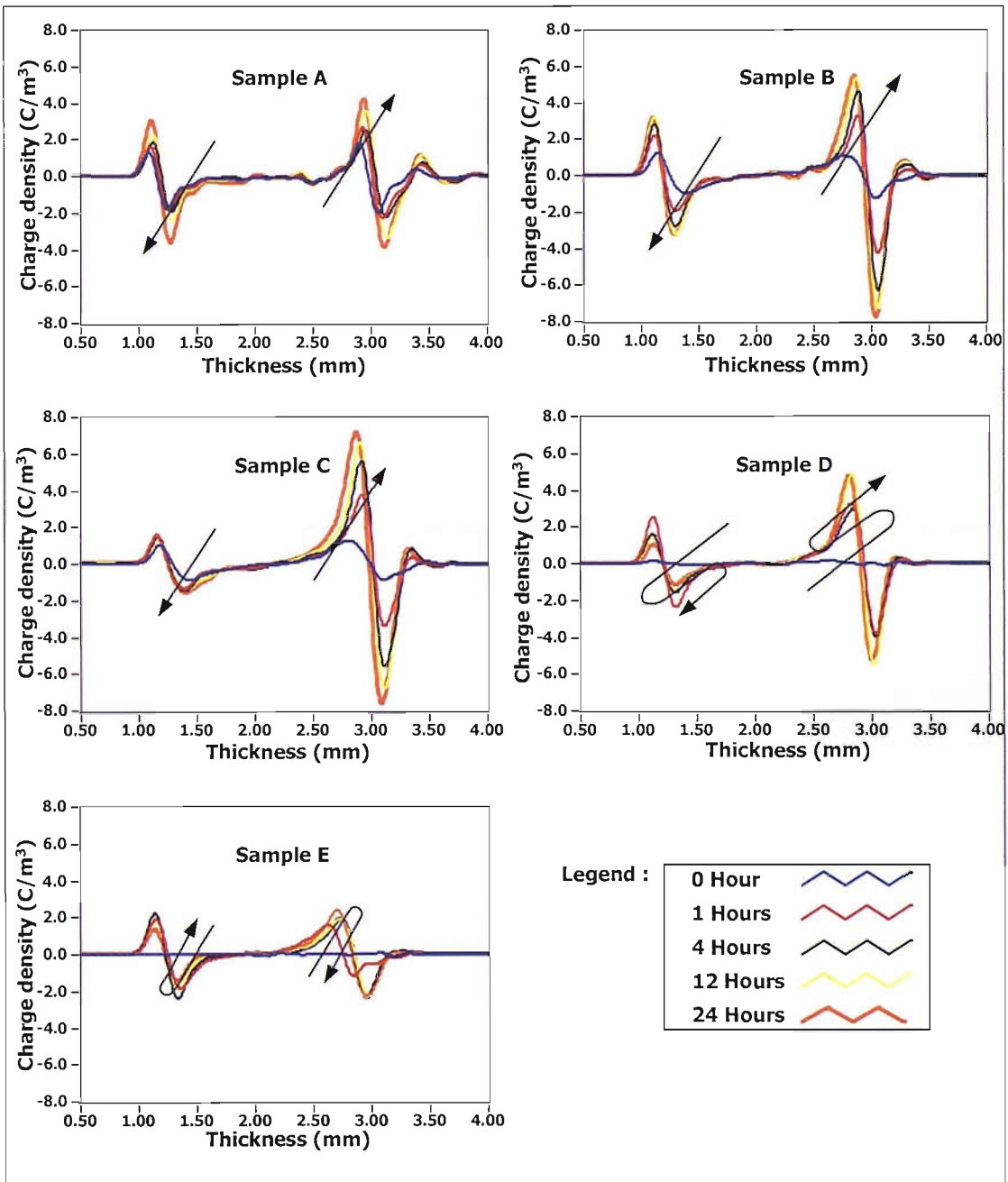
Figure 5.11. Volt-off space charge profiles of samples A to E

After 1 hour of aging, however, samples D and E also indicate heterocharges at both ends of the electrodes. This suggests that after 1 hour of ageing, ionic dissociation and not charge injection/extraction is the dominant process in samples A to E.

Careful observation indicates that the evolution of space charge in samples A to C follows a similar trend, in that the heterocharge accumulation near the electrodes increases with stress period. Samples D and E, however, show a reduction in heterocharges at both electrodes after 2 hours of ageing. Clear evidence of this can be seen in figure 5.12 which shows the integration of the charge densities, Q, across the bulk calculated using equation 5.3

$$Q(t) = \int_{0}^{d} \rho(x,t) S dx \qquad (5.3)$$

where: d = sample thickness

x = position within the bulk

S = electrode area,

This could be attributed to the amount of by-products that is left in the samples. Line 2 of figure 5.1 suggests that there is quite a substantial amount of volatile by-products in the samples when degassed at 60 $^{\circ}$C for a period of 12 hours or less as in the case of samples A, B & C. Hence ionic dissociation is dominant throughout the entire ageing process.

On the other hand, relatively more by-products have been removed when the degassing period is 24 hours or more (samples D and E). Therefore, after 2 hours of electric ageing, most of the remaining by-products have already been dissociated while injection of homocharge continues to occur at both electrodes. This homocharge will cancel out some of the heterocharge near the electrodes.

Looking at figures 5.11 and 5.12, it becomes apparent that space charge in samples A to C is dictated by ionic dissociation. Results from samples D and E indicate a

hybrid of two processes, with ionic dissociation dominant during the first 2 hours and charge injection thereafter.
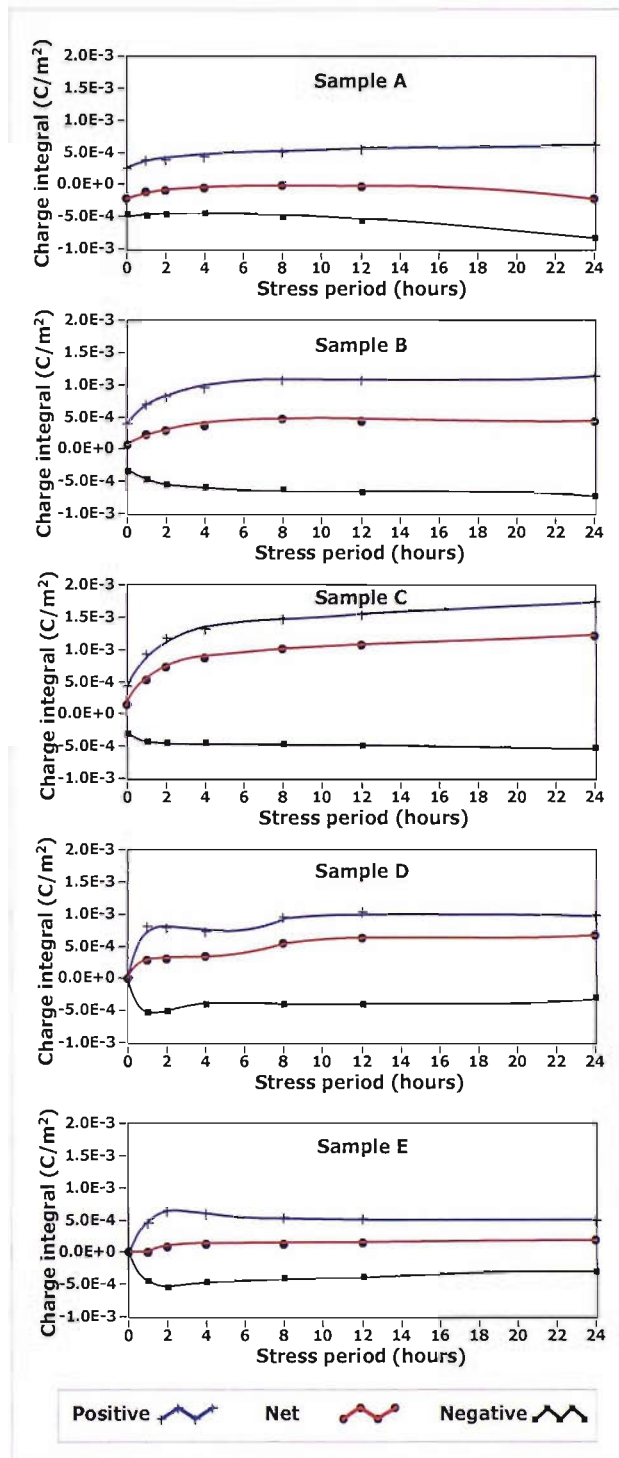
Figure 5.12. Charge integral of space charge in samples A to E

A few points can be made concerning samples A to C from figures 5.11 and 5.12. First, the rate of space charge formation in the bulk increases with degassing period

within the first 2 hours of dc ageing. Second, the amount of positive charge in the bulk increases with degassing period. Third, with increasing degassing duration, the negative charge accumulated in the material tends to spread towards the middle of the bulk while the positive charge remains close to the cathode. These results are rather unexpected, since sample A has the most crosslinking by-products and should therefore contains more charge, as a result of dissociated ionic pairs.

One possible cause of this is difference in electrical conductivity of the XLPE material. The by-products generated from crosslinking include acetophenone, alpha methylstyrene, cumyl alcohol and water. It has been reported that acetophenone generates ionic charges in XLPE when coexist with water [113]. There are also reports that acetophenone increases conductivity such that carrier transport becomes accelerated [76, 77, 118-122]. Therefore, it is more difficult for sample A, which has more by-products and therefore higher conductivity, to trap charge than sample B and sample C.

In order to explain why negative charge tends to spread towards the middle of the bulk, the following proposition can be made.

It has been reported [121] that it is easier for positive charge to migrate from acetophenone-containing region to non-acetophenone-containing regions than negative charge. As explained in section 5.1, which discussed diffusion process, assuming that prior to degassing the volatile by-products in all the samples are homogeneously distributed and that the rate of heat transfer from the two surfaces to the middle of the bulk is equal, one can therefore directly relate the weight loss of the samples to the extent of by-product diffusion in the bulk. This may be the reason as to why by-products concentration in an XLPE cable has been shown to vary as a function of time and insulation radius [123]. In other words, taking the surfaces of the samples as the reference, the effect of diffusion of by-products has occurred to a greater depth in sample C than sample B as illustrated in figure 5.3. This probably explains why for sample C, which has a smaller acetophenone-containing region than sample B, the negative charge tends to spread more towards the middle of the bulk but not positive charge. In fact, since the charge is a result of ionic dissociation of by-

products from the middle of the material, it is therefore more correct to say that the negative charge tends to remain in the middle of the bulk. As such, it is perhaps also reasonable to assume that the negative charge has lower mobility.

Another possible reason as to why negative charge tends to remain in the middle may concern the influence of the positive heterocharge accumulated near the cathode as the relatively higher positive heterocharge in sample C attracts the negative charge towards itself and hence pulling it towards the bulk. There is also the possibility of negative charge near the cathode being neutralised by positive charge injected from the anode.

Space charge activity in samples D and E is dominated by two different processes at different times and hence the explanation used for samples A, B and C may not be completely fitting here. The reduction in charge is most probably due to cancellation effects due to homocharge injection from the electrodes. Notice also that it is positive charge decreases at a lower rate than its negative charge. This could imply that positive charge is more difficult to neutralise and cancel out by negative charge injected from the cathode or less negative charge is injected.

After 12 hours of ageing, the changes in the amount of space charge accumulated in samples A to E very much stablised, suggesting the ionic dissociation, injection and trapping of positive and negative charges has balanced out.

The ageing results indicate that no homocharge accumulation observed in samples A to E within the 24 hours dc ageing period.

One possible reason for the absence of homocharge in samples A to E may be due to the fact that there are still quite substantial amount of by-products left in these samples, despite them being degassed at 60 $^{\circ}$C for 48 hours.

One way of removing more by-products from the sample is to increase the degassing temperature. Sample F is a 3.4 mm thick sample degassed at 90 $^{\circ}$C for 48 hours. The

volt-off space charge profiles and integrated bulk charge trapped inside the insulation bulk are shown in figure 5.13.
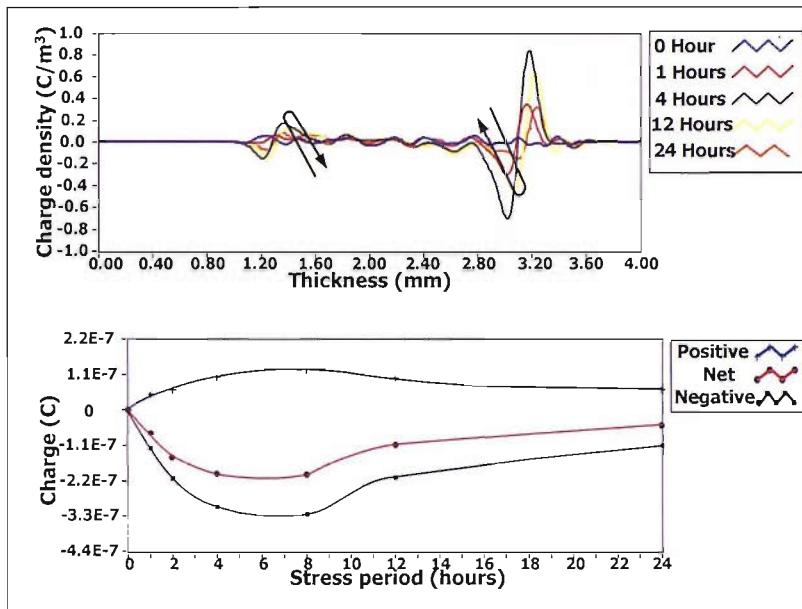
Figure 5.13. Profiles and charge integrals of space charge in sample F

The weight loss ratio (line 4 in figure 5.1) and space charge profiles of sample F indicate that, by degassing the sample at higher temperature, more by-products are removed, resulting in homocharge formation at the electrodes. In such a case, charge injection/extraction is dominant over ionic dissociation.

It is also apparent that the amount of homocharge at both electrodes decreases after about 8 hours of dc ageing. This is probably due to an increase in the bulk stress as a result of homocharge formation during the first 8 hours. This increase in bulk stress will, in turn, ionise the by-products that may still remain in the middle of the bulk which, as mentioned earlier, is probably the area least susceptible to degassing. The heterocharge produced by ionic dissociation will, therefore, cancel out the homocharge at the electrodes.

It is also noteworthy that the rate at which positive charge reduces after the 8 hours ageing period is lower than that of the negative charge. This is in agreement with the earlier statement that positive charge is more difficult to neutralise and cancel out than negative charge.

Another way to remove more volatile by-products is to reduce the sample thickness. Referring to figure 5.1, the weight loss ratio of sample H (line 1) and sample I (line 3) indicates that more by-products can be removed when a 1.6 mm thick sample is degassed at 60 $^{\circ}$C and 90 $^{\circ}$C for a duration of 48 hours respectively. Space charge profiles and the total amount of charge for samples H and I are illustrated in figures 5.14 and 5.15 respectively.
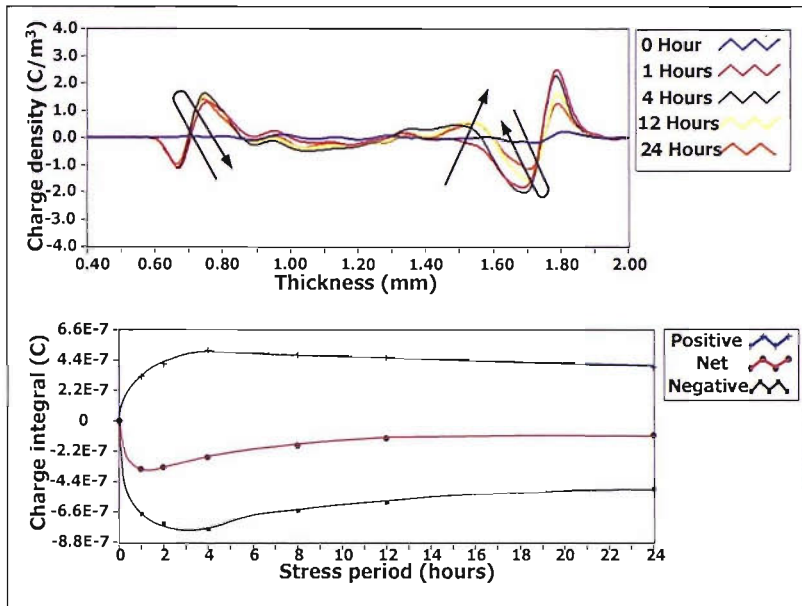
Figure 5.14. Profiles and charge integrals of space charge in sample H.
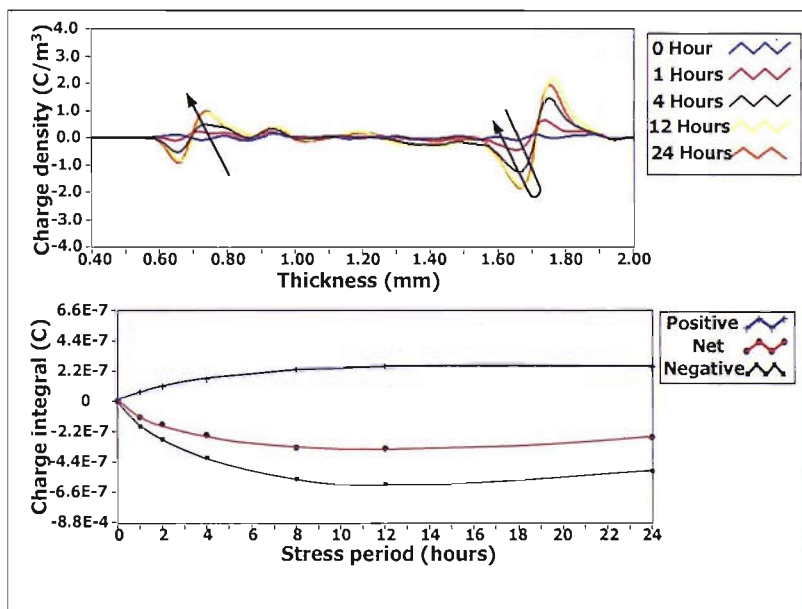
Figure 5.15. Profiles and charge integrals of space charge in sample I.

Obvious similarities can be seen when comparing the space charge profiles of sample F and sample I. Like sample F, sample I exhibits homocharge at both electrodes. Another noticeable similarity between samples F and I is that the net charge is negative throughout, in other words, more negative charge is trapped than positive charge. One possible explanation for this is that it is easier to trap negative charge than positive charge. This is evident by looking at the relatively higher rate of increase of negative space charge in each sample before they start to be cancelled out by the positive charge. Other reasons for the negative net charge could be that more negative charge is injected into the samples than positive charge or it could also be a combination of both reasons.

The main difference between samples F and I is that, in the case of the latter, the amount of negative homocharge only starts to decrease after 12 hours of dc ageing and the amount of positive charge very much stabilizes after 8 hours of dc ageing, emphasizing that positive charge, once trapped, is more difficult to cancel out.

The decrease in negative homocharge in samples F and I is most probably due to cancellation by positive charge. The question to be addressed therefore concerns the origin of the positive charge. One possible source is ionization of by-products in the middle of the bulk. While this may be significant in sample F, it is, however, believed to have minimal effect in sample I seeing that its weight loss ratio has stabilized after only 6 hours of degassing, suggesting that most of the by-products has been removed.

Another possible source of positive charge may be the migration of charge from the anode to the cathode. It is shown that positive charge is more difficult to trap; therefore, relative to negative charge, significantly more positive charge injected will not be trapped at the vicinity of the anode but, rather will be attracted to the cathode and cancelled out and/or recombined with the accumulated negative charge.

Comparing line 1 with line 3 in figure 5.1, it can be seen that the weight loss ratio is very much equal after 36 hours of degassing period. In other words, the amount of by-products in samples H and I is very much the same.

Not surprisingly, sample H also reveals evidence of homocharges at both electrodes. Notice also that, as in samples F and I, sample H also has net negative charge, suggesting that more negative charge is trapped than positive charge.

Although, slight differences, such as the amount of positive and negative charges accumulated and initial (within the first 2 hours) rate of increase of charge, can be seen when comparing the charge integral of samples H and I, the general space charge distributions is similar. Therefore, the difference in morphological structure, clearly revealed by DSC, has little effect on space charge distributions.

5.5 Conclusion

This chapter reports on the space charge characteristics of XLPE plaque samples, degassed for different duration and temperatures, subjected to dc electric stress and the influence of degassing on the morphological development of XLPE samples. Parameters such as degassing duration, degassing temperature and sample thickness were investigated.

While the main intention of degassing is to remove volatile by-products, by subjecting the material to an elevated temperature, annealing effects are inevitable, which modify the morphology of the material.

The resultant complicated space charge behaviour is then attributed to a combination of ionic dissociation, charge injection/extraction, charge transportation, trapping, cancellation and differences between the morphology of each sample.

The main points are:

- The amount and rate at which volatile by-products are removed are dependent on sample thickness, degassing temperature and duration.
- Annealing of material, an inevitable consequent of degassing, result in the formation of more perfect and higher quality crystals and this is dependent on the temperature, duration and, to a lesser extent, sample thickness.

- Annealing of material causes the clustering of crystals groups resulting in formation of coarser lamellar texture with some local organization.
- The dc threshold stress at which space charge initiates increases with degassing period.
- The nature of space charge (i.e. homo or hetero charge) depends strongly on the amount of by-products in the sample.
- The presence and amount of by-products is believed to take precedence over the morphology of the material as far as space charge evolution is concerned.
- Even in the event of comparable by-product concentration, the space charge distribution is not significantly affected by changes to the morphological structure of the material.

In conclusion, space charge distribution is highly dependent on degassing duration, temperature and thickness of the degassed sample.

6   Space charge in planar samples using the LIPP (Part 2): Temperature effect on space charge characteristics in XLPE insulation under DC electric stress

6.1   Introduction

In the previous chapter, the effects of degassing duration and temperature on space charge in XLPE insulation under dc electric stress were studied. However, all the experiments were conducted at room temperature. In fact most of the research work done on space charge has been conducted at room temperature while space charge effect in XLPE under DC electric stress at different temperatures has only received limited attention [43, 64, 92, 112, 124-131].

Obviously, the operational temperature of underground cable is not constant, especially in countries whereby the climatic condition various significantly during different times of the year. It has been reported that the temperature experienced by underground cable can go up to 90 °C [43]. As such, it becomes important to study and attempt to understand space charge dynamics in XLPE under various temperatures.

This chapter reports on space charge evolution in XLPE planar samples subjected to electric stress level of -30 kV$_{dc}$/mm under four temperature conditions of 25 °C, 50 °C, 70 °C and 90 °C. Unlike the previous study, this investigation will be limited to as-received samples and samples degassed at 90 °C for 48 hours.

6.2   Samples details

The samples used were made from the same material and manufacturing procedure as described in section 5.2. The samples are approximately 1.6 mm thick overall and 1.2 mm thick in insulating bulk. All degassing was done in a vacuum at 90 °C for 48 hours and subsequently left to cool at room temperature for 15 mins. Details of the samples are shown in table 6.1

	Testing Temperature	Bulk Thickness	Sample Treatment	Applied Stress
A	25°C	1.21 mm	As-received	
B	50°C	1.17 mm	As-received	
C	70°C	1.25 mm	As-received	
D	90°C	1.26 mm	As-received	$-30\ kV_{dc}/mm$
E	25°C	1.12 mm	Degassed	
F	50°C	1.19 mm	Degassed	
G	70°C	1.26 mm	Degassed	
H	90°C	1.20 mm	Degassed	

Table 6.1: Sample details

6.3 Experimental protocols

The samples were loaded in the sample holder and then placed inside an oven. The temperature in the oven is controlled by a temperature controller. The samples were held at the set temperature for 1 hour before any space charge measurements were taken. This is necessary to ensure that the samples has reached a thermal steady-state as temperature affects the pressure pulse induced by the laser and also the velocity of the acoustic pulse as it transverses across the sample [112, 126].

As like in chapter 5, the space charge experiment also consists of two parts; the step voltage test and the dc ageing test.

6.3.1 Step voltage test

First, a step voltage test was conducted to determine the voltage level at which space charge effect initiates. This is referred to as the threshold voltage or simply V_{th} of the sample. Voltages were applied from 0 to approximately -35 kV, with a voltage step of -5 kV every 5 secs. The entrance peak of the space charge signal was then plotted against the applied voltage.

6.3.2 DC ageing test

Immediately following the step voltage test, the samples were stressed under dc voltage conditions at a stress level of -30 kV_{dc}/mm for a duration of 24 hours at temperatures shown in table 6.1. Likewise, the volt-on and volt-off space charge profiles were measured at various times during the ageing period.

It should be pointed out that when tested at elevated temperatures, degassing of the samples is inevitable. However, considering

1) the current experimental setup; i.e. the samples were pressurized with SF_6 insulating gas and the area whereby space charge was measured (the semicon electrode area) was sandwiched by two metal electrodes (the high voltage brass electrode on the cathode and the aluminum target electrode on the anode) under high pressure and

2) the sample's geometry, which is about 1.6 mm thick and 20 mm in diameter, such that diffusion mainly occurs in one dimension i.e., from the two surfaces,

it can therefore be assumed that diffusion of volatile by-products out of the samples is negligible particularly between the metal electrodes.

Changes in the morphological structures of the samples as a result of difference in testing temperature is also ignored as it has been demonstrated in chapter 5 that such changes has little impact on space charge.

6.4 Results and discussion

6.4.1 Step voltage test

As in section 5.4.1, only the magnitude of the entrance peaks (anode) of the space charge signal is being plotted against the applied voltage. Due to relatively poor signal-to-noise ratio of the exit peak, the magnitude of the noise will be of similar order as that of the actual signal, especially when the applied voltage is small. As

such, any data extracted from the exit peak of the space charge signal may be questionable.

The generation of the pressure pulse is a result of rapid heating of the target surface (in our case the silicone oil). Due to this, the temperature of the target has a definitive effect on the magnitude of the entrance peak. Hence, in order to have a better comparison of the step voltage results, the magnitude of the entrance peak of each sample is normalised the final value obtained during the step voltage test.

6.4.1.2 As-received samples (Samples A to D)

The normalised entrance peaks of the space charge signal against the applied voltage of the as-received samples are shown in figure 6.1.
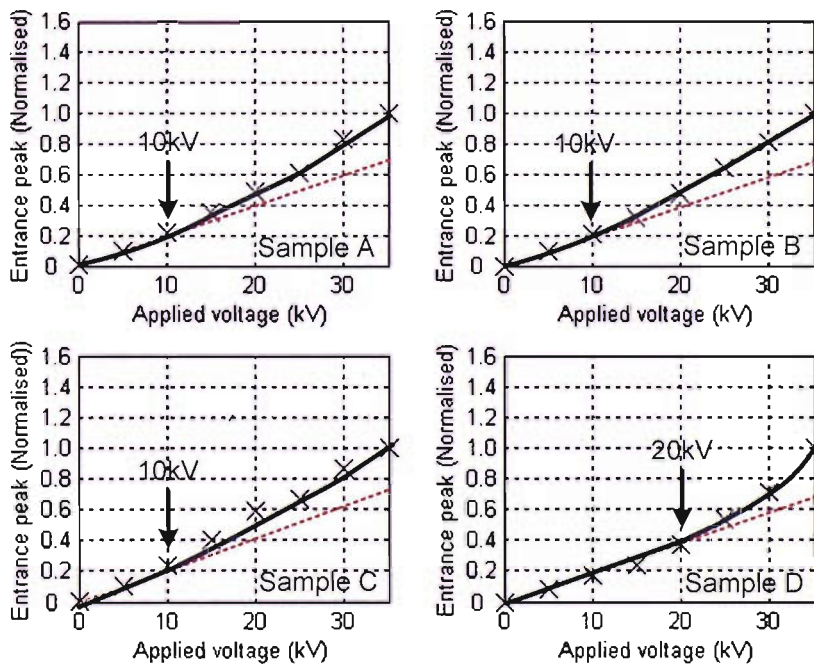
Figure 6.1: Normalised entrance peak (Anode) magnitudes of the LIPP current against the applied voltage of as-received samples

In the absence of space charge, the magnitude of the entrance peak of the LIPP signal should have a linear relationship with the applied voltage. This is represented by the red dotted line shown in figure 6.1

Any deviation from the red dotted line indicates the presence of space charge. A quick look at figure 6.1 suggests that the threshold voltage at which space charge initiates are 10 kV and 20 kV for samples A to C and sample D respectively.

Positive deviation of the curves from their respective red dotted line suggests stress enhancement at the interface. Stress enhancement at the interface is normally caused by heterocharge accumulation in the vicinity of the interface. For samples A to D, negative charge is expected to have accumulated near the anode when the applied voltage is higher than their individual threshold value.

The formation of negative charge near the anode of samples A to D is believed to be caused by ionic dissociation of crosslinked by-products. This is consistent with the results reported in chapter 5 that for as-received samples where ionic dissociation is dominant over charge injection.

For ionic dissociation to occur, energy is required to break the bond holding the ionic pairs together. From the above experimental setup, there are 2 sources of energy: electrical from the applied voltage and thermal from the oven's heat. Bearing this in mind, one would expect the threshold voltage of sample D to be the lowest considering it has the highest thermal energy which contradicts the results of the step voltage test.

In order to explain this, the space charge profile of sample D with applied voltage of 20 kV was further examined.
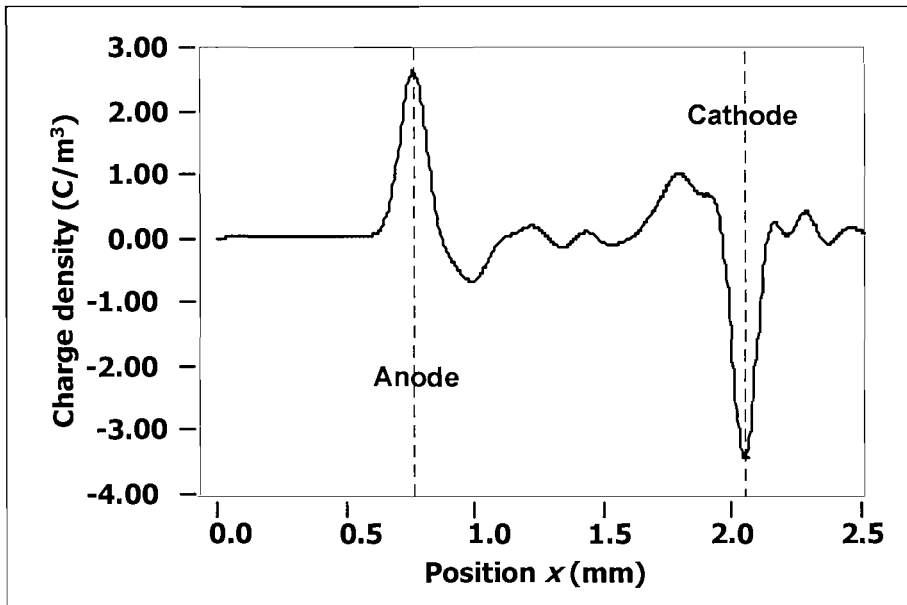
Figure 6.2: Space charge profile of sample D at 20 kV.

Figure 6.2 shows the space charge profile of sample D during the 20 kV stage of the step voltage test. Heterocharges can be clearly seen in the vicinity of both electrodes. As mentioned earlier, the formation of heterocharges normally enhances the interfacial stress. However, this is not reflected on the step voltage experiment. One possible explanation is that the positive heterocharge near the cathode is significantly larger than the negative charge at the anode, masking off its effect on the interfacial stress at the anode.

To confirm this, the electric field distribution across the sample was computed using

$$E(x) = \int_0^x \frac{x\rho(x)}{\varepsilon_0\varepsilon_r}dx \ , \quad 0 < x < d \text{ (where d is the sample thickness)} \qquad (6.1)$$

The electric field distribution across sample D is shown in figure 6.3
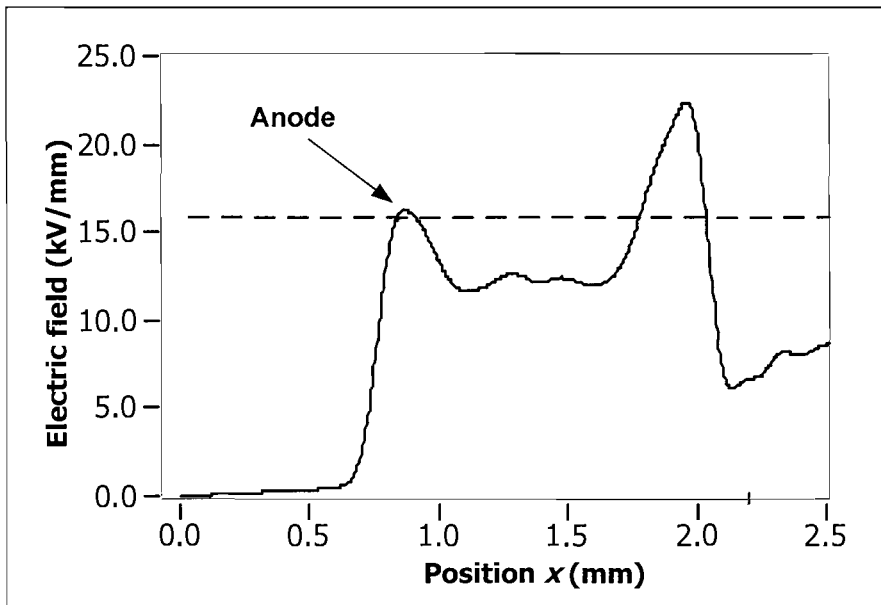
Figure 6.3: Electric field distribution across sample D at 20 kV.

The approximate average electric stress across the sample, that is, the stress across the sample if there is no space charge inside the sample is represented by the blue dotted line. It can be seen that the actual electric stress at the anode, as indicated by an arrow, is almost the same as the average stress despite the presence of space charge which clearly affects the electric field across the bulk and at the cathode. This suggests that the results from the step voltage test should not be used explicitly but to be complemented with space charge profiles and electric field distributions whenever possible.

Although there is no calibration signal for sample D, the space charge signal during the 5 kV step was used as a calibration for the above analysis. While the result cannot be used quantitative but qualitative one is good enough to illustrate that the presence of space charge may not necessarily leads to enhancement of interfacial stress.

Careful examination of all space charge profiles and electric field distributions of the step voltage test revealed that only samples A and B truly reflect the threshold voltage suggested by the test. Sample C, however, indicates space charge accumulation at applied voltage of 10 kV (but no space charge accumulation at 5 kV) while in the case of sample D, the threshold voltage was found to be less than 5 kV. This is probably because the difference in the amount of thermal energy gained by the samples A and

B is not enough to cause any difference in the threshold voltage. At 70 °C, the amount of thermal energy gained is probably big enough to break the holding bonds even at a low applied voltage of 10 kV. Not surprisingly, this effect is even more pronounced in sample D is tested at 90 °C.

6.4.1.2 Degassed samples (samples E to H)

The step voltage results for the degassed samples are shown in figure 6.4.
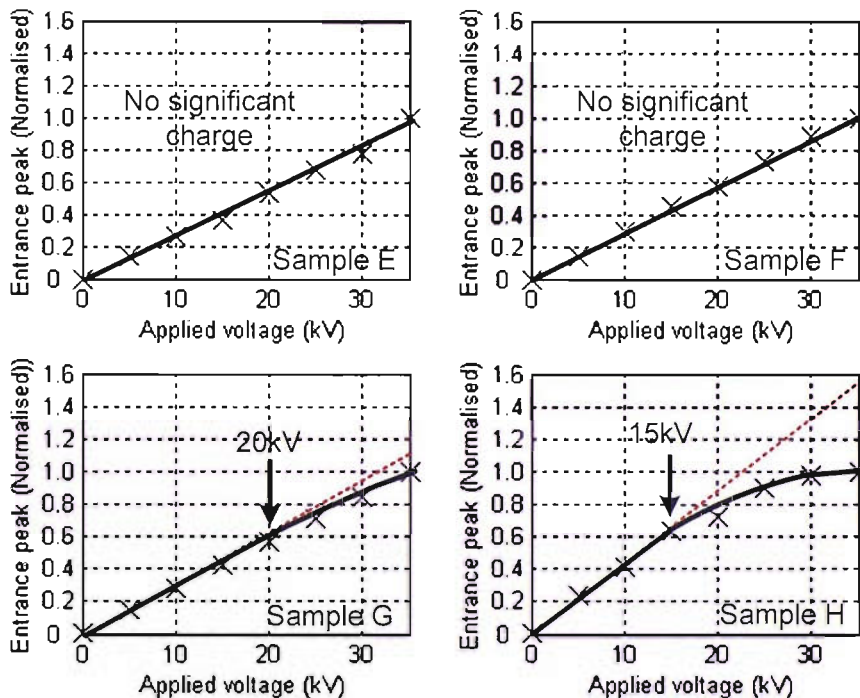
Figure 6.4: Normalised entrance peak (Anode) magnitudes of the LIPP current against the applied voltage of degassed samples

As seen in figure 6.4, the relationship between the normalised entrance peak magnitude and the applied voltage of the samples E and F appears to be linear. This suggests that no significant charge has been formed adjacent to the anode in the degassed samples during the step voltage test up to 50 °C. This is probably due to the reduction in crosslinked by-products from degassing which in turn reduces the amount of ionic pairs that can be dissociated with the applied electric field.

In the case of samples G and H, the magnitude of the entrance peak against the applied stress deviates negatively from the red dotted trend line. This suggests that homocharge has been formed close to the anode. This is believed to be caused by charge injected from the anode to the insulation. By comparing the results of samples of all the degassed samples, it is evident that the threshold voltage of the homocharge formation decreased from above 35 kV to 15 kV as the testing temperature was increased from 25 °C to 90 °C. This suggests that charge injection is enhanced by high temperature.

It is important to highlight the significance of the step voltage test results of sample D. As the threshold voltage was less than 5 kV, there is a problem with choosing the reference signal for calibration purpose. This is because if the applied voltage was less than 5 kV, the signal-to-noise ratio of the output profile would be too poor. On the other hand, if the applied voltage was 5 kV or more, space charge would have already been build up in the sample.

There has been suggestion that the accumulated space charge in the sample, $\rho_{accumulated}(x)$ can be estimated using

$$\rho_{accumulated}(x) = \rho_{volt-on}(x) - \rho_{no-charge}(x) \tag{6.2}$$

where $\rho_{volt-on}(x)$ = volt-on space charge profile with charge
$\rho_{no-charge}(x)$ = volt-on space charge profile with no charge which can be computed using

$$\rho_{no-charge} = \frac{E_{applied}}{E_{cal}} \times \rho_{calibrate} \tag{6.3}$$

where $E_{applied}$ and E_{cal} are the applied stress and calibration stress respectively.

Assuming that the charge in the sample is trapped reasonably deeply such that there is no fast charge, any charge accumulated, $\rho_{accumulated}(x)$, in the sample will be equal to

the space charge profile immediately after the removal of the voltage, $\rho_{volt-off}(x)$. By substituting $\rho_{volt-off}(x)$ for $\rho_{accumulated}(x)$ and rearranging equation 6.2, one has

$$\rho_{no-charge}(x) = \rho_{volt-on}(x) - \rho_{volt-off}(x) \tag{6.4}$$

Hence, under no fast charge condition, the space charge profile with no charge accumulation can be calculated using the volt-on space charge profile and space charge profile shortly after the removal of the voltage (i.e. the volt-off space charge profile). This space charge profile can, therefore, be used as a reference signal for calibration purpose. It must be stressed that this is true if and only if

$$\rho_{fast}(x) = \rho_{accumulated}(x) - \rho_{volt-off}(x) \approx 0 \text{ where } \rho_{fast}(x) \text{ is fast charge} \tag{6.5}$$

Throughout the step voltage test, no volt-off space charge profile was measured until the final stress level of each sample was obtained. Based on the no charge ($\rho_{no-charge}$), the volt-on ($\rho_{volt-on}$) and the volt-off ($\rho_{volt-off}$) space charge profiles immediately after the step voltage test, profile accumulated charge, $\rho_{accumulated}(x)$ can be calculated using equation 6.2, while fast charge, $\rho_{fast}(x)$, can be calculated using equation 6.5. The fast charge profiles of samples A to C were computed and shown in figure 6.5.
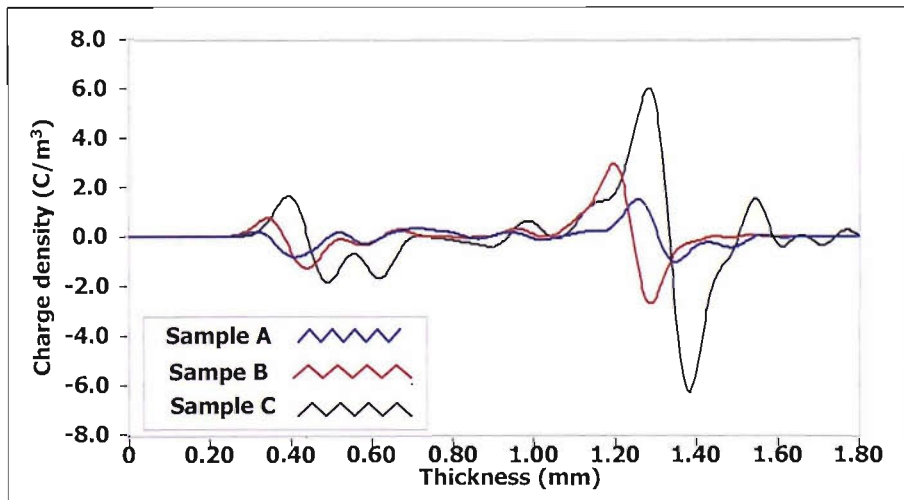
Figure 6.5: Fast charge in samples A to C immediately after step voltage test.

The fast charge of sample D cannot be computed because all the space charge profiles measured show charge accumulation, in other words, there is no observable $\rho_{no\text{-}charge}$. Nonetheless, from figure 6.5, it can be seen that the higher the testing temperature, the more fast charge present in the sample. This is probably due to increase in charge mobility with temperature as reported in [43, 112, 125]. This increase in charge mobility is probably attributed to the fact that charges in sample B have higher energy than that in sample A. Therefore, more of these charges will have enough energy to be detrapped shortly after the applied voltage removed. This effect is even more pronounced in sample C which is tested at even higher temperature.

Although the fast charge in sample D cannot be computed, the above results indicate that the calibration signal cannot be obtained by using equation 6.5 as sample D is tested at the highest temperature of all as-received samples and the amount of fast charge present will be quite significant.

An intriguing topic arises from the above discussion regarding space charge calibration. When measuring space charge in an existing cable or its peelings, often space charge has already accumulated in the material. Under such circumstances, it will not be possible to obtain the calibration signal without first depleting the charge in the sample. Based on the fast charge results of samples A to C, it can be seen that the amount of space charge is small when testing at low temperature. This may suggest that if the testing temperature can be controlled to a reasonably low value, the amount of fast charge can be further reduced.

Furthermore, it has been shown that, within reasonable limits, the amount of space charge in a sample increases with applied electric stress [119, 124]. If one assumes that the proportion of shallow and deep traps in any give sample is constant, hence the amount of fast charge will also be reduced if the applied stress is low. Therefore, if a low electric stress is applied to a charged sample at low testing temperature one can obtain the $\rho_{no\text{-}charge}$ of a sample by using equation 6.4.

It should be stressed that the duration for which the low electric stress is applied to a sample should be short so that the space charge accumulated in the sample is not

affected but must be sufficiently long for a space charge measurement to be obtained, which will be less than a second with most space charge measurement techniques that are available. Experimental work needs to be conducted to confirm the above proposition. This requires further investigations.

6.4.2 DC ageing test

6.4.2.1 As-received samples

The volt-off space charge profiles taken at various times and the corresponding charge integrals, calculated using equation 5.3, of sample A were plotted and shown in figure 6.6. The volt-off space charge profiles can be perceived to be trapped charge as they remained trapped in the sample even after the applied voltage has been removed.

As seen in the volt-off space charge profiles in figure 6.6, heterocharges were trapped in the vicinity of both electrodes. These heterocharges can be seen even at 0 hour (i.e. immediately after step voltage test) and increase with ageing time. This is in agreement with the step voltage result and the results of the as-received samples investigated in chapter 5. These heterocharges are believed to be due to electric stress assisted ionization of crosslinking by-products such as water.

From the charge integral plot, it can be seen that the rate at which space charge was built up reduces with ageing time. This is probably because as the amounts of heterocharges increased, the stress at semicon/insulation interfaces also increased. This increase of interfacial stress enhanced charge injection which neutralised some of the heterocharges that has been accumulated.

It has been shown that fast charge was present in sample A immediately after the step voltage test. Furthermore, it was clearly illustrated that the amount of fast charge reduces with testing temperature. Hence, it would be interesting to study the evolution of fast charge with electric ageing.
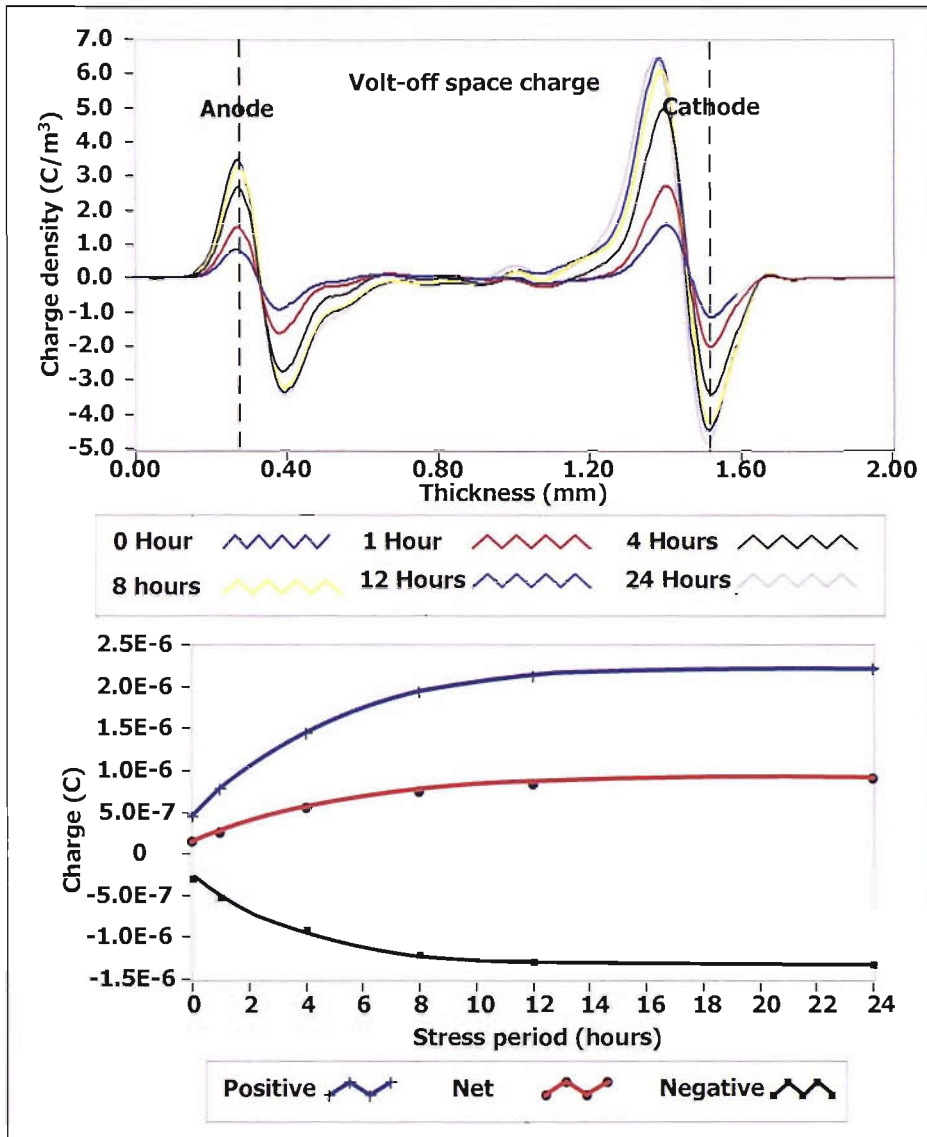
Figure 6.6: Volt-off space charge profiles and charge integrals of sample A.

Figure 6.7 shows the fast charge profiles in sample A, which was computed using equation 6.5, and their integrals over 24 hours of ageing. Unlike the charges in the volt-off space charge profiles which are trapped in the sample, fast charges are charges which disappear almost immediately after the removal of the applied voltage. A quick comparison between the volt-off space charge profiles and the fast charge profiles show clearly that the amount of fast charge is significantly less than that of the volt-off space charge, particularly the negative charge at the anode. This suggests that most of the charges in the sample did not have enough energy to overcome the trap depth.
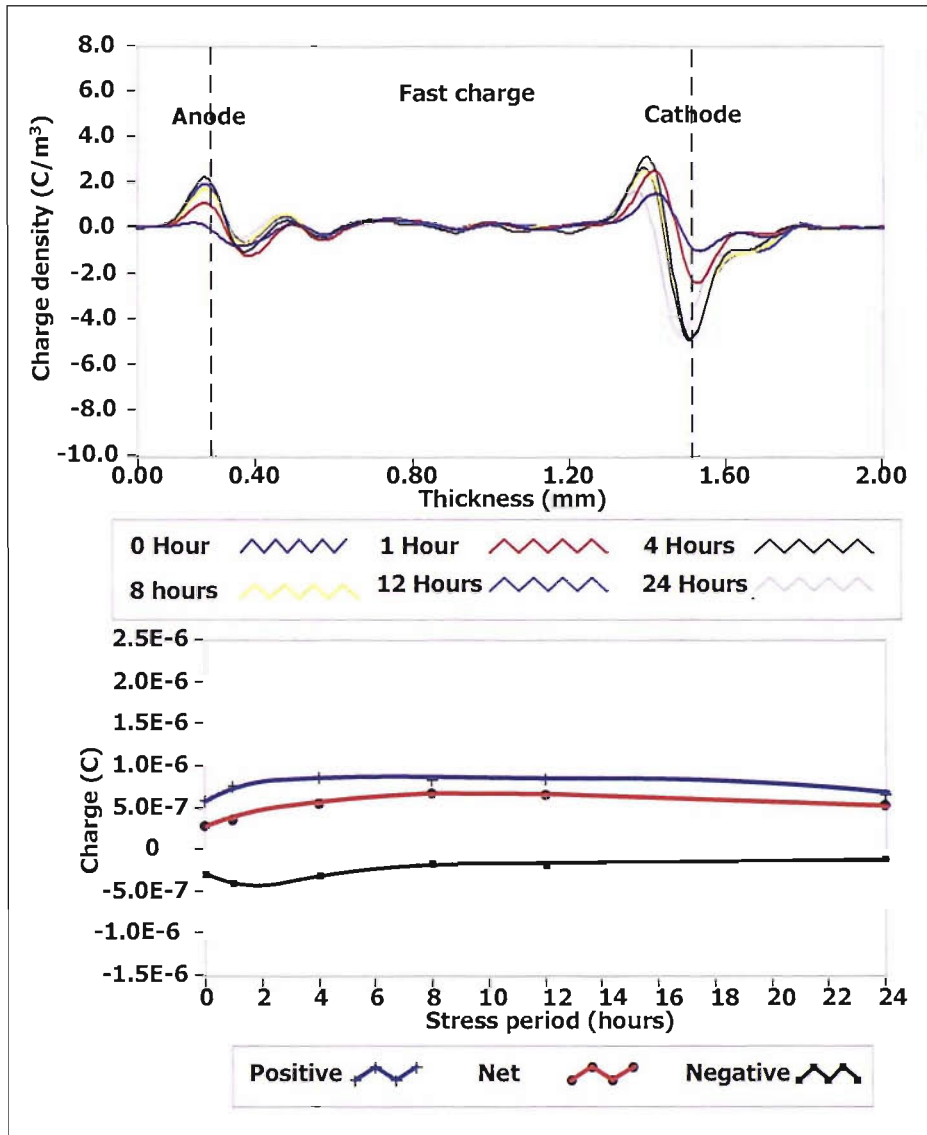
Figure 6.7: Fast charge profiles and charge integrals of sample A.

Comparing the charge integrals of the trapped charge and the fast charge, it can be seen that the amount of space charge trapped (i.e. volt-off space charge) in sample A increased with ageing period, while the amount of fast charge increased during the early stages of the ageing period, but reduces after about 2 hours in the case of negative charge and 4 hours for positive charge.

It has been reported that when LDPE or indeed XLPE is aged under dc [132-134] or ac [96, 135-137] electric stress, space charge trapped in the material decayed at a slower rate when short-circuited. It was also reported that the longer the ageing time, the slower the decay rate. These results suggest formation of deep traps in the

materials due to electrical ageing. Bearing this in mind, dc electrical ageing results in reduction of shallow traps; making deep traps more dominant.

Figure 6.8 illustrates the volt-off space charge profiles of sample B and its integral.
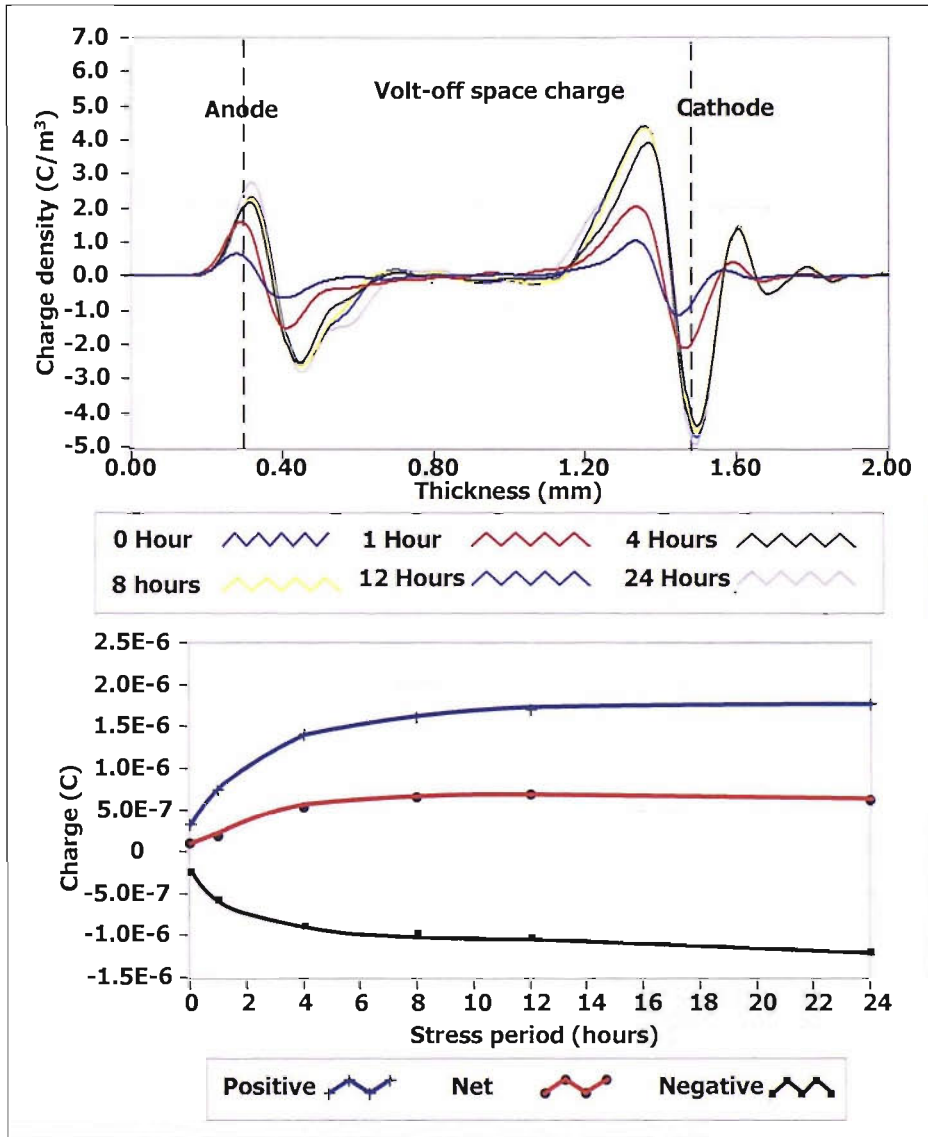
Figure 6.8: Volt-off space charge profiles and charge integrals of sample B.

The general distribution of the charge trapped in the sample B is similar to that of sample A. As in the case of sample A, the amount of trapped charge in sample B also increased with ageing time but to a lesser amount. This is due to the difference in testing temperature which may lead to a number of implications. Firstly, the increase in temperature may result in enhancement of charge injection at the electrodes, which

in turn neutralised the heterocharges. Secondly, higher temperature causes electrical conductivity to increase. As such it will be more difficult for sample B to trap charge as they are moving at a faster speed. Thirdly, as the temperature in sample B is higher than sample A, the charges in the former will have higher energy and, therefore, may possess enough energy to surmount certain shallow traps almost immediately after the removal of the voltage.
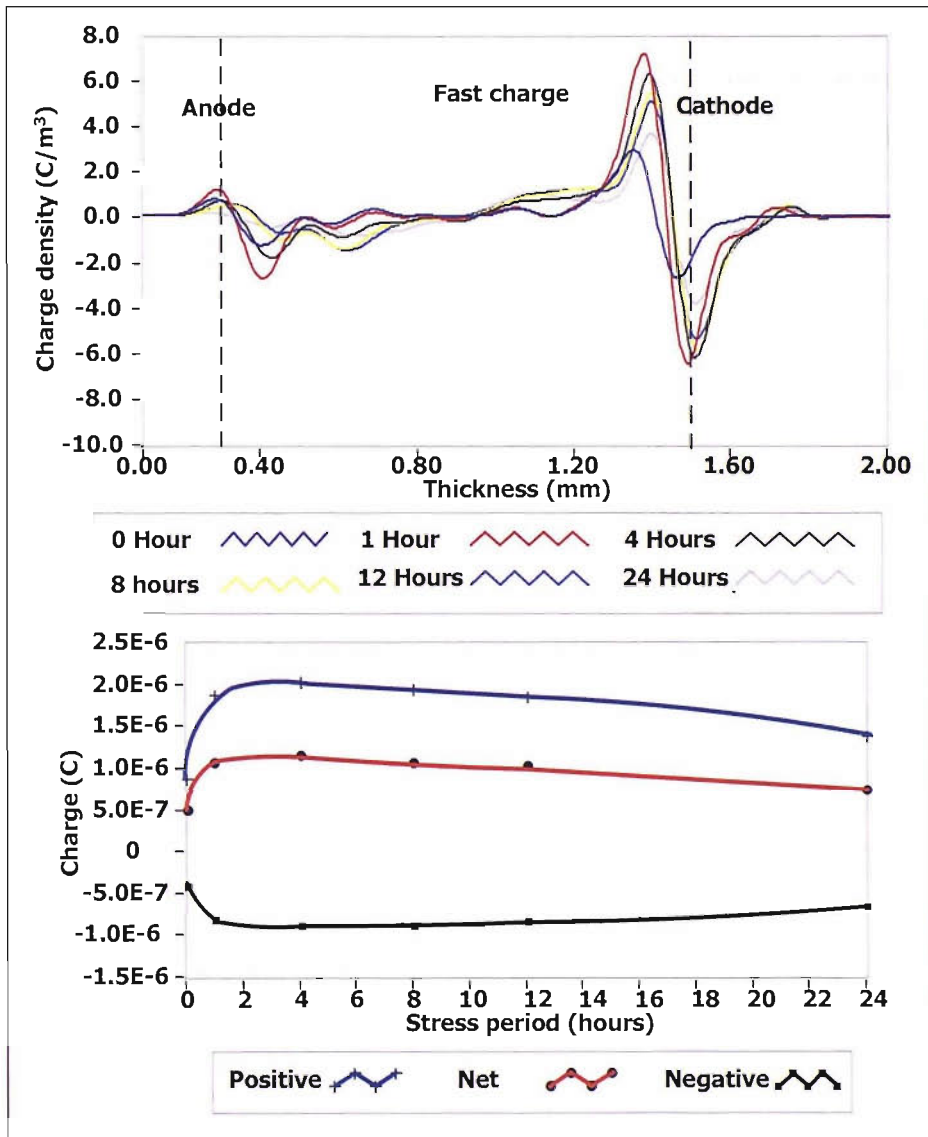
Figure 6.9: Fast charge profiles and charge integrals of sample B.

Figure 6.9, which shows the fast charge profiles in sample B and their integrals, indicates relatively large amount of fast charge when compared with sample A. This

partially supports the earlier argument of more charge having enough energy to surmount the trap depth as a result of higher energy.

It is noted that the rate of fast charge accumulation in sample B increases rapidly during the first 2 hours of the ageing but reduces steadily after 4 hours of ageing. This rapid increase followed by gradual decrease of fast charge, although less pronounced, was also seen in sample A. Therefore, it is believed that the charge dynamics of sample B is basically the same as sample A only accelerated and enhanced by the increase in temperature. It is also interesting to note that, the fast charge profiles were dominated by positive charge and its magnitude is comparable to the positive trapped charge.
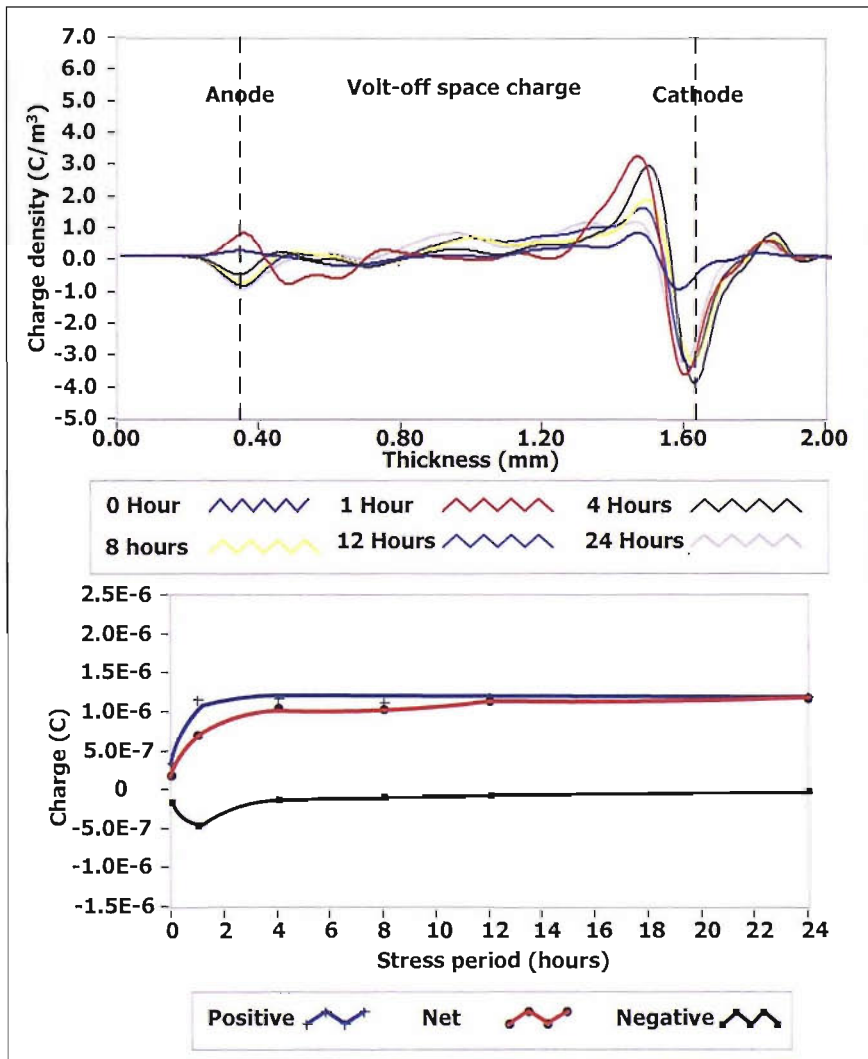
Figure 6.10: Volt-off space charge profiles and charge integrals of sample C.

Figure 6.10 shows the volt-off space charge profiles and its integral of sample C and figure 6.11 shows the corresponding fast charge profiles and integral. From the two figures, it can be seen that sample C has significantly less trapped charge compared to samples A and B. Furthermore, like in the case of samples A and B, the amount of fast charge reduces with ageing times. The reasons for these observations were believed to be the same when explaining the discrepancies between samples A and B. Sample C being tested at the highest temperatures of the 3 samples will, unsurprisingly, have the most extreme of such effects.
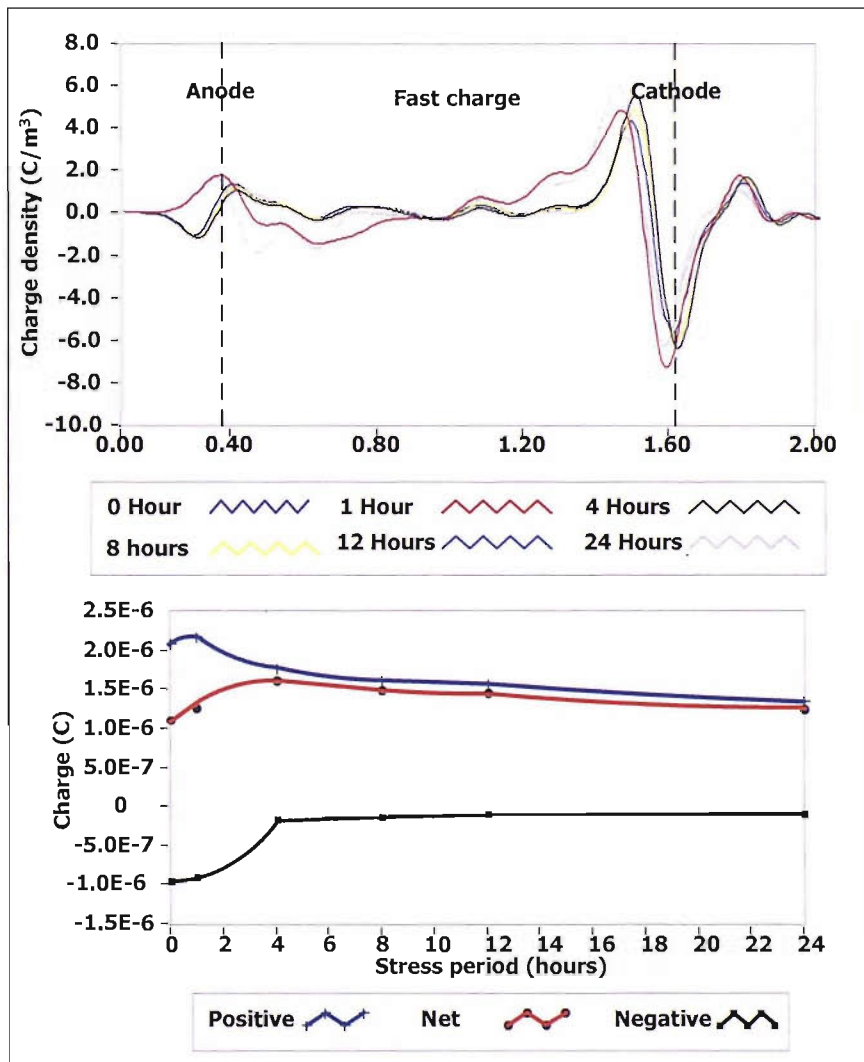
Figure 6.11: Fast charge profiles and charge integrals of sample C.

Closer examination of the volt-off space charge profiles of sample C, indicates a small amount of negative trapped charge accumulated in the vicinity of the anode at 0 hour and it became more pronounced after 1 hour of ageing. However, beyond 1 hour this

negative charge accumulation gradually reduced and eventually was masked by the image charge at the anode after 12 hours of ageing.

Similar effect was seen for the positive trapped charge during the first hour of ageing. Beyond 1 hour, however, the accumulation region of the positive trapped charge became more widely distributed into the bulk of the sample as compared to samples A and B. Considering the above, it is proposed that due to the higher temperature, more positive charge was injected at the anode. Furthermore, the increase in charge mobility and thus conductivity due to higher temperature made easier for the injected positive charge to be transported into the bulk.

Comparing the results of samples A to C, it can be concluded that, for this combination of electrode and insulation materials, positive trapped charge dominates the space charge dynamics under high temperature dc electrical ageing.

6.4.2.2 Degassed samples

As mentioned earlier, degassing is one of the most common treatments used in cable industry to improve the electrical performance of the cable. Hence, it would be useful in not only a theoretical, but also from a practical stand point to study temperature effect on space charge dynamics in degassed XLPE samples.

As the experimental protocols for sample E are exactly the same as for sample I tested in chapter 5, therefore, it is not necessary to re-do the experiment. The volt-off space charge profiles of sample E and its integral can be seen in figure 5.16 and the space charge mechanism has also been explained.

Figure 6.12 shows the fast charge profiles and charge integral of sample E. As seen from the fast charge profiles, only negative fast charge can be seen in the sample. The slight amount of positive charge reflected in the charge integral are not actual charge present but rather oscillating noise due to the measurement circuit and signal processing.
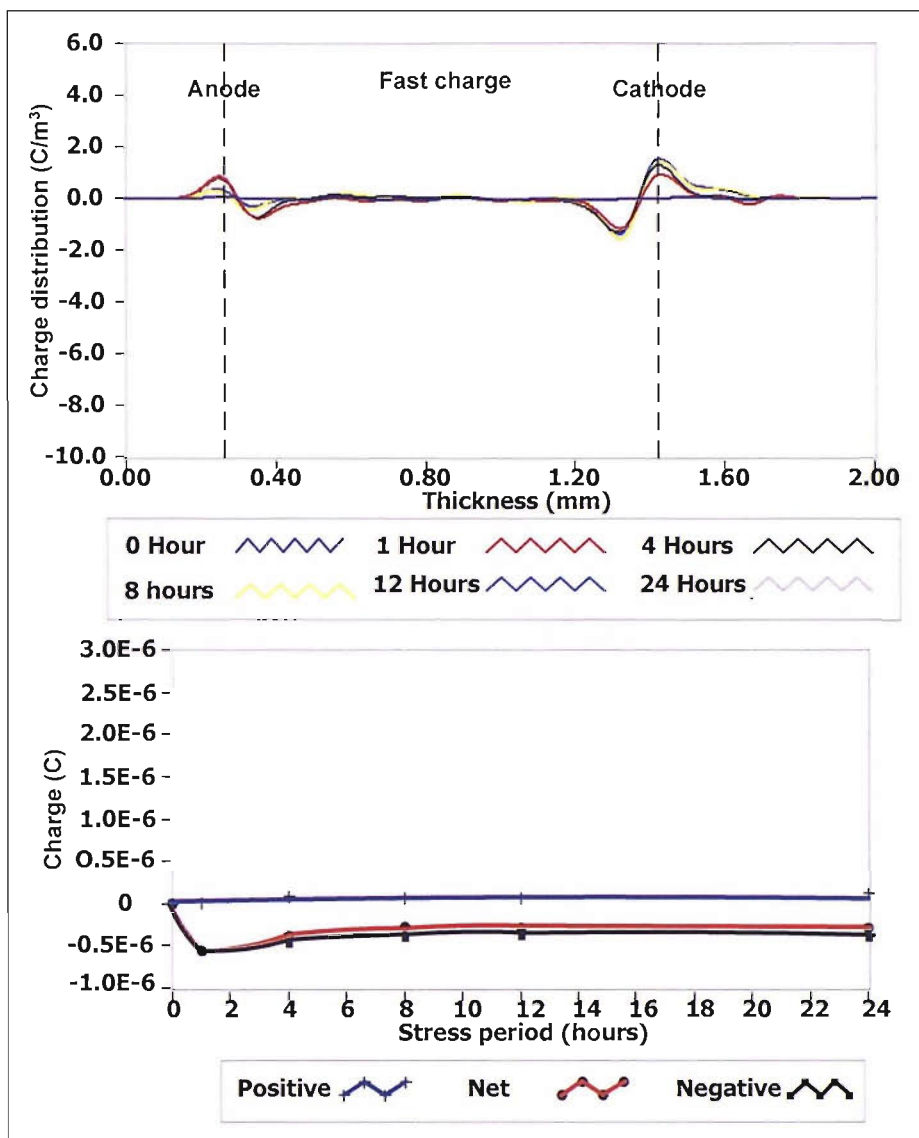
Figure 6.12: Fast charge profiles and charge integrals of sample E.

Evidently, from both the trapped and fast charge integrals, negative charge seems to be more dominant over positive charge. Results from chapter 5 suggest that volatile by-products in this sample have already been largely removed by degassing, therefore, most of the charge, both trapped and fast, in the sample originates from charge injected across the insulation/semicon electrode interfaces. Bearing this in mind and looking at the negative fast charge in the vicinity of the anode, suggests that negative charge is more mobile at 25 °C. Careful observation of the volt-off space charge profile in figure 5.15, which indicates that negative charge is more widely distributed in the bulk as compare to positive charge, further supports the above statement.
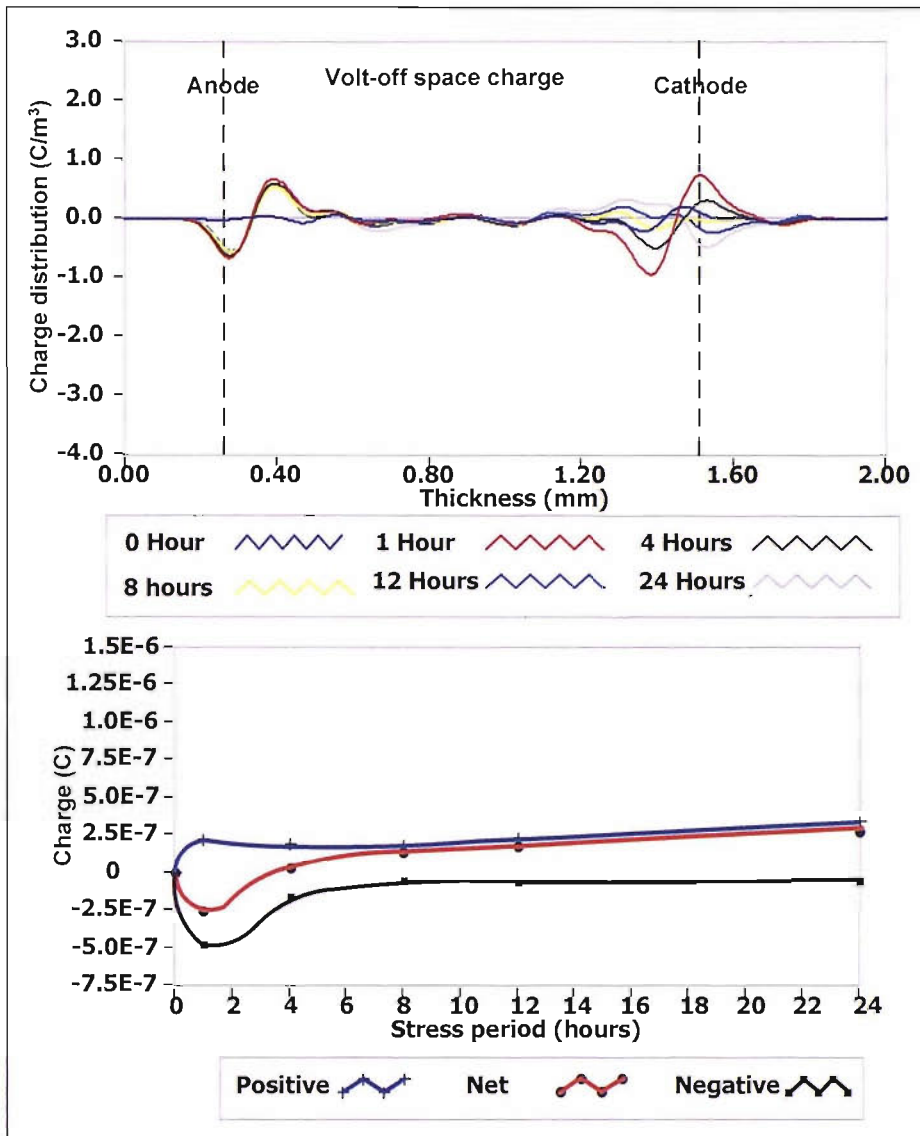
Figure 6.13: Volt-off charge profiles and charge integrals of sample F.

With reference to figure 6.13, which shows the volt-off space charge profiles and charge integral of sample F, a rapid increase in homocharge accumulation adjacent to both electrodes can be observed after 1 hour of ageing. Beyond 1 hour, the negative charge adjacent to the cathode starts to decrease while the positive charge near the anode remained reasonably stable throughout the ageing experiment. It was also noted that all the negative charge in the vicinity of the cathode disappeared after about 4 hours and was replaced by a small amount of positive charge.

The origin of the positive charge may be attributed to the presence of crosslinked by-products that remained in the sample despite strong degassing. Further if these crosslinked by-products can only be dissociated into ionic pairs at temperature higher than 25 °C, it would explain why this positive charge wasn't observed in sample E.

This effect may also be due to an increase in charge injection and charge mobility as a result of increase in temperature, causing more positive charge to be injected, transported and eventually trapped at the cathode.

It should be noted that dissociation of by-products result in not only positive charge but negative charge as well. Also, increase in temperature will not only enhance positive charge injection and transportation but negative charge as well. Evidently, the positive charge at the anode remained rather stable. This is probably because trapped positive charge is more stable therefore more difficult to neutralize and cancel off than negative charge. This agreed with the one of the findings from the results in chapter 5.

Only positive fast charge can be seen in sample F as shown in figure 6.14. No fast charge was present immediately after the step voltage test. This was followed by an increase in positive fast charge in the vicinity of the cathode during the first 8 hours before it reduces slightly. Interestingly enough, this coincides with the time when the trapped negative charge was replaced by positive charge.
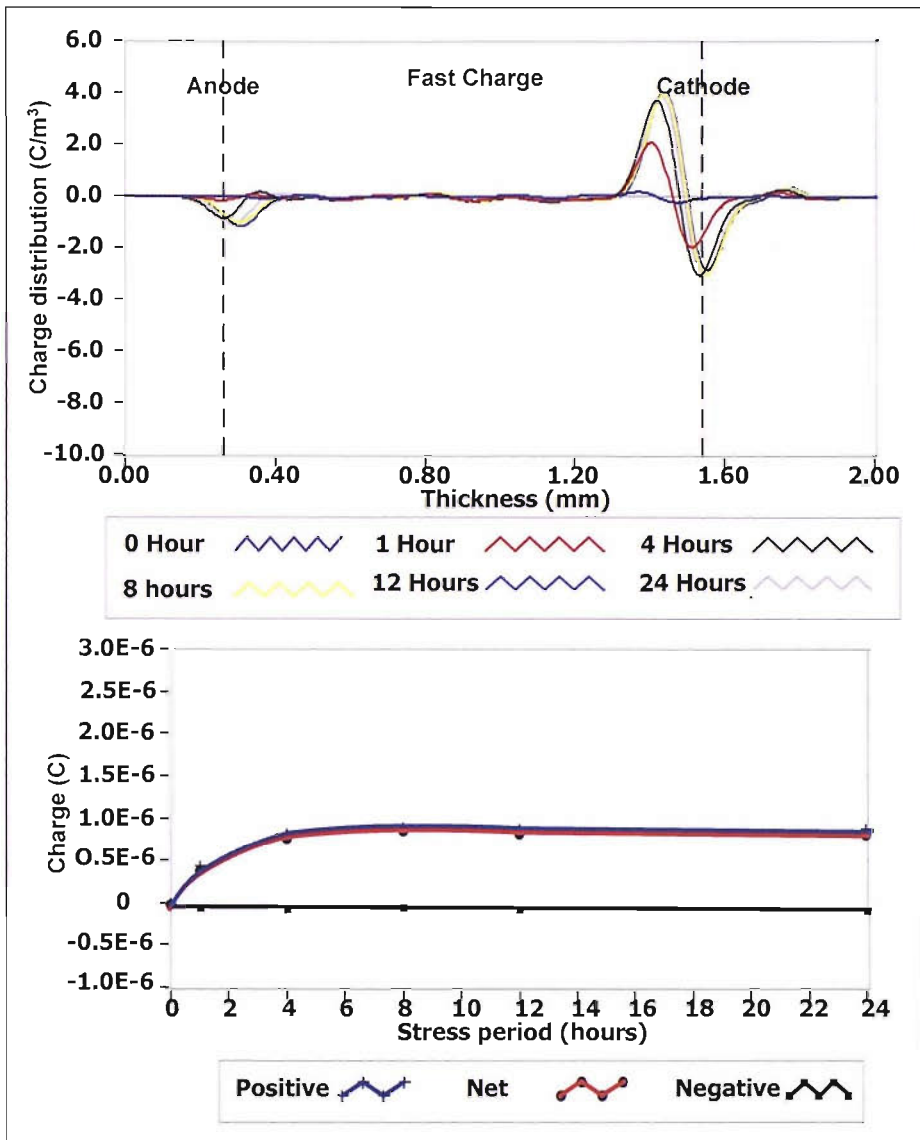
Figure 6.14: Fast charge profiles and charge integrals of sample F.

Boudou et al reported that an enhancement of positive charge de-trapping and negative charge injection occurs at about 45 °C in virgin LDPE [92]. Taking into account that the polarity of the applied voltage was opposite and there are reports which showed that polarity reversal resulted in mirror image space charge distributions [79, 112, 129], therefore, it can be said that there is agreement between the results reported by Boudou et al and those in the present study.
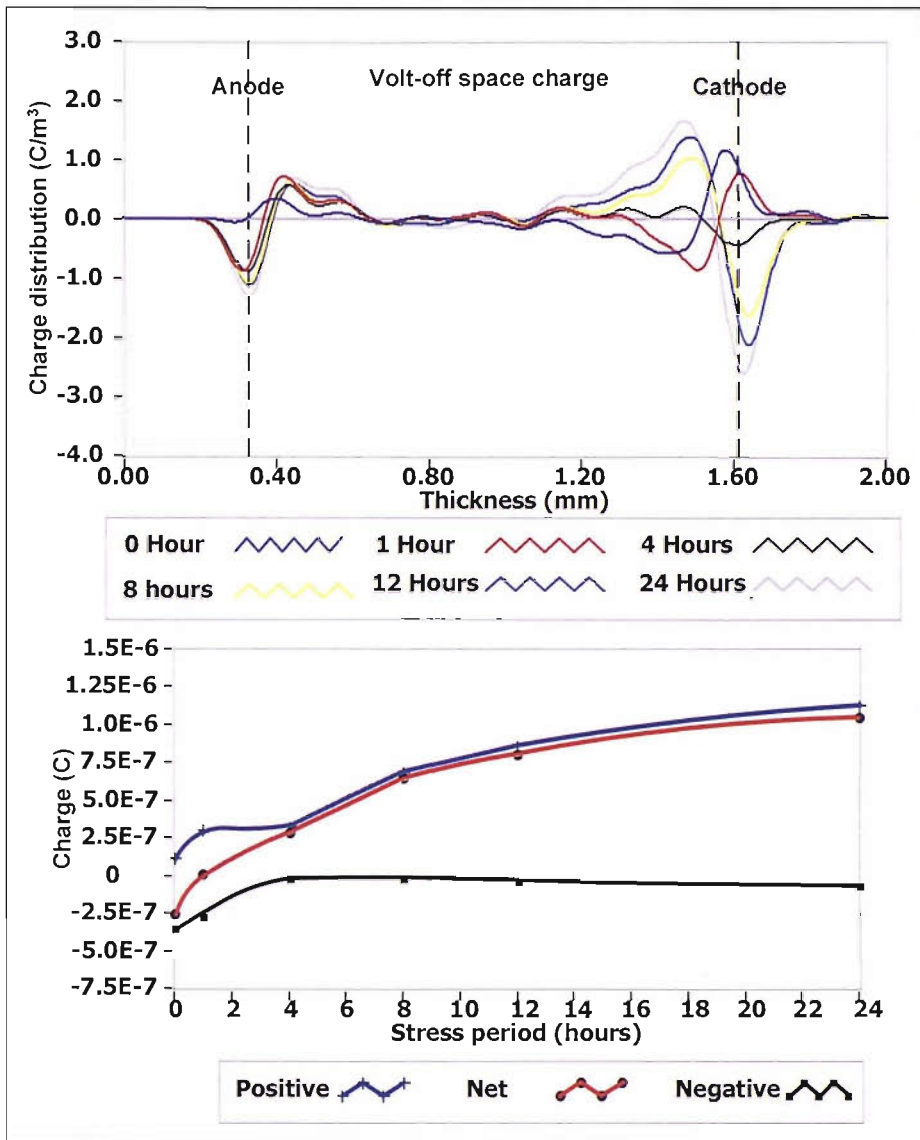
Figure 6.15: Volt-off charge profiles and charge integrals of sample G.

The volt-off space charge profiles of sample G, shown in figure 6.15 indicates homocharges accumulation near both electrodes at 0 hour. This confirmed its results in the step voltage test, which suggested accumulation of positive charge at the anode when the applied voltage exceeds 20 kV. This is probably due to the enhanced injection from the electrode as a result of increase in temperature. These homocharges continued to increase after 1 hour of ageing.

While the positive homocharge trapped near the anode remained reasonably stable throughout the 24 hours of ageing, the negative homocharge which was trapped in the vicinity of the cathode was completely neturalised after 4 hours of ageing. After 8

hours of ageing, substantial amount of positive heterocharge has already been trapped at the cathode and the amount of charge continued to increase with ageing.

The space charge dynamics of the trapped charge in sample G seemed to follow the trend of sample F, the only difference being the effect was more pronounced. This is probably because all the possible causes used to explain space charge formation in sample F can be accelerated and enhanced with higher temperature.

As the fast charge results of sample G are very similar to that of sample F, it will not be shown in this report. The only noticeable difference was at 0 hour there is a small amount of fast positive charge adjacent to the cathode (heterocharge). This is probably due to the increase in the mobility of the fast positive charge under increased temperature.

Sample H was tested at 90 $^{\circ}$C. Under such high temperature, the XLPE material is significantly softened and will in turn affect the acoustic properties of the sample. As the LIPP is a measurement technique based on the propagation of acoustic waves, increase in temperature will most definitely affect the output signal.

With reference to figure 6.16, which shows the volt-off space charge profiles and charge integrals of sample H, there appeared to be a slight amount of charge in the sample at 0 hour, but it is of the same magnitude as the oscillating noise. This relatively poor signal-to-noise ratio is probably caused by the change in acoustic properties of the XLPE sample. Due to this, the observed signal may not be the actual charge but an artifact of the LIPP system.

Similar to samples E to G, homocharges were seen trapped near the electrodes of the sample H after 1 hour of ageing. However, at the 4th hour, relatively large amount of positive charge were seen trapped in the vicinity of the cathode and remained reasonably stable during the 24 hours of ageing.
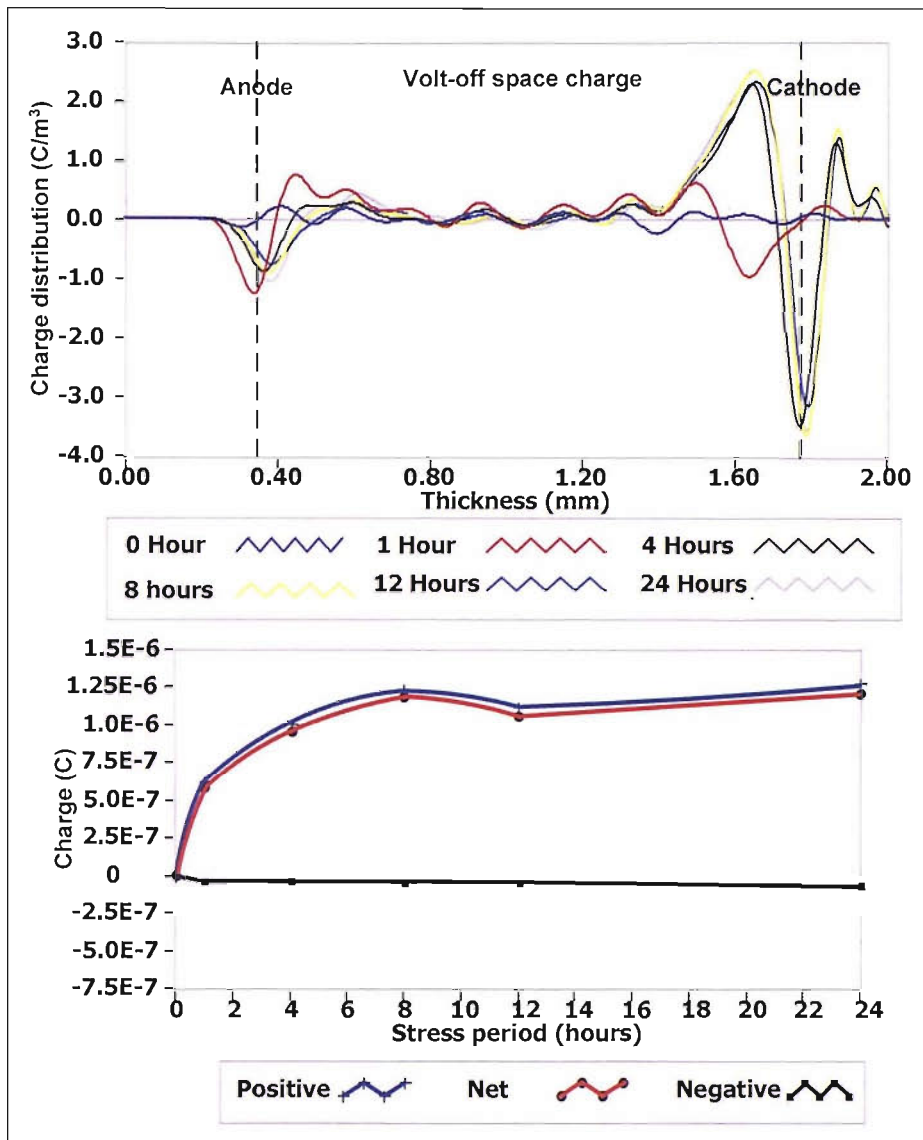
Figure 6.16: Volt-off space charge profiles and charge integrals of sample H.

The effect whereby the positive charge trapped adjacent to the anode remained relatively constant throughout the experiment as in the case samples E to G was not seen in sample H. Figure 6.16 indicates trapped charge accumulated adjacent to the anode of sample H during the 1st hour of ageing has disappeared after 4 hours. The difference observed is probably due to the increase in energy of the positive charge injected. This causes the positive charge to be more difficult to be trapped near the anode. Therefore, they are either transported to the cathode or de-trapped themselves after the removal of the applied voltage.
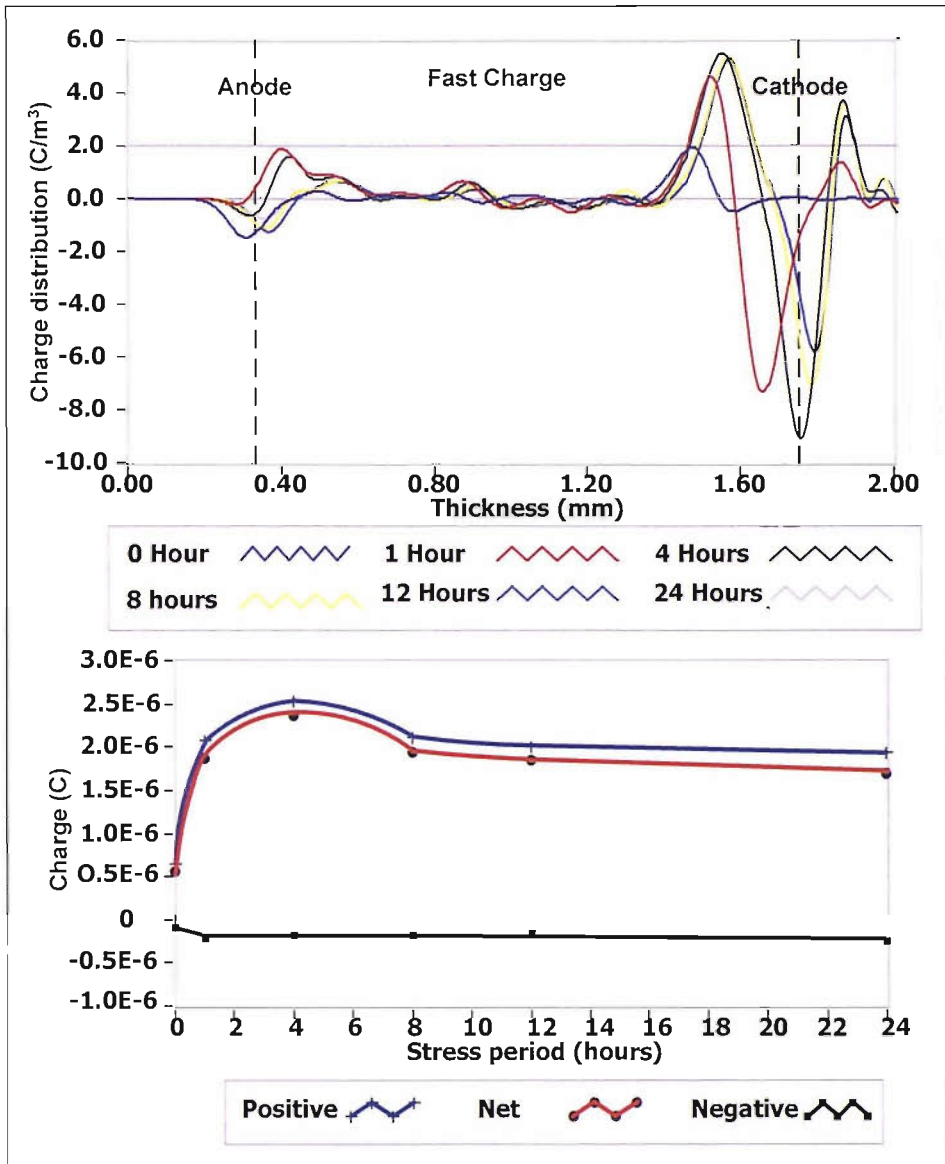
Figure 6.17: Fast charge profiles and charge integrals of sample H.

As mentioned earlier, there is no trapped charge in the sample at 0 hour. Hence, the reason for the drop in interfacial stress seen in the step voltage test must be due to fast charge. A quick look at figure 6.17, which shows the fast charge profiles and integrals, confirmed the presence of positive fast charge at both electrodes. This is probably because of the higher energy and mobility of the charge, making it difficult for charge to be trapped and stayed trapped after the removal of the voltage.

The amount of positive fast charge in the sample rose sharply during the first 4 hours. A slight decrease in the positive fast charge at the cathode can be observed after 8 hours of ageing. On the other hand, the positive fast charge at the anode has almost

completely disappeared by that time. Taking into consideration that the reduction at the cathode end is small as compared to that at the anode and also the increase in charge mobility due to high temperature, it is believed that these reduction of positive fast charge is due to negative charge injected from the cathode and transported across the sample since the reduction at the cathode end is small as compared to that at the anode.

It is worth noting that the fast charge profiles of all the degassed samples tested followed similar trend, in that there is an initial increase in the amount of charge followed by a gradual decrease as ageing progressed. This effect was also seen in all the as-received samples tested. As mentioned before, this is believed to be caused by electrical ageing of the XLPE material which may have converted some shallow traps into deep traps.

A few general remarks can be made when comparing the space charge results of as-received and degassed samples. Firstly, in the case of as-received samples, the amount of trapped charge reduces with increase in testing temperatures but not in the case of degassed samples. In fact, in the case of degassed sample, the general shape of the space charge distribution converted significantly at high testing temperature.

Secondly, space charge distributions of both as-received and degassed sample of at high temperature (70 °C and above) took the same general form, although the quantity is smaller in the case of the latter. This implied that under high temperature, degassing treatment does not significantly alter the general distribution of space charge.

Lastly, it can be seen from the results of the above study that positive charge propagation enhances as testing temperature increases for both as-received and degassed samples. This should be taken seriously by researchers and cable manufacturers as studies have shown a direct relationship between positive charge propagation and the intrinsic breakdown of the insulating materials [107, 130].

6.5   Conclusion

In this chapter, the space charge dynamics in XLPE plaques at different temperatures during 24 hours of dc electric ageing have been reported. The main conclusions are:

- The dc threshold stresses of the as-received and degassed samples are greatly affected by testing temperatures.

- Although, the step voltage test is a nice and convenient way to determine the threshold stress of a sample, it is necessary to verify the results with the space charge profiles and electric field distribution.

- The testing temperature has numerous effect on space charge dynamics such as enhancement of ionic dissociation of polar crosslinked by-products, enhancement of charge injection from the electrodes and increase energy of the charge which in turn enhances charge mobility and conductivity.

- In the case of as-received samples, it is believed that the ionization of by-products dominates the space charge characteristics at low temperatures. However, testing temperature may enhance the injection process at the electrodes and the negative heterocharge at the anode initially accumulated inside the bulk will be neutralised.

- The amount of trapped charge in the as-received samples decreases while the fast charge increases with testing temperature. This is believed to be due to the increase in energy of the charge, enabling it to be de-trapped almost immediately after the removal of the applied voltage.

- The nature of the space charge in the degassed samples changed rather significantly as compared to the as-received samples. It is believed that the combination of enhance high temperature ionisation of crosslinked by-produtcs, charge injection, transportation and formation of deep traps caused the negative homocharge accumulated at low temperature to be neutralised and eventually replaced by positive heterocharge at the cathode.

- For both as-received and degassed samples, the space charge distribution is dominated by positive charge at high testing temperature.

- At temperature of 70 °C and above, the space charge distribution takes the same form, albeit lesser in quantity in degassed sample, regardless of whether the sample is degassed or not.

- The fast charge of all samples seemed to follow the same trend, in that, a rapid increase in charge followed by stabilization or in most cases, reduction of fast charge as ageing progressed. This is believed to be due to conversion of shallow traps into deeper traps as a result of ageing.

- Positive charge propagation enhances as testing temperature increases for both as-received and degassed samples. This can be a major cause of concern as such behaviour is usually related to insulation breakdown.

7 Space charge in planar samples using the LIPP and the PEA: Space charge and charge trapping characteristics of crosslinked polyethylene subjected to ac electric stresses

7.1 Introduction

Over the past two decades, space charges within dielectrics under dc electric stress (herein known as dc space charge) have received much interest and numerous literatures regarding their evolution and activities in different types of materials with different chemical additives were published [27-29, 31, 38, 40, 44, 66, 70-73, 76-85, 89, 92, 93, 104, 118-122, 124, 138-146].

On the other hand, investigation in space charges under 50 Hz ac condition remains a relatively unexplored field. Indeed, it is only in the last few years or so that results, albeit limited, of space charge in polymeric insulation subjected to ac stress (herein known as ac space charge) were reported [35, 69, 94-99, 101-103, 109, 135, 147].

Various measurement techniques, former only used for dc space charge, such as the thermal step method [94, 102, 103], the pulsed electroacoustic (PEA) method [35, 96, 101, 109, 135, 147] and the laser induced pressure pulse (LIPP) method [69, 95, 97-99] were employed for ac space charge measurements.

Earlier results using the PEA technique [35] revealed that the critical frequency on which space charge accumulates is < 0.02 Hz. However, findings in [102, 103, 135] have shown clear evidence of space charge accumulation in polymeric insulation when stressed at power frequency (50 Hz). It should be pointed out that the poling times were considerable longer in the literature whereby space charge accumulations were observed. It was also suggested in [135] that different electrode/insulation interfaces could be another factor contributing to the inconsistency in literatures. Indeed, it was demonstrated that ac space charge of very different nature (in fact completely opposite) were observed with different electrode/insulation interface configurations.

This chapter reports on the result of space charge evolution in crosslinked polyethylene (XLPE) planar samples. Initially, space charge in both degassed and as-received samples of approximately 1 mm thick subjected to 50 Hz 30 kV_{pk}/mm ac electric stress measured using the LIPP technique were presented.

Next, space charge distributions in samples of approximately 220 μm thick were examined using the PEA technique. There are two phases to the PEA experiment. First, the samples, both as-received and degassed, were subjected to dc 30 kV_{dc}/mm and ac (sinusoidal) electric stress level of 30 kV_{pk}/mm at frequencies of 1 Hz, 10 Hz and 50 Hz ac for 24 hours. In addition, ac space in samples charge subjected to 30 kV_{rms}/mm and 60 kV_{pk}/mm electric stresses at 50 Hz were also investigated.

Space charge mechanism in dielectric under ac electric stress is often difficult to understand as numerous factors such as the varying amplitude of sinusoidal ac voltage, voltage reversal, charging trapping/recombination, charge injection/extraction, material degradation, etc, need to be considered. Hence, the second phase of the experiment involves studying the dc space charge evolution in samples that were pre-aged under ac stress. However, for reasons to be explained later, the second phase of the experiment will only be conducted on the degassed samples.

7.2 Sample details

The samples used were made from the same material and manufacturing procedure as described in sections 5.2 and 6.2. The samples are approximately 1.6 mm thick overall and 1.2 mm thick in insulating bulk. All degassing was done in a vacuum at 90 °C for 48 hours and subsequently left to cool at room temperature for 15 mins. Details of the samples are shown in table 7.1.

7.3 Experimental protocols

7.3.1 Ac space charge measurements using the LIPP technique

Both degassed and as-received samples, approximately 1 mm thick, were stressed at 30 kV_{pk}/mm for 24 hours. Point-on-wave space charge measurements were taken at regular intervals during this period. After 24 hours of ageing, the volt-off space charge profiles were measured and monitored for another 2 hours. As high voltage is required, the samples were pressurized in SF_6 gas to reduce electric discharge. All tests were conducted at room temperature. Details of the experiment is shown in table 7.1

Sample	Treatment	Stress level	Frequency
S1	Degassed	30 kV_{pk}/mm	50 Hz Sinusoidal
S2	As-received	30 kV_{pk}/mm	50 Hz Sinusoidal

Table 7.1: Experimental protocols for space charge measurement using the LIPP technique (first phase)

7.3.2 Ac space charge measurements using the PEA technique

This experiment is sub-divided into 2 phases. In the first phase of the experiment, all samples were electrically aged for 24 hours. Space charge distributions were measured at every hour interval during the ageing period with voltage applied. Details of the experimental protocols can be seen in table 7.2.

Investigations on dc space charge dynamics were done mainly as a reference to assist the understanding of ac space charge dynamics since its behaviour is better understood.

The point-on-wave approach is not necessary for dc space charge since the applied voltage does not vary with time. For the case of ac space charge, however, 16 equally spaced measurements on a complete sinusoidal wave were taken. After 24 hours of

ageing, the short-circuit space charge distributions were measured and monitored for 2 hours.

Sample	Treatment	Stress level	Frequency
A	Degassed	30 kV$_{dc}$/mm	dc
B	Degassed	30 kV$_{pk}$/mm	1 Hz Sinusoidal
C	Degassed	30 kV$_{pk}$/mm	10 Hz Sinusoidal
D	Degassed	30 kV$_{pk}$/mm	50 Hz Sinusoidal
E	Degassed	30 kV$_{rms}$/mm	50 Hz Sinusoidal
F	Degassed	60 kV$_{pk}$/mm	50 Hz Sinusoidal
G	As-received	30 kV$_{dc}$/mm	dc
H	As-received	30 kV$_{pk}$/mm	1 Hz Sinusoidal
I	As-received	30 kV$_{pk}$/mm	10 Hz Sinusoidal
J	As-received	30 kV$_{pk}$/mm	50 Hz Sinusoidal
K	As-received	30 kV$_{rms}$/mm	50 Hz Sinusoidal
L	As-received	60 kV$_{pk}$/mm	50 Hz Sinusoidal

Table 7.2: Experimental protocols for space charge measurement using the PEA technique (first phase)

The second phase of the experiment was carried out about 1 month after completion of the first. Samples B to F that were aged under ac electric stress during the first phase of the experiment were stored at room temperature during the 1 month, allowing any charge trapped to decay.

After the storage period, a step voltage test was conducted to investigate the stress at which space charge initiates. In this experiment, voltage was increased from 0 kV, at a voltage step of 1 kV every 30 seconds interval, until a stress of level of 30 kV$_{dc}$/mm was reached. Space charge measurements were taken at every incremental voltage step. The final voltage, which depends on the sample thickness, was between the range of 6 to 7 kV. The front and rear peaks of the measured outputs, which are proportional to the stresses at the electrodes, were then plotted against the applied voltage.

Immediately after the step voltage test, the samples were then aged under 30 kV_{dc}/mm electric stress for 24 hours at ambient temperature with, once again, space charge measurement taken at regular intervals. Just as in the first phase of the experiment, the short-circuit space charge distributions in the samples after ageing was monitored for 5 hours. For the sake of brevity the samples tested in the second phase of the experiment will be labelled with 'dc_'; for example dc_sample B, dc_sample C and so on.

7.4 Results and discussion

Results from chapters 5 and 6 indicate that as-received samples have more complicating space charge dynamics due to the presence of crosslinked by-products. As space charge under ac electric stress is still a relatively unexplored field, it would be logical to examine the results of degassed samples first.

7.4.1 Ac space charge measurements using the LIPP technique

Figure 7.1, which shows the point-on-wave measurements of S1 at 0 hour, clearly demonstrates the feasibility of the technique. It can be seen that, as the phase angle of the ac voltage increases from 22.5° to 90° and from 202.5° to 270.0°, the electric stress at the interface, reflected by the amplitude of the two electrode peaks, also increases.
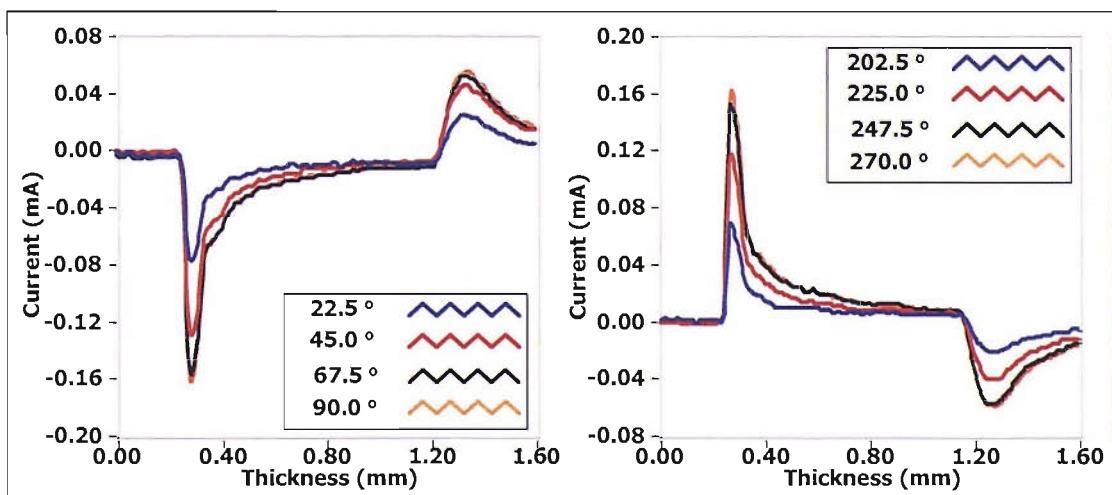
Figure 7.1: Charge profiles of sample S1.

However, as mentioned in chapter 3, the pressure pulse generated by the LIPP system has limited spatial resolution due to the introduction of the target cooling liquid; it would be difficult to see any space charge if the amount is too small which is the case for ac space charge since its magnitude is considerably smaller than dc space charge [101]. As such, figure 7.1 can only serve to illustrate the feasibility of the point-on-wave approach. Since the space charge profiles of sample S2 are similar to that of sample S1, they will not be shown in this report.

Nevertheless, there are 2 ways to go around the problem of spatial resolution. The first way is to use the deconvolution algorithm to recover the ideal space charge profile. The other way is to compute the accumulated charge by using equations 6.2 6.3 and 6.4 as discussed in section 6.4.1.2.

However, as considerable amount of data generated during ac space charge measurements, it will be extremely laborious to use either method to analyse the space charge results. Furthermore, due to the large amount of data generated in ac space charge, it is often difficult to digest all the information. Ho et al has proposed and successfully implemented a simple method for analysing ac space charge termed the 'X-plot' [69, 98].

Details on the concept of 'X-plot' can be found in [69, 98]. Briefly, the 'X-plot' asserts that presence of space charge in a sample will in turn affect the interfacial stresses. Hence, by plotting the interfacial stresses against the point-on-wave voltages or electric stress, one will be able to perceive space charge accumulation, if any.

The 'X-plots' of samples S1 during the 0 and 24 hour of ageing can be seen in figure 7.2.
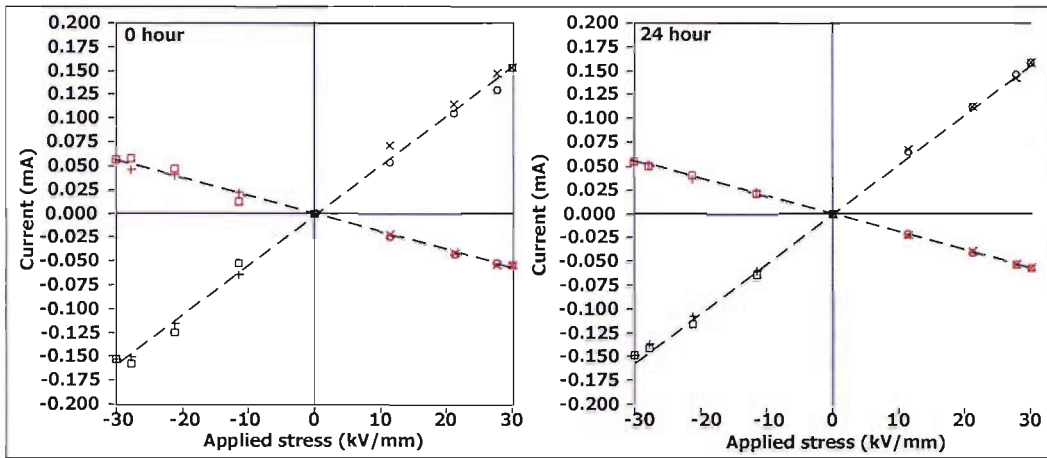
Figure 7.2: 'X-plot' of sample S1

With reference to figure 7.2, it can be seen that entrance and exit peak currents of sample S1 has a linear relationship with the applied point-on-wave electric stress as indicated by the dotted lines. This suggests that no significant space charge has been developed in the sample since presence of space charge will generally cause the entrance and/or exit peak currents and hence the interfacial stresses to change.

Figure 7.3 shows the volt-off space charge profiles of sample S1 before electrical ageing, after 24 hours of ac ageing (at 0 hour decay) and the 2 hours after the applied ac stress has been removed (after 2 hours decay).
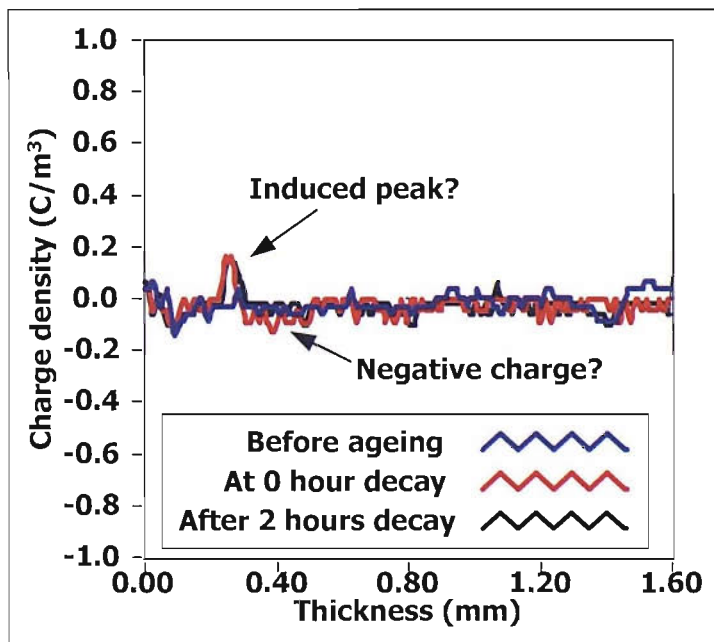
Figure 7.3: Volt-off space charge profiles of sample S1 after 24 hours ageing

From figure 7.3, a small positive peak can be observed in the volt-off space charge profile at 0 hour decay (red line). This small peak seems to be the induced charge caused by the presence of negative charge accumulation in the bulk as indicated by the arrow. However, the result needs to be treated with caution as these indications are extremely subtle, almost of the same order as the oscillation noise. Nonetheless, as will be seen later, the results for samples under ac stress measured using the PEA method confirms that this negative charge is real and not an artefact of the measuring system.

It should be pointed out that this amount of negative charge may be too little to have any significant effect on the interfacial stress. This explains why the 'X-plot' at 0 hour and at 24 hours of ageing look almost identical. An important point to note is while the 'X-plot' is a simple and convenient method for ac space charge analysis, it is not suitable if the amount of charge accumulated is small.

The 'X-plot' and the volt-off space charge profiles of sample S2 are shown in figures 7.4 and 7.5 respectively.
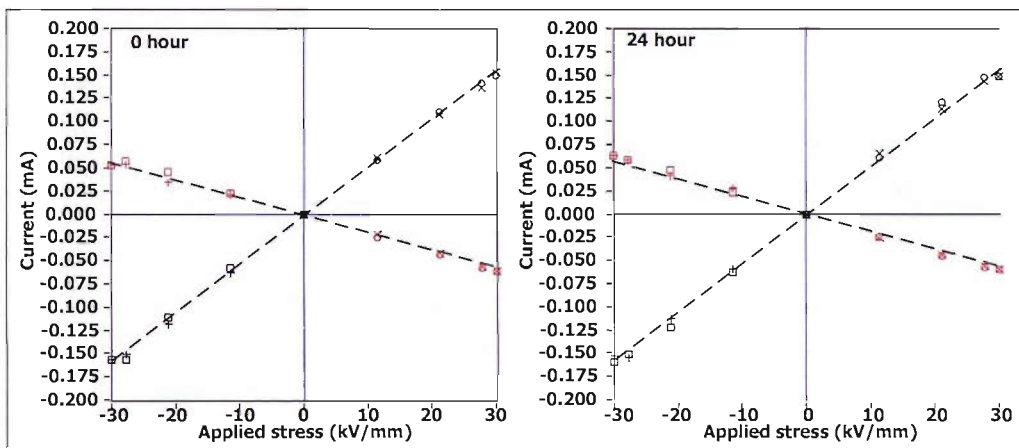
Figure 7.4: 'X-plot' of sample S2
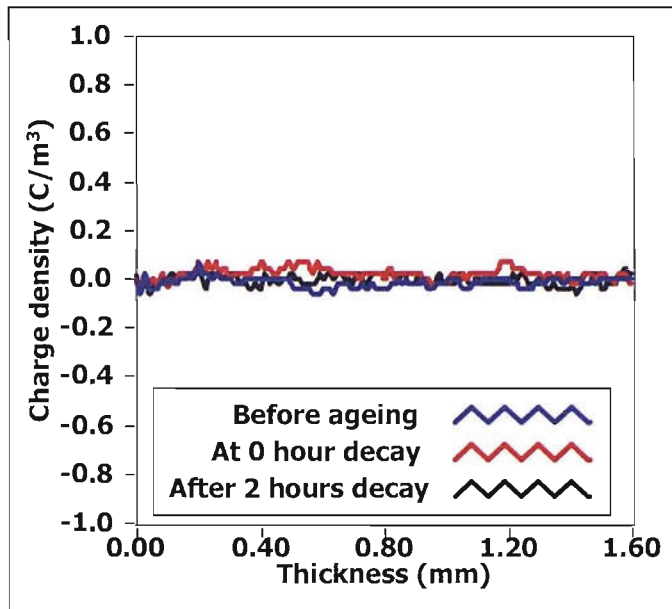
Figure 7.5: Volt-off space charge profiles of sample S2 after 24 hours ageing

Similar to sample S1, the 'X-plot' of sample S2 did not suggest presence of space charge as the relationship between the entrance and exit peak currents and the applied stress is linear as seen from figure 7.4. This is in agreement with the volt-off space charge profiles of sample S2 as shown in figure 7.5. Unlike sample S1, there is neither induced peak nor accumulation of space charge in the bulk, or they are masked off by the oscillation noise inherent in the measurment system.

One possible reason as to why space charge can be seen in sample S1 but not S2 is because of the presence of crosslinked by-products. As seen in the earlier experiment, crosslinked by-products such as acetophenone increases the electrical conductivity. Therefore, it will be more difficult for sample S2, which has a higher conductivity to trap charge than sample S1.

7.4.2   Ac space charge measurements using the PEA technique

As a reference, the space charge profiles of sample A stressed at a dc electric field of 30 kV_{dc}/mm are shown in figure 7.6.
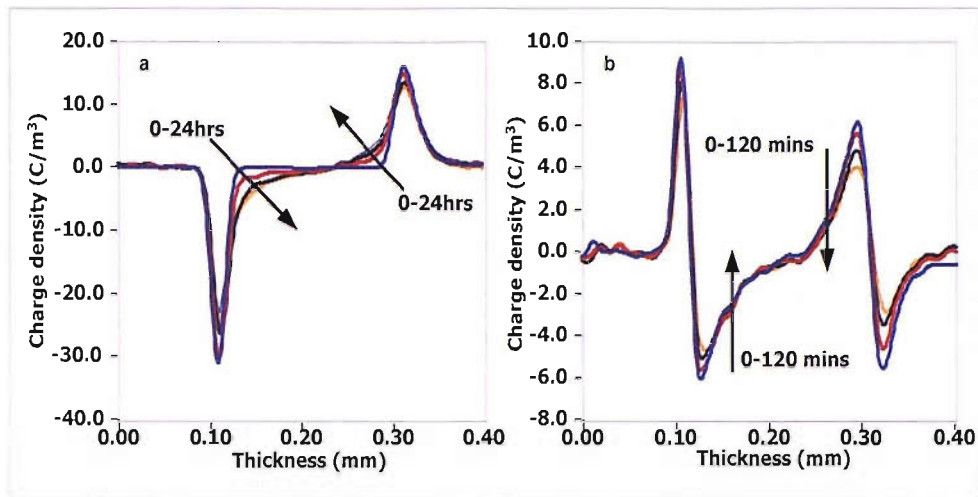
Figure 7.6: Charge profiles of sample A : (a) volt-on (b) volt-off

With reference to figure 7.6(a), which shows the volt-on charge profile during 24 hours ageing, homocharges, or charges of the same polarity as the electrodes, can be seen in the vicinity of both electrodes after just 1 hour of the experiment. The amount of homocharges accumulation increased with ageing duration. This accumulation of homocharges caused the interfacial stresses to reduce, as evident by the decrease in amplitude of the induced charge on the anode and cathode.

The accumulation of homocharges in the bulk of sample A was also reflected in the volt-off space charge profiles as seen in figure 7.6(b). Significant decease in space charge was observed after the applied voltage has been removed for 2 hours. It was also observed that there is more negative charge than positive charge accumulated in the sample.

Figure 7.7 shows the space charge profiles of sample B at various phases of the ac waveform.
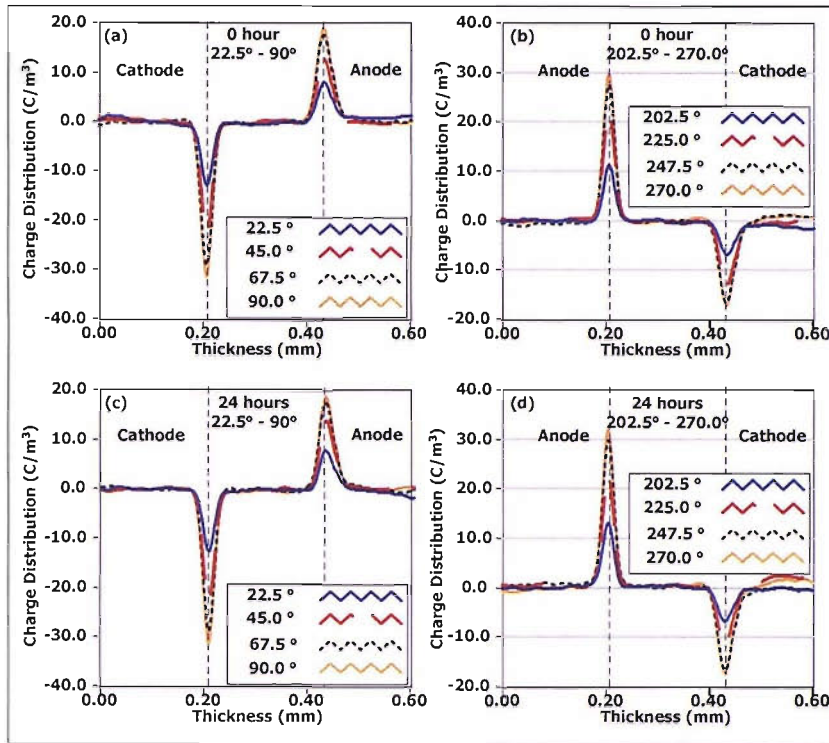
Figure 7.7: Charge profiles of sample B.

Figure 7.7 demonstrates that the feasibility of the point-on-wave technique of the PEA system. Comparing the space charge profiles at 0 hour with that after 24 hours suggests negligible charge accumulation. However, careful examination of the anodes of figure 7.7(b) and 7.7(d) seems to indicate a slight increase in amplitude after 24 hours of ageing.

As mentioned before, space charge can affect the stress at the interface. As opposed to sample A, increase of the stress at the anode may be caused by negative charge accumulation. Although, almost no charge accumulation can be seen in figure 5(d), however, this may be due to the induced interfacial peaks masking off the substantially smaller charge accumulation.

Two methods have been proposed by Montanari et al [101] to observe space charge of such small magnitude. The first method was to compute the charge accumulated in the sample using equation 6.2,

The space charge profile of $\rho_{no-charge}$ used in equation 6.2, has to be obtained before the aging. First the space charge profile of the sample at a stress level that is high enough to yield good signal-to-noise ratio but small enough to avoid space charge

built up in the sample was measured. The electric stress level used for this purpose is < 10 kV/mm as it has been reported in chapters 5 and 6 that, under room temperature, threshold stress for space charge accumulation in this material is at least 10 kV/mm. This space charge profile is also used for calibration purpose and will hence be known as $\rho_{calibrate}$.

Hence $\rho_{no\text{-}charge}$ can be calculated using

$$\rho_{no\text{-}charge} = \frac{E_{applied}}{E_{cal}} \times \rho_{calibrate} \tag{7.1}$$

where $E_{applied}$ and E_{cal} are the applied stress and calibration stress respectively.

Figure 7.8 shows the space charge profiles of sample B at $270°$ after applying the above data algorithm.
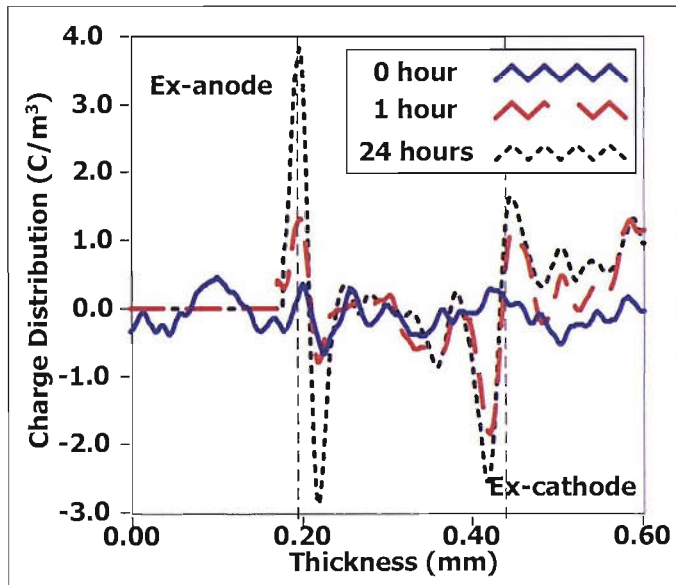
Figure 7.8: Charge profiles of sample B after the removal of the Laplacian contribution to induced interfacial peaks.

As seen in figure 7.8, the charge distribution is dominated by negative charge, also the amount of accumulated in the sample increases with ageing duration. These results are consistent with those reported in [147].

The accumulation of negative charge at the anode led to the increase in interfacial stress at the anode observed in figure 7.7. On the other hand, the negative charge accumulated should cause the interfacial stress at the cathode to reduce. This effect, however, is extremely subtle as the sensitivity of the system at the cathode end is substantially lower than the anode with the latter being closed to the piezoelectric transducer.

The second method proposed was to measure the space charge profile when the Laplacian field is zero which is at the natural zero of the ac waveform, i.e. phases 0° and 180°.

Figure 7.9 shows the space charge profiles of sample B at 180°.
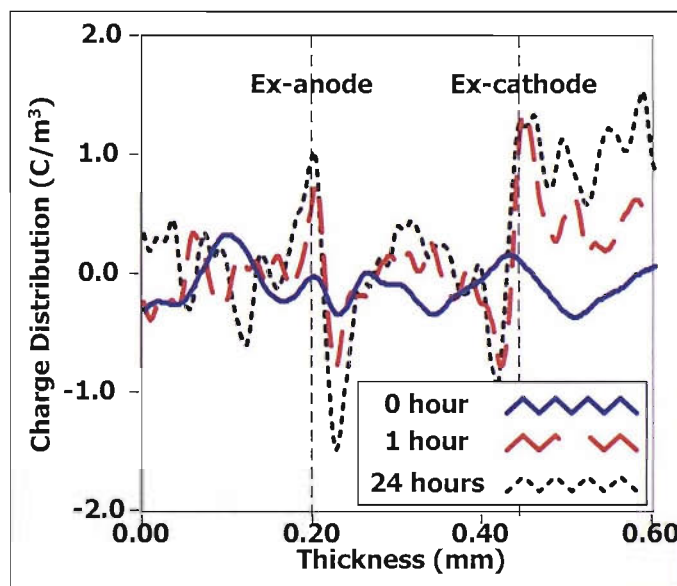
Figure 7.9: Charge profiles of sample B at phase 0°

The space charge profiles taken at the natural zero (only phase 0° is shown here for brevity) of the ac waveform are similar to that seen in figure 7.8, only smaller in magnitude. This may be attributed to very fast charge accumulated in the sample which disappeared as soon as the electric stress across the sample falls to zero.

However, both methods are very dependent on the precision of the point-on-wave technique as such, any drift in the control system may lead to erroneous results. This

is especially true at high frequency and/or voltage where even a phase shift of 1° can result in considerable difference in voltage level.

The point-on-wave space charge profiles of samples C to F are very similar to that of sample B, with the induced peaks masking the presences of space charge accumulation, if any at all. This and bearing problems associated with the above methods and also for simplicity, only charges that were trapped reasonably deep will be presented.

This was done by removing the applied stress after 24 hours of electrical ageing before measuring the volt-off space charge profile. The time span between the removal of voltage and the measurement of the first space charge measurement is approximately 5 seconds. However, for simplicity, this measurement is referred here as 0 hour measurement.

The volt-off space charge profile of sample B is shown in figure 7.10.
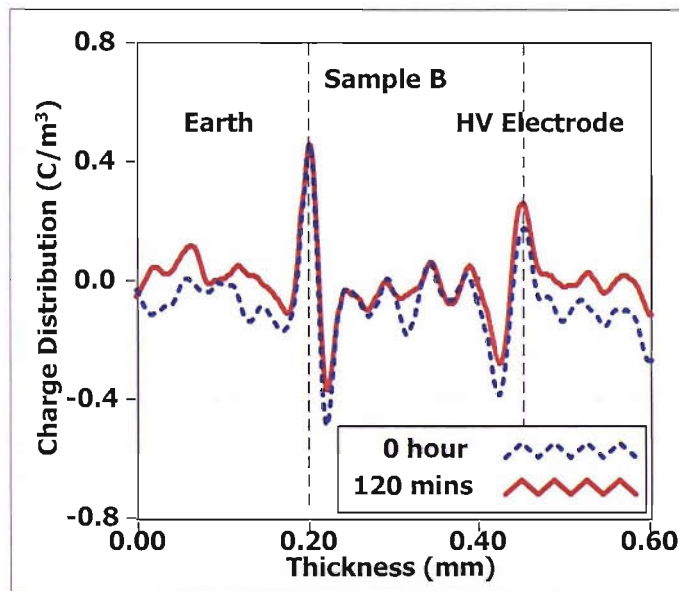
Figure 7.10: Volt-off charge profiles of sample B.

Comparing figure 7.10 with figures 7.8 and 7.9, it can be seen that while smaller in magnitude, the distribution of space charge is generally the same- dominated by negative charge accumulation. This reduction in magnitude is probably due to fast charge being detrapped during the 5 seconds time span needed between the removal

of voltage and measurement of space charge. Short-circuiting the sample for 2 hours resulted in appreciable amount of charge decay but less than what was observed in sample A.

Figure 7.11 shows the volt-off space charge profiles of samples C to F after 24 hours ac ageing.

If the frequency of the ac voltage is low, there is more time for charge to be injected, transported and trapped in the bulk before the polarity of the voltage reverses. Therefore, one would expect the amount of charge trapped in a sample to reduce when the frequency increases. Indeed, it was reported that the amount of charge accumulated in LDPE and XLPE reduces as the frequency of the applied ac voltage increases [35, 147].
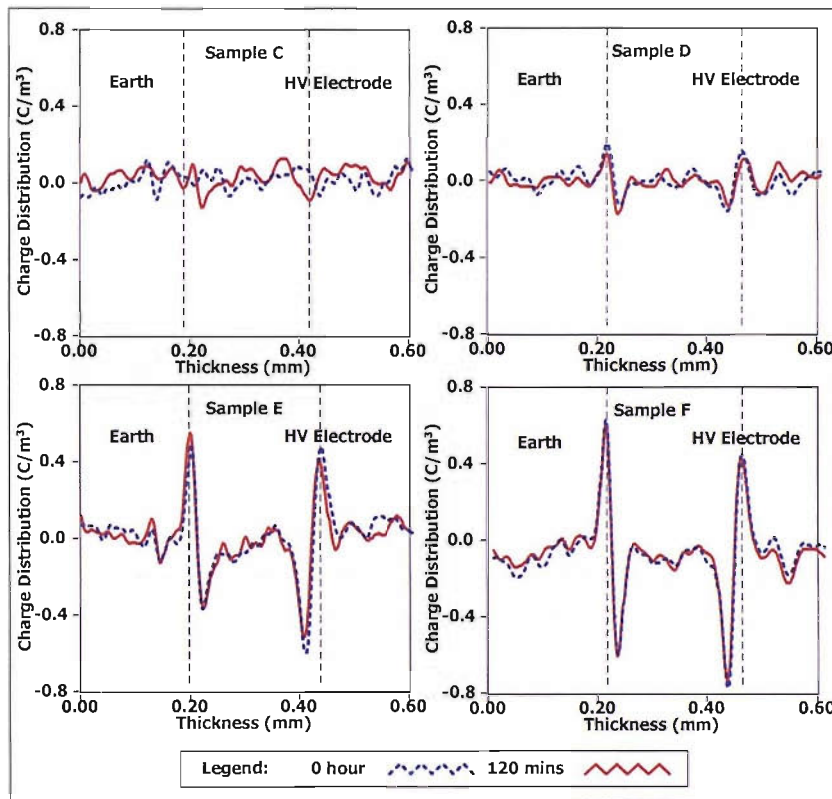
Figure 7.11: Volt-off charge profiles of samples C to F.

However, a quick comparison between the space charge profiles of samples B, C and D suggests otherwise. While at the lowest frequency of 1 Hz (sample B) saw the highest amount of charge trapped in the bulk but at the end of the scale did not see the

least amount of charge (sample D). In fact, it was sample C, which was aged at 10 Hz ac voltage, which exhibits negligible charge trapped in the bulk.

One possible explanation is that the contribution of space charge to ac ageing is speculated to be mainly due to a fatigue mechanism associated with the electromechanical energy stored or released in trapping/detrapping as well as to the electromechanical forces exerted by the injected charge in each half cycle [148]. Hence, at 50 Hz, sample D was subjected to more cycles of polarity reversal for the given ageing duration as compared to both samples B and C. This may result in more rapid degradation which may in turn result in formation of deeper traps.

All the samples tested under ac condition, with the exception sample C, were dominated by trapped negative charge. This suggests that ac ageing result in the formation of deep traps for negative charge.

It should be noted that in [35, 101], space charge were measured while ac voltage was applied on the sample while in the present study the charge measured were those trapped in the sample after the removal of voltage. This may be accountable for the difference in between the results.

Comparing the space charge profiles of sample D with samples E and F indicate increase in the amount of accumulated negative charge. This maybe attributed to the fact that higher electric stress enhances charge injection and also the process described before.

It was noted that relatively less decay of the trapped charge was observed in samples D, E and F as compared to samples A and B. This is probably attributable to the formation of more deep traps as a result of the higher frequency and/or electric stress which supports the hypothesis of deep traps formation.

The space charge profiles of both sample D and sample S1 indicate negative charge accumulation near the earth electrode. This confirms that the negative charge seen in figure 7.3 is not an artefact of the LIPP system but real trapped charge. Negative charge can also be seen in the vicinity of HV electrode of sample D, however, this is

not seen in sample S1. This is probably because the PEA system is more sensitive than the LIPP system for detection of small quantity charges. Also as sample S1 is thicker, the effect of attenuation and dispersion is more sever than sample D, hence making the already small amount of charge even smaller and eventually masked off by the oscillating noise.

Figure 7.12 shows the volt-off space charge profiles of samples G to L after 24 hours of ageing.
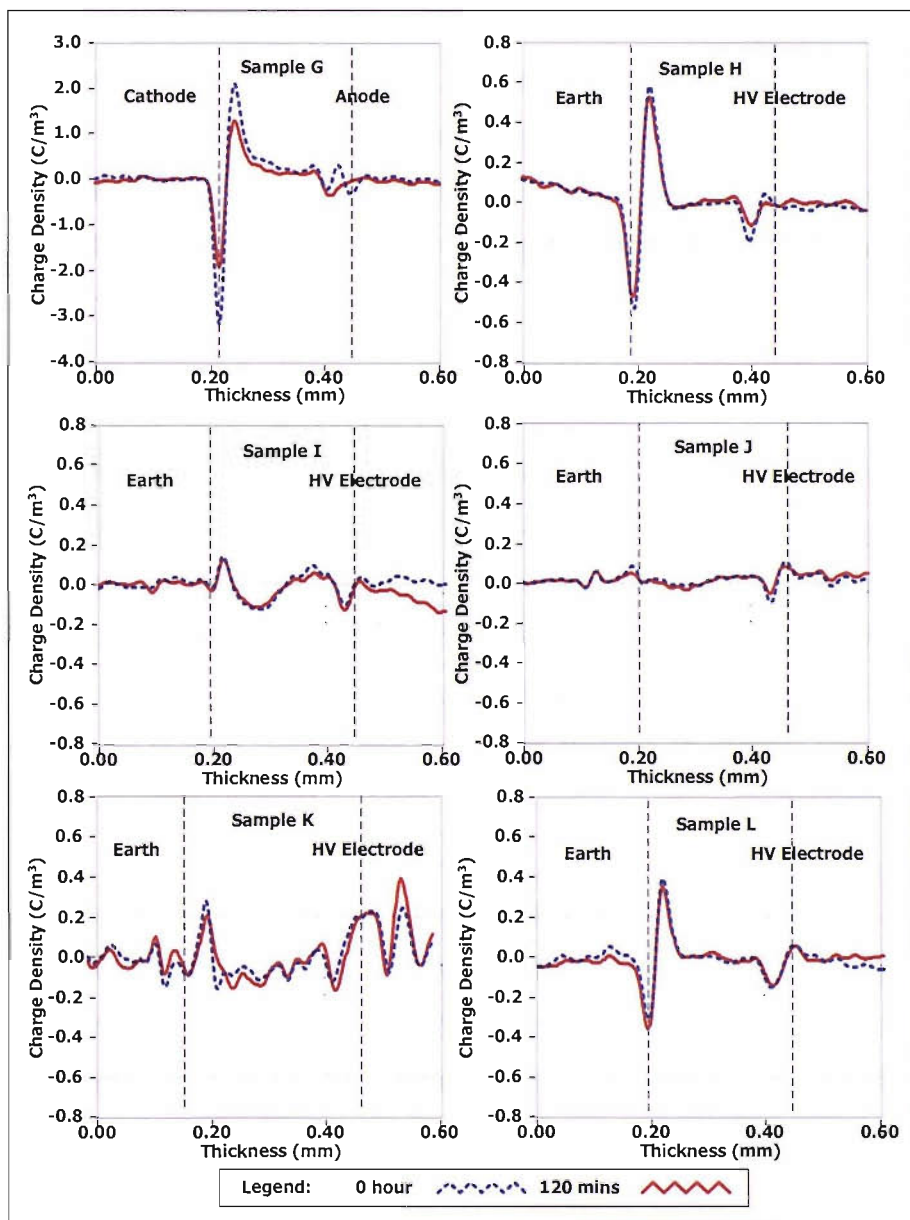
Figure 7.12: Volt-off charge profiles of samples G to L

A significant amount of positive heterocharge can be seen in the vicinity of the cathode of sample G after 24 hours of ageing. This is believed to be attributed to ionic dissociation of crosslinked by-products. A slight amount of positive homocharge can be seen adjacent to the anode and a layer of negative charge is sandwiched between it and the positive charges adjacent to the cathode. After the sample is short-circuited for 2 hours, considerable amount of charge reduction can be observed.

The short-circuit space charge profiles of sample H is dominated by positive charge accumulation near the earth electrode while a small amount of negative charge can be seen close to the HV electrode. An even smaller but opposite charge can be observed between these two layers of charges. This maybe due to charge carriers with lower mobility than the ones trapped near the two electrodes. Similar to sample G, charge reduction can be observed after short-circuiting the sample for 2 hours, although, by proportion, appears to relatively less.

The space charge profiles of sample I are somewhat similar to that of sample H, except the amount of the charges accumulated at the vicinity of the electrodes reduces while the charges in the bulk increases. This is probably because at 10 Hz, the frequency at which the voltage polarity varies is too fast for the charges caused by ionic dissociation of impurities and by-products to be trapped near the electrodes and hence remained in the middle of the bulk. While in the case of sample J, the voltage variation (50 Hz) is even greater and hence the amount of charges trapped is even smaller than that seen in sample I.

Comparing the results of as-received samples tested at 50 Hz, 30 kV_{pk}/mm ac electric stress measured using different systems shows negligible space charge trapped in the thicker sample measured using the LIPP system (sample S2) while a very small amount of charge can be seen in the thinner sample measured using the PEA system (sample J). Like before, this is probably because the PEA system is more sensitive than the LIPP when detecting small amount of charge.

Increasing the applied stress to 60 kV$_{pk}$/mm results in space charge distributions that resemble that of sample H. This can be clearly seen when comparing the short-circuit space charge distributions of sample H with sample L.

One possible explanation for this is at 50 Hz ac stress, the alternating voltage is constantly charging and discharging the sample. Hence it takes a much higher stress level to accumulate the kind of space charge it takes for a sample under ac stress of lower frequency and magnitude to accumulate. Perhaps not surprisingly, sample K, being aged at a stress level between that of samples J and L, has an intermediate space charge characteristic of the two.

It is worthy to note that for samples J to L, short-circuiting the samples for 2 hours result in little reduction in accumulated charge. This may be due to formation of deep traps caused by ac ageing.

The second phase of the experiment involved stressing samples B to F under dc electric stress. Samples H to L were not tested in this phase of the experiment as there is no track record on the concentration of crosslinked by-products in the samples.

It was confirmed that the charges trapped in the samples during the first phase of the experiment had decayed to an amount that can no longer be detected by the PEA system.

Before ageing the samples a simple step voltage test was conducted to investigate the threshold stress at which space charge initiates in the samples. The results are shown in figure 7.13.
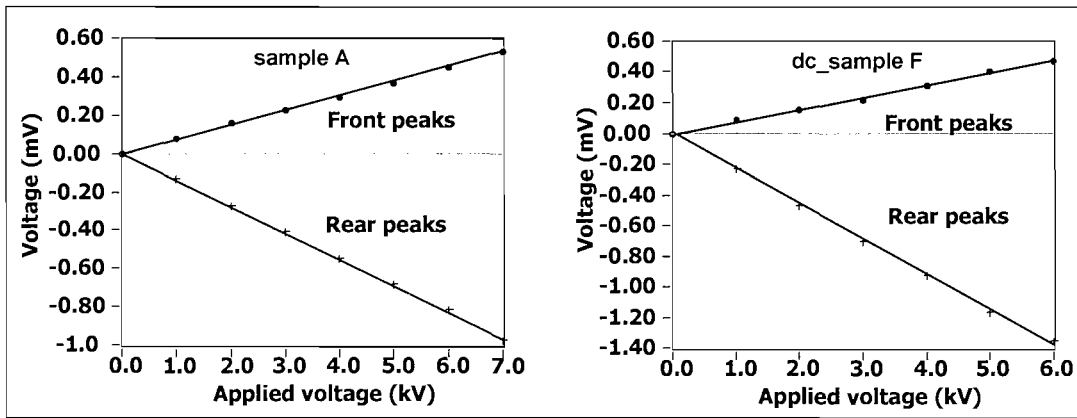
Figure 7.13: Step voltage test results of sample A and dc_sample F.

Space charge modifies the stress at the insulation/electrode interfaces which in turn causes the front and rear peaks to deviate from the extrapolated trend line. However, this is not seen in figure 7.13 suggesting that up to a stress level of 30 kV_{dc}/mm, no space charge is formed in the samples. The step voltage test results of dc_samples B to E are similar to that of sample A and dc_sample F and will not be shown here. While the results in this experiment suggest that the threshold voltage is not affected by ac ageing, it is worth pointing out that this deduction only holds true for applied stress of 30 kV_{dc}/mm or less.

The results of the volt-on space charge profiles of dc_samples B to F can be seen in figure 7.14.
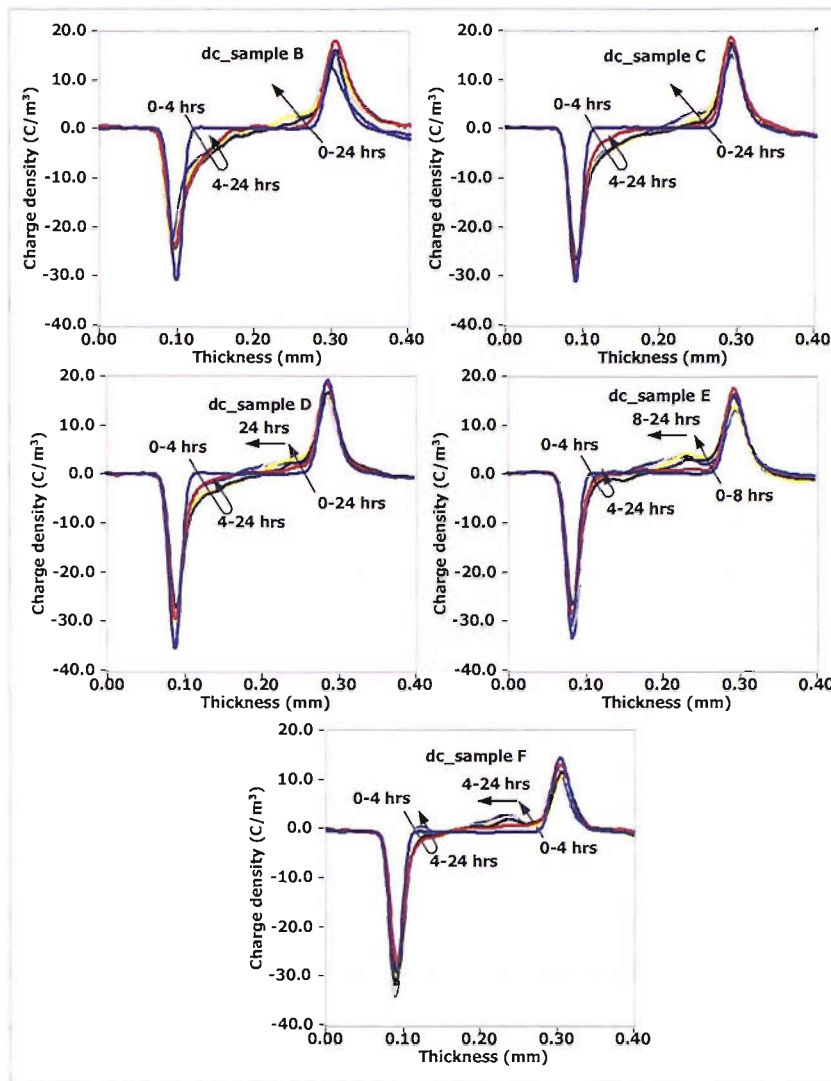
Figure 7.14: Volt-on charge profiles of dc_samples B to F.

With reference to figure 7.14, no significant space charge can be seen in dc_samples B to F at 0 hours, i.e. immediately after the step voltage test. This is consistent with the results of the step voltage test.

At 1 hour, homocharges can be seen accumulating near the vicinity of both electrodes in all the samples. As in the case of sample A, the formation of these homocharges is believed to be caused by charge injection from the semicon electrodes.

In the case of dc_samples B and C, increase in positive homocharge with increasing stress period was observed, with the negative homocharge reaching its maximum amount after 4 hours of ageing.

Similar behavior can be observed for the negative charge in dc_samples D to F, which appears to reach its maximum amount after 4 hours of ageing. However, in vicinity of the anode, positive packet charge can be seen; less obvious in dc_sample D as compare to E and F.

It has been reported that packet charge formation may be caused by charge carrier generation under high electric field (above 100 kV_{dc}/mm), antioxidant deteriorated by oxidation [45] and local ionization of impurities through salvation by acetophenone [149]. The samples used in this experiment, however, do not contain antioxidant and acetophenone is believed to be largely removed after the degassing process while the stress applied is much lower than 100 kV_{dc}/mm. Therefore, formation of packet charge is believed to be caused by the ac ageing during the first phase of the experiment.

Careful comparison of the charge profiles of dc_samples D, E and F indicates that the time for packet charge formation is dependent on the ac ageing conditions. From figure 7.14 packet charge only appears in dc_sample D after 24 hours of ageing while it only takes 8 hours in the case of dc_sample E and 4 hours for dc_sample F. It is noteworthy that after it initiates, the packet charge tends to move towards the cathode with ageing time as indicated by the arrows.

According to the findings reported in [142], positive charge packet can be observed only when the positive charge is the dominate carrier. Similar conclusion can be drawn by looking at figure 7.14, which shows that dc_samples D to F are dominated by positive charge. A quick look at figure 7.15, which shows the space charge profiles of all the samples with the volt-off after the 24 hours of ageing, further confirms this.
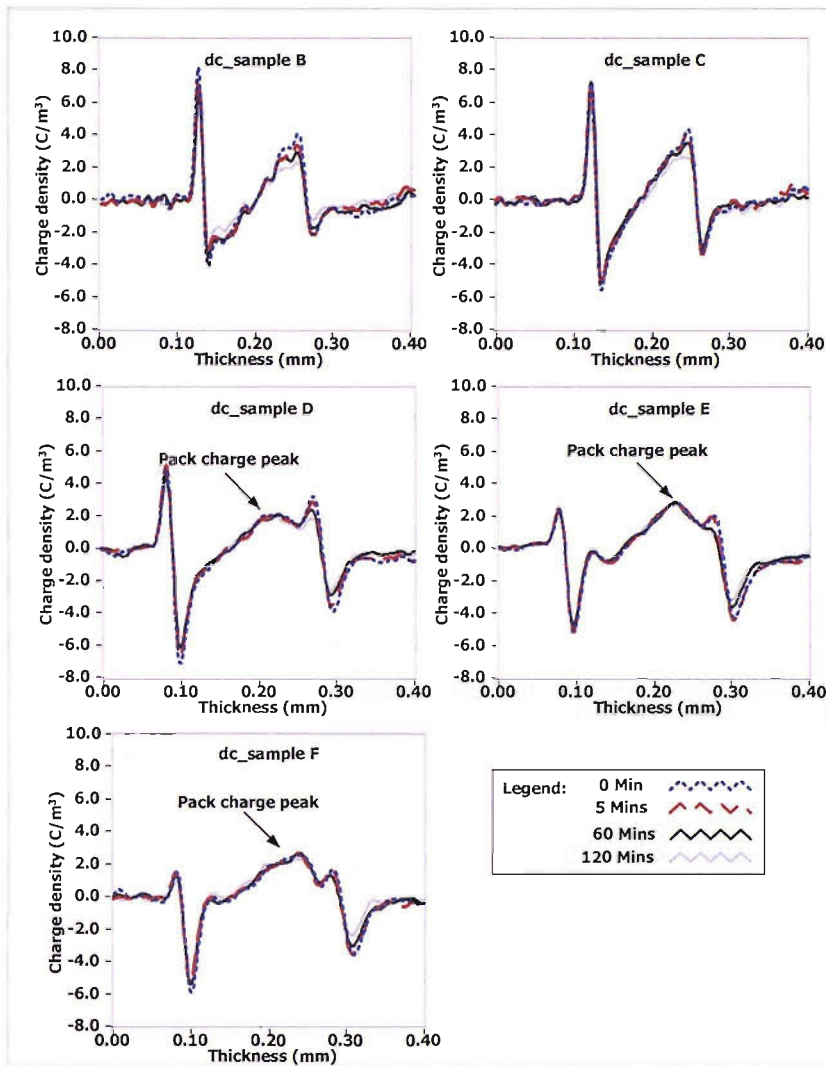
Figure 7.15: Volt-off charge profiles of dc_samples B to F.

The amount of positive and negative charges trapped in sample A are almost equal as seen in figure 7.6(b). In the case of dc_sample B, positive charge appears to be more dominant, moving more towards the cathode. This effect is even more profound in dc_samples C and E. This is probably due to the difference in frequencies of the ac electric stress they were subjected during the first phase of the experiment.

One way to explain this is at 1Hz, dc_sample B was subjected to 10 and 50 times less cycles of polarity reversal as compared to dc_samples C and D respectively. Therefore, the effect of ac ageing experienced by dc_sample B can be viewed as much lesser comparatively.

Increasing the ac stress level seems to enhance the effects exhibited in dc_samples B to D. This can be clearly seen in the space charge profiles of dc_samples E and F in figures 7.14 and 7.15.

The space charge distributions of dc_samples D to F shown in figure 7.15 indicate two peaks in the positive charge trapped in the bulk. This is not seen in samples A, dc_samples B to C. The second peak, as indicated by the arrow, appears to correspond to the packet charge seen in figure 7.14.

The packet charge peak tends to be positioned closer to the cathode when the pre-ageing ac stress is higher. This can be clearly seen by comparing the space charge profiles of dc_samples D to F in figure 7.15.

Therefore, positive charge propagation may be an indication of the material degradation. Indeed, studies have shown some relation between propagation of positive charge and the intrinsic breakdown of insulating materials [107, 130]. This may be attributed to the fact that as positive charge propagates closer to the cathode, the interfacial stress at the cathode increases which eventually lead to electrical breakdown.

However, due to limited results no direct relationship can be observed between positive charge propagation and the extent of material degradation or life expectancy. More experimental results are needed before any firm conclusion may be drawn regarding this issue.

The mechanism of which the packet charge forms and moves is believed to be the same as reported in [142]. To summarise, positive charge injected from the anode moves towards the cathode under the influence of the effective stress, E_e (x), which can be described as:

$$E_e(x) \quad = \quad E_a + E_c(x) \tag{7.2}$$

where E_a = the applied stress and

E_c (x) = the stress from space charge distribution

As more positive charge is injected into the bulk, the interfacial stress at the anode reduces and hence the rate of charge injection also reduces. The positive charge then moves towards the cathode under the influence of the effective stress. This probably explains why the positive packet charge in dc_sample F is smaller and penetrates deeper into bulk.

Reduction of positive charge can be seen in sample A, dc_samples B and C after the voltages were removed for 5 minutes. On the other hand, insignificant reduction in positive charge can be observed in dc_sample D to F after voltage removal for the same duration.

In order to confirm this, the integration of the charge densities (Q) across the bulk was calculated using equation 5.3. Figure 7.16 shows the integral of the positive charge of 4 different samples at various times after the removal of voltage.
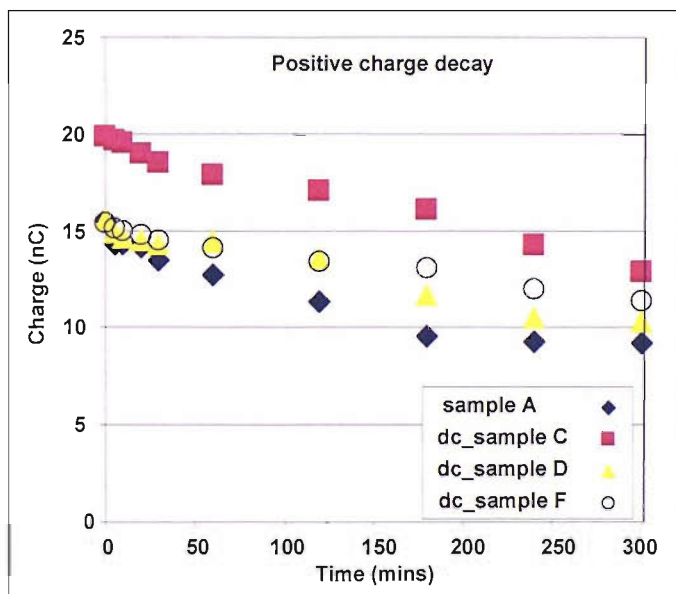
Figure 7.16: Positive charge decay in selected samples after voltage removal for 5 hours

It can be seen that the positive charge in sample A and dc_sample C decays more rapidly than those of dc_samples D and F. This suggests that charges are trapped more deeply in the latter as compared to the former. Hence, it is believed that ac ageing results in the formation of deep traps. This is consistent with the observation in LDPE after ac ageing [135, 137].

134

With reference to figure 7.15, it is also noted that the reduction of negative trapped charge is relatively less as compared to that of positive charge. This may imply that ac ageing causes the formation of traps that are more stable for negative charge.
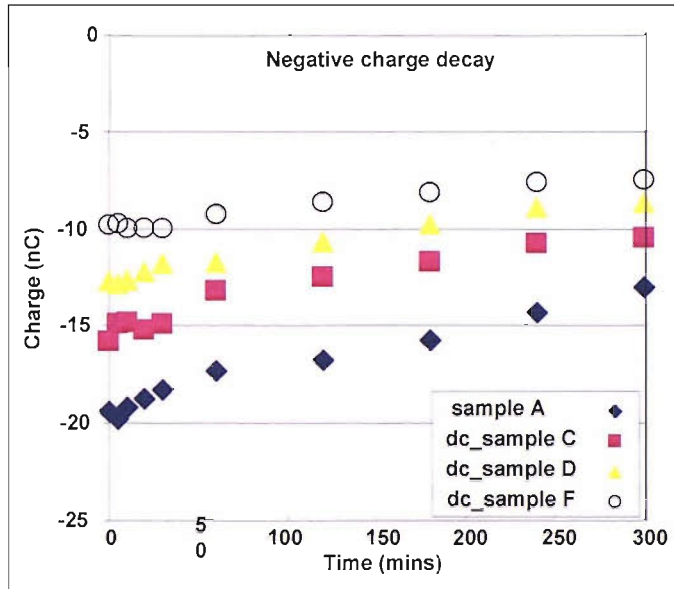
Figure 7.17: Negative charge decay in selected samples after voltage removal for 5 hours

Figure 7.17, which shows the integral of the negative charge of the same 4 samples, confirms that negative charge of dc_samples decay at a slower rate than their positive counterpart.

The concept of fast charge was mentioned earlier. Fast charges, in the context of this study, refer to charges which disappear almost immediately after the removal of the applied stress. As a time lag of approximately 2-3 seconds is needed between the removal of voltage and the measurement of space charge, the '0 min' of the volt-off space charge profiles presented thus far does not take fast charge into account. If electrical ageing modifies the trap depth, it may also affect fast charge.

Although it is impossible to measure fast charge in a sample practically, it can be, however, be computed using equation 6.5.

Using equations 6.2 and 7.1, $\rho_{accumulated}$ *(x)* is obtained and subsequently substituted into equation 6.5. The fast charge profiles are shown in figure 7.18.
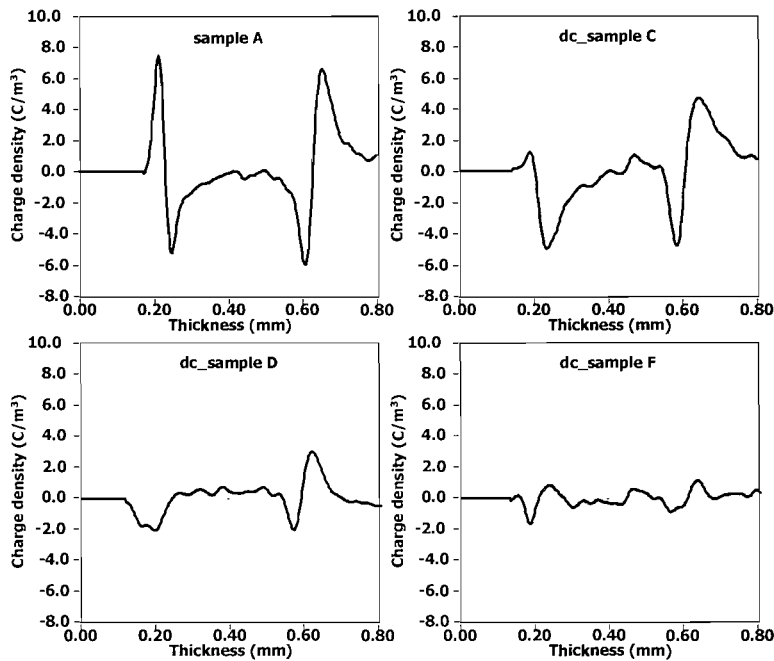
Figure 7.18: Fast charge of selected samples

As seen in figure 7.18, of the four selected samples, sample A has the most amount of fast charge. This suggests that sample A has the most amount of shallow traps. On the other hand, dc_sample F shows the least amount of fast charge which suggests it has the least number of shallow traps. Based on these limited data, it seems that the more sever the electrical ageing, the lesser the amount of fast charge. More experimental work needs to be carried out on different materials before any firm conclusion on fast charge and its relation to material degradation can be drawn.

7.5   Conclusion

Space charge evolution in XLPE planar samples, subjected to dc and ac electric stress has been investigated using both the LIPP and the PEA technique. The LIPP system is only limited to measuring space charge at 50 Hz ac electric stress while in the PEA system, space charge characteristics in samples under 1 Hz, 10 Hz and 50 Hz ac electric stress were investigated.

In the LIPP system, small amount of negative charge can be seen in the vicinity of the earth electrode in the degassed sample after 24 hours of ac ageing while no charge was observed in the as-received sample. This difference is probably attributed to the

136

higher conductivity of as-received sample, making it more difficult for charge to be trapped.

Apart from degassed sample subjected to 10 Hz ac electric stress, accumulated space charge, albeit very small amount, can be seen in all the samples tested using the PEA system. It is believed that a combination of ionic dissociation, charge injection, trapping, formation of deep traps and material degradation caused by ac ageing is accountable for the observed phenomena.

Increasing the applied ac electric stresses increase the amount of charge trapped in the samples, although it is still significantly lesser than the amount of charge trapped in sample subjected to dc electric stress.

The space charge dynamics of the degassed samples used for the investigation of ac space charge were tested again under dc electric stress. The results showed the threshold stress at which space charge initiates was not affected by the ac ageing. Furthermore, positive charge becomes more dominant after the samples were aged under ac stress. The higher the frequency and/or magnitude of the ac stress, the more dominant positive charge over negative charge.

As positive charge became more and more dominant, positive packet charge was formed. These were observed in samples that were aged under 50 Hz ac. The formation and dynamics of the packet charge were explained.

Charge accumulated during dc stress period was allowed to decay for five hours. It seems that ac ageing results in the formation of deeper traps, particularly for negative charge carriers.

8 Conclusion and further work

8.1 Conclusion

The work presented in this thesis mainly concerns the space charge in XLPE insulation under dc and ac electric stresses. Two techniques were used in this study, namely the LIPP and the PEA method.

The LIPP system reported in this report is capable of measuring space charge in XLPE under both dc and 50 Hz ac electric stress. The basic principles behind dc and ac space charge were reviewed.

In order to improve on the performance of the LIPP system, a programme using LabVIEW was developed to automate the system. This has been done with considerable success although further improvements are still needed before the LIPP system can be fully automated.

Through the course of experimenting with the LIPP system, problems concerning the target cooling system were encountered. One obvious way to get around this problem is not to use the target cooling system; firing directly at the target electrode. Apart from eliminating the problem associated with the choice of cooling agent, this solution also has the advantage of improved spatial resolution. However, the effect of target ablation will become significant for ac space charge measurement which requires numerous laser pulses to be fired within a short period of time.

Another possible solution is to place a metal (aluminum) plate in front of the target electrode. Since metal is hard as compared to semicon, the effect of ablation is therefore less significant. In addition to that, with the help of the aluminum plate, the spatial resolution of the system can be improved.

The output signal from the LIPP is distorted due the system's response. The low frequency element was affected due to the implementation of the liquid cooling system. This was dealt with reasonable success by filtering away the low frequency

component. The rear peak of the measured waveform was caused by the acoustic mismatch between semicon and the HV metal electrodes.

The raw output obtained from the LIPP needs to be calibrated and converted to charge density distribution before quantitative data can be extracted. A data processing methodology for calibration and calculation of space charge density, which also takes into account the attenuation and dispersion of pressure as it propagates through the sample was also covered.

The principle behind the PEA technique was briefly explained. Unlike the LIPP system, the PEA system used in this study is capable of measuring space charge in a dielectric sample under both dc and ac electric stress of various frequencies. The concept of point-on-wave measurement as applied to measurement of ac space charge was also presented.

Due to the inherent response of the PEA system, there is distortion to the output signal. A data processing treatment known as deconvolution is required to recover the original signal. The main idea behind the concept of deconvolution was also covered.

A comparison between the PEA technique and LIPP technique was made and some of the improvements on the PEA system since its development were also presented. It was concluded that both the LIPP and PEA has their strengths and short-comings and the choice of technique solely depends on measuring conditions and requirements.

The influence of degassing has on the morphological development and space charge in XLPE planar samples was investigated. Parameters such as degassing duration, degassing temperature and sample thickness were altered.

Results showed that more volatile by-products can be removed by increasing the duration and temperature of degassing. It is also proven that it is easier to remove the by-products from thinner samples.

Along with removing volatile by-products, annealing of the samples also occurs during degassing. DSC results indicate that factors that affect the morphological development include degassing duration, temperature and thickness of the sample. TEM also indicates changes in the lamellar structures due to different degassing temperature.

The dc ageing experiments suggest that space charge distribution is highly dependent on the amount of by-products in the samples. Complicating space charge behavior is attributed to ionic dissociation, charge injection/extraction and recombination.

The effect of temperature on space charge for as-received and degassed samples was also investigated. The testing temperature was between 30 to 90 $^{\circ}$C. The threshold stress at which space charge accumulates are found to be greatly affected by temperature. Charge mobility and energy increase with temperature as such, the amount of trapped charge reduces.

At high temperature, the space charge distribution was dominated by positive charge and at 70 $^{\circ}$C or above, the space charge distribution takes the same form regardless of whether the sample is as-received or degassed. Futhermore, positive charge propagation enhances as temperature increases, which can be worrying as such behaviour is related to insulation breakdown.

Part of this research work includes a student exchange programme to Musashi Institute of Technology in Japan. Over there, a PEA system that is capable of measuring space charge under both dc and ac stress was already built. Both dc and ac space charge experiments were conducted.

Experiments on samples subjected to ac electric stress indicate that space charge under ac condition is not as profound as samples under dc stress. Accumulated space charge, albeit very small amount, can be seen in most of the samples tested using the PEA system. No significant charge can be observed in the degassed sample subjected to 10 Hz ac electric stress, while accumulation of negative charges was observed in degassed samples at frequencies of 1Hz and 50 Hz.

Complicating space charge distributions were seen in as-received samples under different frequency and stress level. For degassed samples, it was observed that the magnitude of the applied stress only affects the magnitude of the trapped charge but not the nature of it.

The degassed samples used for the ac PEA space charge investigation were re-used for dc space charge experiment to examine the effect of ac ageing on space charge dynamics and trapping. It was discovered that with increasing frequency and/or stress level, positive charge becomes more and more dominant, until a point whereby packet charge can be observed. This positive packet charge propagates more towards the cathode when the sample has been pre-aged at higher ac stress. It was also observed that the trapped charge decayed slower when the sample was pre-aged at higher frequency and/or stress level. It is believed that like in dc, ac ageing results in the formation of deep traps.

8.2   Future work

While degassing duration and temperature on space charge and morphology has been investigated, the full picture of morphology has on space charge and depth of space charge trap-centres is still unclear. One possible way is to investigate the rate at which space charge decay in a sample.

The other objective of this research work is to compare space charge under dc electric stress with that under 50 Hz ac electric stresses. Space charge under ac stress is often considered to be more complex because the stress level at which the sample experience varies with time. Therefore, it is necessary to investigate dc space charge before going into ac space charge.

The same experimental protocols for dc space charge can be repeated only this time the samples are subjected to 50 Hz ac stresses. The effect of sample treatment and testing temperature on ac space charge hence can be understood.

The samples used in this report were all planar XLPE samples. It will be interesting to know how the results will be affected when the same experimental protocols were used on XLPE material in cable geometry.

Through the ac space charge experiment, very little space charge effect was observed. There is no doubt that when an insulating material is subjected to ac stress, the material degrades. However, reports have shown that techniques such as FTIR and the Raman spectroscopy were not able to detect very distinct difference in materials with and without ageing.

It this thesis, it has been shown that space charge measurement technique is extremely sensitive to material degradation. It has also been shown here as well as in other literatures that more severely aged samples have deeper traps [132, 133, 135, 137]. The problem with this method is that a virgin sample of the same material is required as a comparative reference. This is usually not available when diagnosis of an existing cable that has been in operation for sometime is required. Although limited results, the concept of fast charge as discussed in this report may be a good start off point.

Meunier el at [150, 151] shows that by defining the defect energy in terms of the molecular electron affinity, a relationship can be established between electron trap and the molecular properties of the material. Hence, if the trap depth of the charge can be estimated, say using the thermally simulated current (TSC) technique, it may be possible to provide a better understand the relationship between electrical ageing with physical and/or chemical defects.

Lastly, modelling of the space charge behaviour can also be attempted. This will lead to a better idea of space charge injection and mechanism.

References

[1]   B.M. Weedy, "*Underground transmission of electric power.*" 1980: J. Wiley and Sons.

[2]   F. Rodriguez, "*Principle of polymer science.*" 1983: McGraw-Hill.

[3]   T. Fukuda, S. Irie, Y. Asada, M. Maeda, H. Nakagawa, and N. Yamada, "*The effect of morphology on the impulse voltage.*" IEEE Transactions on Electrical Insulation, 1982: p. 386-391.

[4]   B. Brijs, J. Becker, G. Geerts, and X. Delfree, "*150 kv underground links in belgium: A new technical stage on xlpe insulation cables.*" CIGRE, 2000: p. 21-101.

[5]   M. Ieda, "*Electrical conduction and carrier traps in polymeric materials.*" IEEE Transactions on Electrical Insulation, 1984: p. 162-178.

[6]   J.W. Billing, "*Examination of thin tape produced from extruded cable insulation.*" IEE International Conferenece on Dielectric Materials, Measurements and Applications, 1984: p. 195-198.

[7]   S.G. Swingler, "*On the short-term electric strength of polyethylene film.*" IEE International Conferenece on Dielectric Materials, Measurements and Applications, 1988: p. 1-4.

[8]   I.U.o.P.a.A. Chemistry, "*Report on nomenclature in the field of macromolecules.*" J. Polymer Science, 1952: p. 257-277.

[9]   http://www.stark.kent.edu/~cearley/ChemWrld/polymers/polymers.htm

[10]   M. Ieda, T. Mizutani, and Y. Suzuoki, *"Tsc and tl studies of carrier trapping in insulating polymers."* Nagoya University Memoirs of The Faculty of Engineering, 1980: p. 173-219.

[11]   M.A. Brown, *"Spacecharge, breakdown and lifetime estimation of polyethylene insulation systems"*,thesis, University of Southampton, 2002.

[12]   G.A. Cartwright, *"The measurement of space charge and its effect on the breakdown strength of solid polymeric insulation"*,PhD thesis, University of Southampton, 1994.

[13]   T.J. Lewis, *"Electrical effects at interfaces and surfaces."* IEEE International Symposium on Electrets, 1986: p. 75-87.

[14]   J.G. Simmons, *"Conduction in thin dielectric films."* Journal of Applied Physics D, 1971: p. 613-657.

[15]   N.F. Mott and R.W. Gurney, *"Electronic processes in solids."* 1948: Calredon Press, Oxford.

[16]   R.H. Fowler and L.W. Nordheim, *"Electronic emission in intense electric fields."* Proceeding of The Royal Society London A199, 1928: p. 173-181.

[17]   J.C. Slater, *"Insulators, semiconductors and metals."* 1967: McGraw-Hill.

[18]   R.M. Eichhorn, *"Organic residues in polyethylene insulation cross-linked with dicumyl peroxide."* IEEE Underground Transmission Conference, 1972: p. 282-285.

[19]   P.J. Flory, *"On the morphology of the crystalline state in polymers."* Journal of American Chemical Society, 1962: p. 2857-2867.

[20]   P.J. Phillips, "*Morphology-electrical property in relations in polymers.*" IEEE Transactions on Electrical Insulation, 1978: p. 69-81.

[21]   Y. Takai, K. Mori, T. Mizutani, and M. Ieda, "*Investigation of traps in γ-irradiated polyethylene by photo stimulated detrapping current analysis.*" Journal of Applied Physics, 1989: p. 2341-2347.

[22]   Y. Suzuoki, K. Yasuda, T. Mizutani, and M. Ieda, "*The influence of oxidation on thermally stimulated current from trapped carriers in high density polyethylene.*" Journal of Applied Physics, 1977: p. 1985-1990.

[23]   J. Perret and R. Fourine, "*Space charge in polyethylene for high voltage cables.*" IEE International Conferenece on Dielectric Materials, Measurements and Applications, 1975: p. 83-86.

[24]   M.S. Khali and B.S. Hansen, "*Investigation of space charge in low density polyethylene using a field probe technique.*" IEEE Transactions on Dielectrics and Electrical Insulation, 1988: p. 441-445.

[25]   M. Flack, G. Dreyfus, and J. Lewiner, "*Vapour-induced depolarization currents i. Models.*" Physical Review A, 1982: p. 5499-5508.

[26]   M. Flack, G. Dreyfus, and J. Lewiner, "*Vapour-induced depolarization currents ii. Models.*" Physical Review A, 1982: p. 5509-5514.

[27]   S.B. Lang and D.K. Das-Gupter, "*A new technique for determination of the spatial distribution of polarization in polymer electrets.*" Ferroelectrics, 1984: p. 23-36.

[28]   S.B. Lang and D.K. Das-Gupter, "*A technique for determining the polarization of distribution in thin polymer electrets using periodic heating.*" Ferroelectrics, 1984: p. 1249-1252.

[29] A.S. DeReggis, C.M. Guttman, F.L. Mopsik, G.T. Davies, and M.G. Broardhurst, *"Determination of charge or polarization distribution across polymer electrects by thermal pulse method and fourier analysis."* Physical Review Letters, 1978: p. 413-416.

[30] H. Von Seggern, *"Thermal pulse technique for determining charge distributions: Effect of measurement accuracy."* Applied Physics Letter, 1978: p. 134-137.

[31] M.S. Khali, A. Cherifi, A. Toureille, and J.-P. Reboul, *"Influence of batio$_3$ additive and electrode material on space-charge formation in polyethylene evidence from thermal step space-charge measurements."* IEEE Transactions on Dielectrics and Electrical Insulation, 1996: p. 743-746.

[32] G. Dreyfus, J. Lewiner, and M. Legrand, *"Electron-spin resonance study of electron-bombarded polymer electrets i. Radical formation, piezoelectric and pyroelectric effects."* Physical Review B, 1979: p. 1720-1724.

[33] F.P. Chen, S.J. Sheng, and D.M. Hanson, *"Dielectric breakdown and space charge effect in molecular crystal stark spectroscopy."* Journal of Chemical and Physics, 1974: p. 60-71.

[34] M. Zahn, K.A. Hikita, K.A. Wright, C.M. Cooke, and J. Brennan, *"Kerr electro-optic field mapping measurements in electron beam irradiated polymethlmethacrylate."* IEEE Transactions on Electrical Insulation, 1987: p. 181-185.

[35] T. Takada, *"Acoustic and optical methods for measuring of electric charge distributions in dielectrics."* IEEE Transactions on Dielectrics and Electrical Insulation, 1999: p. 519-547.

[36]   W.N. Ross, B.M. Salzberg, L.B. Cohen, A. Grinvald, H.V. Davila, A.S. Waggoner, and C.H. Wang, "*Changes in absorption fluorescence, dichroism and birefringence in stained giant axons: Optical measurement of membrane potential.*" Journal of Membrane Biology, 1977: p. 141-183.

[37]   P. Laurenceau, G. Dreyfus, and J. Lewiner, "*New principle for the determination of potential distribution in dielectrics.*" Physical Review Letters, 1977: p. 46-49.

[38]   C. Alquie, F. Chapeau, and J. Lewiner, "*Evolution of charge distributions in f.E.P. Films analysed by the laser induced acoustic pulse method.*" IEEE International Conferenece on Electrical Insulation and Dielectric Phenomena, 1984: p. 488-494.

[39]   C. Alquie, G. Charpak, and J. Lewiner, "*Pulsed laser determination of surface electric charge distributions.*" Journal De Physique Lettres, 1982: p. L-687-L-693.

[40]   C. Alquie, T. Ditchi, and J. Lewiner, "*Measurement of charge distribution in insulating materials for high voltage cables.*" IEEE International Conference on Properties and Applications of Dielectric Materials, 1988: p. 434-437.

[41]   C. Alquie, G. Dreyfus, and J. Lewiner, "*Stress-wave probing of electric field distribution in dielectrics.*" Physical Review Letters, 1981: p. 1483-1487.

[42]   C. Alquie, J. Lewiner, and G. Dreyfus, "*Analysis of laser induced acoustic pulse probing of charge distributions in dielectrics.*" Journal De Physique Lettres, 1983: p. L-171-L-178.

[43]   K. Bambery and R. Fleming, "*The temperature dependence of space charge accumulation in crosslinked polyethylene.*" IEEE International Symposium on Electrets, 1996: p. 16-21.

[44]   K. Bambery and R.J. Fleming, "*Space charge accumulation in two power cable grades of xlpe.*" IEEE Transactions on Dielectrics and Electrical Insulation, 1998: p. 103-109.

[45]   H. Kon, Y. Suzuoki, T. Mizutani, M. Ieda, and N. Yoshifuji, "*Packet-like space charges and conduction current in polyethylene cable insulation.*" IEEE Transactions on Dielectrics and Electrical Insulation, 1996: p. 380-385.

[46]   T. Mizutani, Y. Suzuoki, T. Furuta, M. Ieda, and T. Suzuki, "*Direct observation of space charge distribution in polyethylene.*" IEEE International Conference on Electrical Insulation and Dielectric Phenomena, 1989: p. 309-314.

[47]   S. Mahdavi, Y. Zhang, C. Alquie, and J. Lewiner, "*Determination of space charge distributions in polyethylene samples submitted to 120 kv dc voltage.*" IEEE International Conference on Electrical Insulation and Dielectric Phenomena, 1990: p. 520-526.

[48]   S. Mahdavi, C. Alquie, and J. Lewiner, "*Direct measurement of space charge in synthetic cables by the pressure wave method.*" Jicables, 1991: p. 534-541.

[49]   S. Mahdavi, C. Alquie, and J. Lewiner, "*Measurement of charge distributions in coaxial structures application to high voltage cables.*" IEEE International Conference on Electrical Insulation and Dielectric Phenomena, 1989: p. 296-302.

[50]   A.C. Tam, *"Pulsed laser generation of ultrashot acoustic pulses: Application for thin film ultrasonic measurements."* Applied Physics Letter, 1984: p. 510-512.

[51]   J. Lewiner, *"New experimental techniques."* IEEE International Symposium on Electrets, 1985: p. 429-443.

[52]   J. Lewiner, *"Evolution of experimental techniques for the study of the electrical properties of insulating materials."* IEEE Transactions on Electrical Insulation, 1986: p. 351-360.

[53]   J. Lewiner, *"Direct determination of space charge distributions in dielectrics: The pressure wave propagation method."* IEEE International Conference on Conduction and Breakdown in Solid Dielectrics, 1989: p. 548-554.

[54]   D. Malec, *"Technical problems encountered with the laser induced pressure pulse method in studies of high voltage cable insulators."* Measurement Science and Technology, 2000: p. N-76-N80.

[55]   R.G. Multhaupt, *"Analysis of pressure-wave methods for the nondestructive determination of spatial charge or field distributions in dielectrics."* Physical Review B, 1983: p. 2494-2503.

[56]   G.M. Sessler, *"Charge distribution and transport in polymers."* IEEE Transactions on Dielectrics and Electrical Insulation, 1997: p. 614-628.

[57]   G.M. Sessler, R.G. Multhaupt, H. von Seggern, and J.E. West, *"Charge and polarization profiles in polymer electrets."* IEEE Transactions on Electrical Insulation, 1986: p. 411-415.

[58]   G.M. Sessler, J.E. West, D.A. Berkley, and G. Morgenstern, *"Determination of spatial distribution of charges in thin dielectrics."* Physical Review Letters, 1977: p. 368-371.

[59]   G.M. Sessler, J.E. West, and G. Gerhard, *"Measurement of charge distribution in polymer electrets by a new pressure-pulse method."* Polymer Bulletin, 1981: p. 109-111.

[60]   G.M. Sessler, J.E. West, and G. Gerhard, *"High-resolution laser-pulse method for measuring charge distributions in dielectrics."* Physical Review Letters, 1982: p. 563-566.

[61]   G.M. Sessler, J.E. West, R.G. Multhaupt, and H. Von Seggern, *"Nondestructive laser method for measuring charge profiles in irradiated polymer films."* IEEE Transactions on Nuclear Science, 1982: p. 1644-1649.

[62]   Y. Zhang, J. Lewiner, and C. Alquie, *"Evidence of strong correlation between space-charge buildup and breakdown in cable insulation."* IEEE Transactions on Dielectrics and Electrical Insulation, 1996: p. 778-783.

[63]   Y. Zhang, J. Lewiner, C. Alquie, and R.N. Hampton, *"Space charge of differencet mobiliities: A novel data processing method."* Journal of Applied Physics, 1995: p. 5195-5200.

[64]   Y.F.F. Ho, Y.L. Chong, and G. Chen, *"Temperature effect on the space charge characteristics in as-received and degassed xlpe insulation under dc electric sressing conditions."* IEEE International Conference on Electrical Insulation and Dielectric Phenomena, 2003: p. 241-244.

[65]   Y.F.F. Ho, Y.L. Chong, and G. Chen, *"Optimization of the aluminum target thickness on the space charge measuremet using lipp technique."* IEEE International Conference on Electrical Insulation and Dielectric Phenomena, 2003: p. 237-240.

[66]   Y.L. Chong, G. Chen, and Y.F.F. Ho, *"Effect of the length of degassing period on the space charge dynamics in xlpe insulation under dc stressing condition."* IEEE International Conference on Solid Dielectics, 2004: p. 162-165.

[67]   Y.L. Chong, Y.F.F. Ho, and G. Chen, "*Automation of space charge measurement by using lipp technique.*" International Conference on Insulation Condition Monitoring of Electrical Plant, 2003: p. 168-171.

[68]   G.A. Cartwright, R.N. Hampton, A.E. Davies, S.G. Swingler, D. Patel, and S.M. Moody, "*The laser induced pressure pulse technique for space charge measurements - a user's perspective.*" IEEE International Conference on Conduction and Breakdown in Solid Dielectrics, 1995: p. 595-599.

[69]   Y.F.F. Ho, "*Space charge measurement in xlpe- a comparison of ac and dc stress*",*PhD thesis, University of Southampton, 2001.*

[70]   M.A. Brown, G. Chen, A.E. Davies, L.A. Dissado, and P.A. Norman, "*Space charge characterisation in aged ldpe amalgamated insulation regions, from underwater telecommunication systems.*" IEEE Transactions on Dielectrics and Electrical Insulation, 2000: p. 346-352.

[71]   M.A. Brown, G. Chen, and P.A. Norman, "*High voltage performance of bulk, and amalgamated, pe insulation systems: Part i. Space charge characteristics.*" Journal of Physics D: Applied Physics, 2003: p. 3191-3196.

[72]   G. Chen, A.E. Davies, H.M. Banford, N. Adachi, Y. Tanaka, and T. Takada, "*The role of oxidation in the formation of space charge in gamma-irradiated low-density polyethylene.*" IEE International Symposium on High Voltage Engineering, 1999: p. 75-78.

[73]   A.E. Davies, G. Chen, and A. Vazquez, "*Space charge measurement in dispersive dielectrics.*" Jicables, 1999: p. 733-738.

[74]   T. Ditchi, C. Alquie, J. Lewiner, R. Favrie, and R. Jocteur, "*Electrical properties of electrode-polyethylene-electrode structures.*" IEEE International Symposium on Electrets, 1988: p. 7-12.

[75] T. Ditchi, C. Alquie, J. Lewiner, R. Favrie, and R. Jocteur, *"Electrical properties of electrode/polyethylene/electrode structure."* IEEE Transactions on Electrical Insulation, 1989: p. 403-408.

[76] T. Doi, Y. Tanaka, and T. Takada, *"Measurement of space charge distribution in acetophenone coated low-density polyethylene."* IEEE International Conferenece on Electrical Insulation and Dielectric Phenomena, 1997: p. 32-35.

[77] T. Doi, Y. Tanaka, and T. Takada, *"Short interval measurement of space charge distribution in acetophenoen coated low-density polyethylene."* IEEE International Conference on Properties and Applications of Dielectric Materials, 1997: p. 810-813.

[78] W. Eisenmenger and M. Haardt, *"Observation of charge compensated polarization zones in polyvinylindenfluoride (pvdf) films by piezoelectric acoustic step-wave response."* Solid State Communications, 1982: p. 917-920.

[79] R. Fleming, *"Space charge in polymers, particularly polyethylene."* Brazilian Journal of Physics, 1999: p. 280-294.

[80] K. Fukunaga and T. Maeno, *"Measurement of the internal space charge distribution of an anti-electrostatic discharge polymer."* IEEE Transactions on Dielectrics and Electrical Insulation, 1995: p. 36-39.

[81] K. Fukunaga, T. Maeno, and K. Okamoto, *"Three-dimentional space charge observation of ion migration in a metal-based printed circuit board."* IEEE Transactions on Dielectrics and Electrical Insulation, 2003: p. 458-462.

[82] J.L. Gil-Zambrano and C. Juhasz, *"Space charge polarisation in nylon films."* Journal of Physics D: Applied Physics, 1982: p. 119-128.

[83]   A. Gustafsson, C. Tornkvist, and M. Lindgren, *"Measurement of space charge accumulation: Influence of laminate boundaries in polyethylene."* IEEE International Conference on Conduction and Breakdown in Solid Dielectrics, 1995: p. 279-282.

[84]   N. Hirai, Y. Maeno, T. Tanaka, and Y. Ohki, *"Roles of cumyl alcohol and crosslinked structure in homo-charge trapping in crosslinked polyethylene."* IEEE International Conference on Electrical Insulation and Dielectric Phenomena, 2003: p. 213-216.

[85]   L. Liang, W. Xia, and T. Demin, *"Space charge distribution in two-layer dielectrics."* Jicables, 2003: p. 154-158.

[86]   P. Morshuis and M. Jeroense, *"Space charge measurements on impregnated paper: A review of the pea method and a discussion of results."* IEEE Eletrical Insulation Magazine, 1997: p. 26-35.

[87]   Y. Sekii, T. Kogure, and T. Maeno, *"Influence of physical properties and peroxide decomposition products on the space charge formation in xlpe and epdm."* IEEE International Conference on Properties and Applications of Dielectric Materials, 1997: p. 132-136.

[88]   K.S. Suh, S.J. Hwang, J.S. Noh, and T. Takada, *"Effects of constituents of xlpe on the formation of space charge."* IEEE Transactions on Dielectrics and Electrical Insulation, 1994: p. 1077-1082.

[89]   K.S. Suh, J.H. Koo, S.H. Lee, J.K. Park, and T. Takada, *"Effects of sample preparation conditions and short chains on space charge formation in ldpe."* IEEE Transactions on Dielectrics and Electrical Insulation, 1996: p. 153-160.

[90] Y. Tanaka, G. Chen, Y. Zhao, A.E. Davies, A.S. Vaughan, and T. Takada, *"Effect of additives on morphology and space charge accumulation in low density polyethylene."* IEEE Transactions on Dielectrics and Electrical Insulation, 2003: p. 113-121.

[91] Y. Tanaka, Y. Li, and T. Takada, *"Space charge distribution in low-density polyethylene with charge-injection suppression layers."* Journal of Physics D: Applied Physics, 1995: p. 1232-1238.

[92] L. Boudou, V. Griseri, I. Guastavino, and L.A. Dissado, *"Effect of temperature on space charge formation in low density polyethylene - role of antioxidant."* IEEE International Conference on Solid Dielectrics, 2004: p. 252-225.

[93] Y. Ohki, N. Hirai, K. Kobayashi, R. Minami, M. Okashita, and T. Maeno, *"Effects of byproducts of crosslinking agent on space charge formation in polyethylene-comparison between acetophenone and α-methylstyrene."* IEEE International Conference on Electrical Insulation and Dielectric Phenomena, 2000: p. 535-538.

[94] S. Agnel, A. Toureille, G. Platbrood, and G. Geerts, *"Study of ac charging ability of xlpe insulation for power cable."* Jicables, 1999: p. 656-661.

[95] C. Bert, C. Heninion, J. Lewiner, C. Alquie, R.N. Hampton, J. Freestone, and S. Verner, *"Measurement of space charge distribution under 50 hz ac stress."* Jicables, 1995: p. 195-199.

[96] Y.L. Chong, H. Miyake, Y. Tanaka, T. Takada, H. Nakama, and G. Chen, *"Space charge in polyethylene under ac electric stress using the pulsed eletroacoustic method."* IEEE International Conference on Electrical Insulation and Dielectric Phenomena, 2004: p. 77-80.

[97]   Y.F.F. Ho, G. Chen, A.E. Davies, R.N. Hampton, S. Hobdell, S.G. Swingler, and S.J. Sutton, *"Space charge measurements in xlpe insulation under 50 hz ac electric stress."* IEE International Conferenece on Dielectric Materials, Measurements and Applications, 2000: p. 68-73.

[98]   Y.F.F. Ho, G. Chen, A.E. Davies, S.G. Swingler, S.J. Sutton, R.N. Hampton, and S. Hobdell, *"Measurement of space charge in xlpe insulation under 50 hz ac electric stress using lipp method."* IEEE Transactions on Dielectrics and Electrical Insulation, 2002: p. 362-370.

[99]   S. Hole, C. Alquie, and J. Lewiner, *"Measurement of space-charge distributions in insulators under very rapidly varying voltage."* IEEE Transactions on Dielectrics and Electrical Insulation, 1997: p. 719-724.

[100]   R. Liu, T. Takada, and N. Takasu, *"Pulsed electro-acoustic method for measurement of space charge distribution in power cables under both dc and ac electric fields."* Journal of Physics D: Applied Physics, 1993: p. 986-993.

[101]   G.C. Montanari, F. Palmieri, G. Mazzanti, C. Laurent, and G. Teyssedre, *"Ac charge injection investigated by means of space charge measurements: Threshold and frequency dependence."* IEEE International Conference on Properties and Applications of Dielectric Materials, 2003: p. 895-899.

[102]   P. Notingher, A. Toureille, J. Sanatana, and M. Albertini, *"Space charge in ac-poled xlpe for hv cables."* Jicables, 1999: p. 701-706.

[103]   P. Notingher, A. Toureille, J. Sanatana, L. Martinotto, and M. Albertini, *"Study of space charge accumulation in polyolefins submitted to ac stress."* IEEE Transactions on Dielectrics and Electrical Insulation, 2001: p. 972-984.

[104]   T. Takada and T. Sakai, *"Measurement of electric field at a dielectric/electrode interface using an acoustic transducer technique."* IEEE Transactions on Electrical Insulation, 1983: p. 619-628.

[105] T. Maeno, T. Hoshino, T. Futami, and T. Takada, "*Application of ultrasonic techniques to the measurement of spatial charge and electric field distributions in solid materials.*" Electrical Engineering in Japan, 1989: p. 58-64.

[106] M. Fu, G. Chen, A.E. Davies, and J. Head, "*Space charge measurements in cables using the pea method - signal data processing consideration.*" IEEE International Conference on Solid Dielectrics, 2001: p. 219-222.

[107] K. Matsui, Y. Tanaka, T. Takada, and T. Maeno, "*Space charge observation in various types of polyethylene under ultra-high dc electric field.*" IEEE International Conference on Solid Dielectrics, 2004: p. 201-204.

[108] T. Takada, K. Murata, and Y. Tanaka, "*Dynamic observation of space charge formation in xlpe using the pulsed electro-acoustic method.*" IEEE International Conference on Electrical Insulation and Dielectric Phenomena, 1996: p. 161-164.

[109] X. Wu, G. Chen, A.E. Davies, Y. Tanaka, S.J. Sutton, and S.G. Swingler, "*Space charge measurements in polyethylene under dc and ac operating conditions using the pea technique.*" IEE International Conference on Dielectric Material Measurement and Applications, 2000: p. 57-62.

[110] T. Maeno, "*Portable space charge measurement system using the pulsed electrostatic method.*" IEEE Transactions on Dielectrics and Electrical Insulation, 2002: p. 331-335.

[111] S. Hole, T. Ditchi, and J. Lewiner, "*Non-destructive methods for space charge distribution measurements: What are the differences?*" IEEE Transactions on Dielectrics and Electrical Insulation, 2003: p. 670-677.

[112] F.N. Lim and R.J. Fleming, "*The temperature dependence of space charge accumulation and dc current in xlpe power cable insulation.*" IEEE International Conference on Electrical Insulation and Dielectric Phenomena, 1999: p. 66-69.

[113] N. Hirai, Y. Maeno, T. Tanaka, Y. Ohki, M. Okashita, and T. Maeno, "*Effect of crosslinking on space charge formation in crosslinked polyethylene.*" IEEE International Conference on Properties and Applications of Dielectric Materials, 2003: p. 917-920.

[114] X. Wu, D. Tu, Y. Tanaka, T. Muronaka, T. Takada, C. Shinoda, and T. Hashizume, "*Space charge in xlpe power cable under dc electrical stress and heat treatment.*" IEEE Transactions on Dielectrics and Electrical Insulation, 1995: p. 467-474.

[115] A.S. Vaughan, Y. Zhao, L.L. Barre, S.J. Sutton, and S.G. Swingler, "*On additives, morphological evolution and dielectric breakdown in low densitiy polyethylene.*" European Polymer Journal, 2003: p. 355-365.

[116] J.F. Shackelford, "*Introduction to material science for engineers.*" 1996: Prentice Hall.

[117] I.L. Hosier, A.S. Vaughan, and S.G. Swingler, "*Structure-property relationships in polyethylene blends: The effect of morphology on electrical breakdown strength.*" Journal of Material Science, 1997: p. 4523-4531.

[118] S. Mitusmoto, M. Nagao, and M. Kosaki, "*Effect of acetophenone on high-field electrical properties in polyethylene.*" IEEE International Conference on Electrical Insulation and Dielectric Phenomena, 1996: p. 157-160.

[119] S. Mitusmoto, M. Nagao, and M. Kosaki, *"High field conduction and space charge distribution in acetophenone-coated polyethylene film."* IEEE International Conference on Properties and Applications of Dielectric Materials, 1997: p. 806-809.

[120] N. Nibbio, T. Uozumi, N. Yasuda, and T. Fukui, *"The effect of additives on space charge in xlpe insulation."* IEEE International Symposium on Electrical Insulation, 1994: p. 559-562.

[121] K. Kobayashi, T. Ohara, Y. Ohki, and T. Maeno, *"Effect of acetophenone on the space charge evolution in ldpe and lldpe."* IEEE International Conference on Electrical Insulation and Dielectric Phenomena, 1999: p. 27-31.

[122] T. Tsurimoto, S. Mitsumoto, M. Nagao, and M. Kosaki, *"Effect of acetophenone on electric conduction in ldpe film."* IEEE International Symposium on Electrical Insulating Materials, 1995: p. 267-270.

[123] L. Markey, G.C. Stevens, L.A. Dissado, and G.C. Montanari, *"Multi-stress electrical and thermal ageing of hv extruded polymeric cables: Mechanisms and methods."* IEE International Conference on Dielectric Material Measurement and Applications, 2000: p. 413-418.

[124] Y. Tanaka, T. Takada, C. Shinoda, and T. Hashizume, *"Temperature dependence of space charge distribution in xlpe cable."* IEEE International Conference on Electrical Insulation and Dielectric Phenomena, 1994: p. 334-339.

[125] T. Kanno, T. Uozumi, and Y. Inoue, *"Measurement of space charge distribution in xlpe cable insulation at high temperature."* IEEE International Symposium on Electrical Insulation, 1998: p. 85-88.

[126]   J. Holboll, M. Henriksen, and J. Hjerrild, "*Space charge build-up in xlpe-cable with temperature gradient.*" IEEE International Conference on Electrical Insulation and Dielectric Phenomena, 2000: p. 157-160.

[127]   G.C. Montanari, G. Mazzanti, F. Palmieri, G. Perego, and S. Serra, "*Dependence of space-charge trapping threshold on temperature in polymeric dc cables.*" IEEE International Conference on Solid Dielectrics, 2001: p. 81-84.

[128]   M. Fu and G. Chen, "*Space charge measurement in xlpe cable with temperature gradient through the insulation.*" IEEE International Conferenece on Electrical Insulation and Dielectric Phenomena, 2003: p. 217-220.

[129]   M. Fu and G. Chen, "*The effect of voltage reversal and elevated temperature on space charge behaviour in xlpe cable.*" Jicables, 2003: p. 491-495.

[130]   M. Fukuma, M. Wadamori, M. Nagao, M. Kosaki, K. Fukunaga, and T. Maeno, "*Short interval space charge and external circuit current measurements in ldpe film in high temperature region.*" IEEE International Symposium on Electrical Insulation, 2001: p. 497-500.

[131]   W.S. Lau and G. Chen, "*The influence of temperature on electrical conduction and space charge in ldpe.*" Jicables, 2003: p. 485-490.

[132]   G. Mazzanti, G.C. Montanari, and J. Alison, "*A space-charge based method for estimation of apparent mobility and trap depth as markers for insulation degradation - theoretical basis and experimental validation.*" IEEE Transactions on Dielectrics and Electrical Insulation, 2003: p. 187-197.

[133]   G. Mazzanti, G.C. Montanari, and F. Palmieri, "*Quantities extracted from space-charge measurements as markers for insulation ageing.*" IEEE Transactions on Dielectrics and Electrical Insulation, 2003: p. 108-203.

[134] G.C. Montanari and D. Fabiani, *"Examination of dc insulation performance based on space charge measurement and accelerated life tests."* IEEE Transactions on Dielectrics and Electrical Insulation, 2000: p. 322-328.

[135] G. Chen, M. Fu, X.Z. Liu, and L.S. Zhong, *"Ac ageing and space charge characteristics in low density polyethylene polymeric insulation."* Journal of Applied Physics, 2005.

[136] Y.L. Chong, G. Chen, H. Miyake, Y. Tanaka, and T. Takada, *"Effect of ac ageing on space charge evolution in xlpe."* IEEE International Conference on Electrical Insulation and Dielectric Phenomena, 2004: p. 81-84.

[137] M. Fu, G. Chen, and X.Z. Liu, *"Space charge behaviour in ldpe afer ac ageing."* IEEE International Conference on Solid Dielectrics, 2004: p. 217-220.

[138] M.P. Cals, J.P. Marques, and C. Alquie, *"The pressure-pulse method for measuring space-charge distribution in irradiated insulators."* IEEE Transactions on Electrical Insulation, 1989: p. 999-1003.

[139] M.P. Cals, J.P. Marques, and C. Alquie, *"Application of the pressure wave propagation method to the study of interfacial effects in the e-irradiated polymer films."* Journal of Applied Physics, 1992: p. 1940-1951.

[140] F. Chapeau, C. Alquie, and J. Lewiner, *"The pressure wave propagation method for the analysis of insulating materials: Application to ldpe used in hv cables."* IEEE Transactions on Electrical Insulation, 1986: p. 405-410.

[141] F. Chapeau, C. Alquie, J. Lewiner, H. Auclair, and R. Jocteur, *"Influence of the manufacturing process of ldpe on the build up of a space charge distribution under electric stress."* IEEE International Conference on Electrical Insulation and Dielectric Phenomena, 1986: p. 180-185.

[142] G. Chen, T.Y.G. Tay, A.E. Davies, Y. Tanaka, and T. Takada, *Electrodes and charge injection in low-density polyethylene.*" IEEE Transactions on Dielectrics and Electrical Insulation, 2001: p. 867-873.

[143] N. Hirai, R. Minami, K. Shibata, Y. Ohki, M. Okashita, and T. Maeno, *"Effect of byproducts of dicumyl peroxide on space charge formation in low-density polyethylene.*" IEEE International Conference on Electrical Insulation and Dielectric Phenomena, 2001: p. 478-483.

[144] N. Hirai, R. Minami, T. Tanaka, Y. Ohki, M. Okashita, and T. Maeno, *"Chemical group in crosslinking by-products responsible for charge trapping in polyethylene.*" IEEE Transactions on Dielectrics and Electrical Insulation, 2003: p. 320-329.

[145] Y. Li, J. Kawai, Y. Ebinuma, Y. Fujiwara, Y. Ohki, Y. Tanaka, and T. Takada, *"Space charge behavior under ac voltage in water-treed pe observed by the pea method.*" IEEE Transactions on Dielectrics and Electrical Insulation, 1997: p. 52-57.

[146] T. Nakatsuka, T. Takahashi, H. Miyata, A. Yokoyama, I. Ishikawa, and T. Niwa, *"The effect of dielectric loss of polyethylene caused by acetophenone and cumylalcohol.*" IEEE International Symposium on Electrical Insulation, 1994: p. 574-577.

[147] G.C. Montanari, G. Mazzanti, E. Boni, and G. De Robertis, *"Investigating ac space charge accumulation in polymers by pea measurements.*" IEEE International Conference on Electrical Insulation and Dielectric Phenomena, 2000: p. 113-116.

[148] G. Mazzanti, G.C. Montanari, and L.A. Dissado, *"A space-charge life model of the ac electrical ageing of polymers.*" IEEE Transactions on Dielectrics and Electrical Insulation, 1999: p. 864-875.

[149] N. Hozumi, T. Takeda, H. Suzuki, and K. Okamoto, *"Space charge behavior in xlpe cable insulation under 0.2-1.2 mv/cm dc field."* IEEE Transactions on Dielectrics and Electrical Insulation, 1998: p. 82-90.

[150] M. Meuier and N. Quirke, *"Molecular modelling of electron trapping in polymer insulators."* Journal of Applied Physics, 2000: p. 369-376.

[151] M. Meuier and N. Quirke, *"Molecular modeling of electron traps in polymer insulators: Chemical defects and impurities."* Journal of Chemical Physics, 2001: p. 2876-2881.

Appendix A
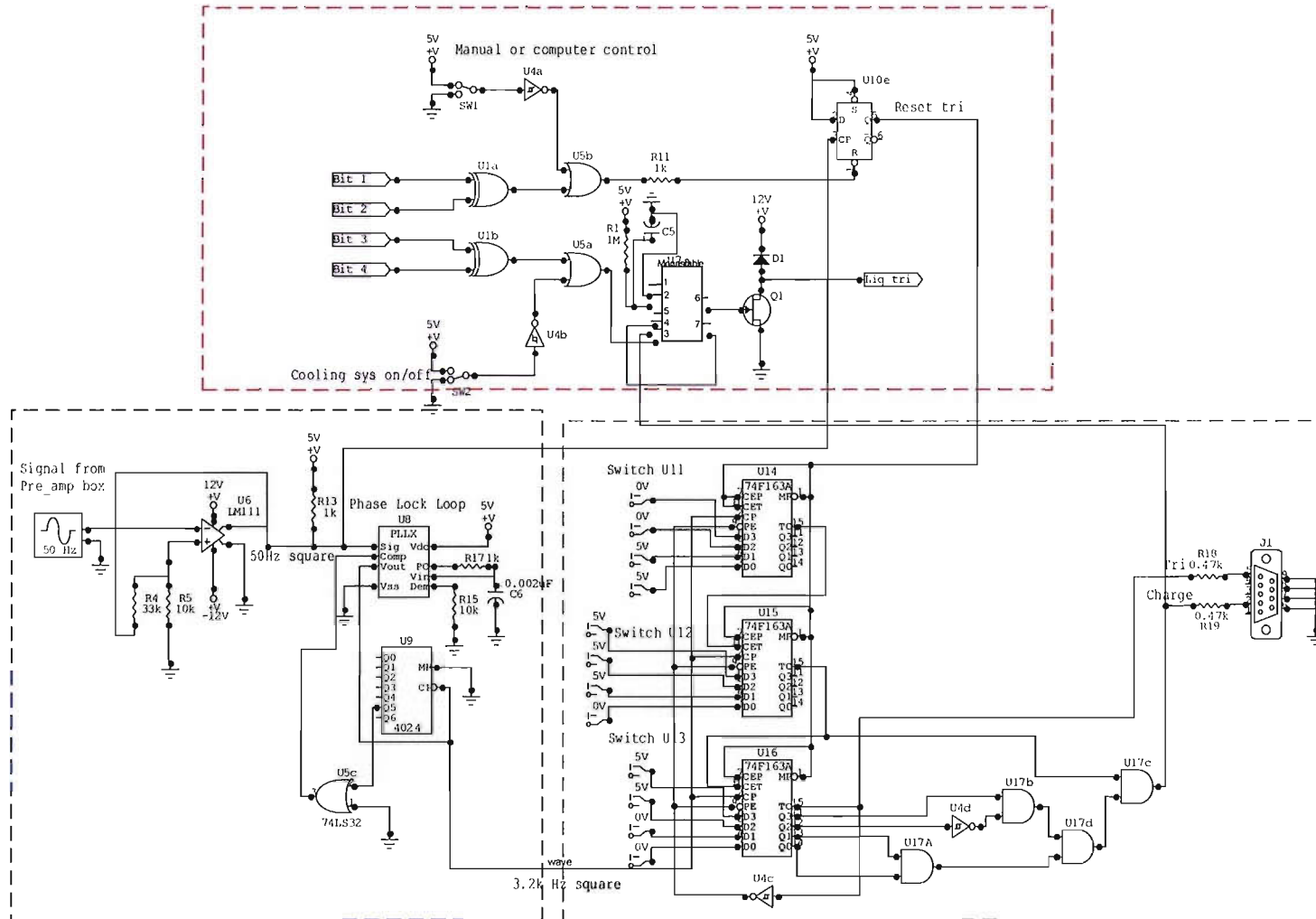
Appendix B

Polyolefins
Superclean™ XL4201S
Natural Crosslinkable Polyethylene with Improved Additive System for High Voltage Power Cable Insulation

Description
Superclean XL4201S is a natural crosslinkable low-density polyethylene compound developed especially for the insulation of high voltage power cables. It provides an excellent balance of a non-staining additive system with improved compatibility, which ensures thermal stability and ease of processing.

Applications
Superclean XL4201S is intended for the insulation of high voltage power cables, i.e. above 66 kV, or for corresponding voltage stresses in non-concentric constructions.

Specifications
Superclean XL4201S meets the applicable requirements as below when processed using sound extrusion practice and testing procedure:

- AEIC CS 5-94 (10th edition)*
- AEIC CS 7-93 (3rd edition)*
- BS 6622
- DIN VDE 0207, 2XI1
- DIN VDE 0263
- DIN VDE 0276-620/A2
- HD 620 S1, Part 1, table 2A, DIX 3 to 14
- IEC 60502
- IEC 60840
- ISO 1872-PE, KHNX, 23-D022
- NEMA WC 7-1996/ICEA S-95-658
- NF C 33-223

* "2 % certification" upon request

Superclean is a trademark of Borealis A/S

Borealis A/S
Lyngby Hovedgade 96
DK-2800 Kongens Lyngby (Denmark)
Telephone: +45 45 96 60 00
Fax : +45 45 96 61 23
www.borealisgroup.com

BOREALIS

Polyolefins
Superclean™ XL4201S

Physical Properties

		Typical Value*	Unit	Test Method
Density	(Base Resin)	922	kg/m^3	ISO 1872-2/ISO 1183-D
Melt Flow Rate, Base Resin	(190°C, 2.16 kg)	2	g/10 min	ISO 1133
Tensile Strength	(250 mm/min)	>17	MPa	ISO 527
Elongation	(250 mm/min)	>450	%	ISO 527
Change of Tensile Properties				
after ageing 135°C, 500 h**		<20	%	IEC 60811-1-2
Hot Set Test	(200°C, 0.20 MPa)			
Elongation under Load		75	%	IEC 60811-2-1
Permanent Deformation		5	%	IEC 60811-2-1
Monsanto Rheometer Value***		30 - 38	dNm	ASTM D 2084
Göttfert Elastograph Value***		0.59 - 0.74	Nm	ISO 6502
Methanol Wash	(max 1500)	800	ppm	BTM00118
Moisture	(max 200)	100	ppm	Karl Fischer-titration

*   Data should not be used for specification work
**   Measured on crosslinked specimen
***   Monsanto Rheometer value is reported for material produced in Belgium and USA
    Göttfert Elastograph value is reported for material produced in Sweden

Electrical Properties

		Typical Value*	Unit	Test Method
Dielectric Constant	(50 Hz)	<2.3	–	IEC 60250
Dissipation Factor	(50 Hz)	<0.0005	–	IEC 60250
DC Volume Resistivity		>10^{16}	Ω cm	IEC 60093
Dielectric Strength	(50 Hz)	>22	kV/mm	IEC 60243

*   Data should not be used for specification work

Processing Guidelines

Borealis crosslinkable grades for power cable insulation provide excellent surface finish and high output rates over a broad range of conditions. Optimum results are normally achieved at a melt temperature of approximately 130°C. Normally no screen-pack is used. For start-up it is recommended that **LE4900** is used until stable extruder conditions are obtained.

BOREALIS

University
of Southampton

School of Electronics and Computer Science

Polyolefins
Superclean™ XL4201S

For the very best result it is recommended to use a fines remover installed immediately before the extruder hopper. The transporting air passes through a filter before it is exhausted into the environment. The fines remover, for example a cyclone, shall be positioned so that there is no risk for fines falling from the filter into the hopper.

Specific recommendations for optimising the processing conditions can be determined only when the application and type of equipment are known. Please contact your local Borealis representative for such particulars.

Storage
Storage shall take place indoors at temperatures between 10 - 30°C due to the risk for peroxide sweat-out at lower temperature. Storage time should not exceed 12 months.

Delivery
Form: Granules
Package: 1000 kg Octabins (with bottom emptying) - Only ex. Belgium and Sweden
            500 kg Half Size Octabins (with bottom emptying) - Only ex. Belgium
            575 kg Smallbins (with bottom emptying) - Only ex. Sweden
            500 kg Smallbins (with bottom emptying) - Only ex. USA
            22 ton (nominal) Bulk Containers
Label: Superclean XL4201SBE   Ex. Belgium, Antwerpen
            Superclean XL4201SSE   Ex. Sweden, Stenungsund
            Superclean XL4201SUS   Ex. USA, Rockport N.J.

BOREALIS

Polyolefins
Superclean™ XL4201S

Safety
Superclean XL4201S is not classified as a dangerous preparation.

The product is supplied in form of free-flowing granules of approximately 3 - 4 mm size and can be readily handled with commercially available equipment. Handling and transport of the product may generate some dust and fines, which constitute a potential hazard for dust explosion. All metal parts in the system should therefore be properly grounded. Properly designed equipment and good housekeeping will reduce the risk. Check and follow local codes and regulations!

Inhalation of any type of dust should be avoided as it may cause irritation of the respiratory system.

The product is intended for industrial use only. A Safety Data Sheet is available on request. Please contact your Borealis representative for more details on various aspects of safety, recovery and disposal of the product.

BOREALIS

University
of Southampton

School of Electronics and Computer Science

Polyolefins

LE0592

Crosslinkable Semiconductive Shielding Compound for Power Cables

Description

LE0592 is a crosslinkable, semiconductive compound.

LE0592 offers good surface smoothness, extrusion properties and gives good scorch resistance also when triple extruded.

Applications

LE0592 intended for conductor and bonded insulation shielding of medium and high voltage XLPE power cables. **LE0592** is suitable for processing in steam as well as in dry cure process, which utilise high temperatures.

Specifications

LE0592 meets the applicable requirements as below when processed using sound extrusion practice and testing procedure:

- AEIC CS 7-93 (3 rd edition)
- AEIC CS 8-00 (1st edition)
- BS 6622
- DIN VDE 0276-263
- DIN VDE 0276-620
- HD 620 S1
- HD 632 S1
- IEC 60502
- IEC 60840
- ISO 1872-E/BA, KHXY, 23-G200, C40
- NEMA WC 74-2000/ICEA S-93-639
- NF C 33-223/UTE C 33-223 / NF C 33-226

BOREALIS

Polyolefins
LE0592

Physical Properties

		Typical Value*	Unit	Test Method
Density		1135	kg/m³	ISO 1872-2-B/ISO 1183-D
Tensile Strength	(25 mm/min)	22	MPa	ISO 527
Elongation	(25 mm/min)	200	%	ISO 527
Change of Tensile Properties				
after ageing 135°C, 240 h		<20	%	IEC 60811-1-2
Hot Set Test	(200°C, 0.20 MPa)			
Elongation under Load		25	%	IEC 60811-2-1
Permanent Deformation		0	%	IEC 60811-2-1
Gottfert Elastograph Value		1.14-1.38	Nm	ISO 6502
Moisture	(max 1000)	300	ppm	Karl Fischer-titration

Electrical Properties

	Typical Value*	Unit	Test Method
DC Volume Resistivity at			
23°C	<100	Ωcm	ISO 3915
90°C	<1000	Ωcm	ISO 3915

* Data should not be used for specification work

Processing Guidelines

LE0592 provides excellent surface finish and outstanding output rates, when processing conditions are optimised for the actual processing equipment and cable dimension.

Optimal conditions may vary according to the equipment used, but as a guide, temperatures according to the table below are suggested:

Hopper drying* (4 hours)	60°C
Melt temperature	115-125°C

* If possible with dehumidified air under agitation

Storage

Storage shall take place indoors at temperatures between 10°C -30°C due to the risk for peroxide sweat-out at lower temperature. Recommended storage time at customer should not exceed 6 months.

BOREALIS

University
of Southampton

School of Electronics and Computer Science

Polyolefins
LE0592

Delivery

Form: Granules
Package: 700 kg Smallbins (PE-liner with bottom emptying)
           1200 kg Octabins (PE-liner with bottom emptying)

Safety

LE0592 is not classified as a dangerous preparation.

The products are supplied in form of free-flowing granules of approximately 3-4 mm sizes and can be readily handled with commercially available equipment. Handling and transport of the products may generate some dust and fines, which constitute a potential hazard for dust explosion. All metal parts in the system should therefore be properly grounded. Properly designed equipment and good housekeeping will reduce the risk. Check and follow local codes and regulations!

Inhalation of any type of dust should be avoided as it may cause irritation of the respiratory system.

The products are intended for industrial use only. A Safety Data Sheet is available on request. Please contact your Borealis representative for more details on various aspects of safety, recovery and disposal of the product.

Disclaimer

BOREALIS

Polyolefins
LE0592

1. Identification of the substance/preparation and of the company/undertaking

Trade name:	Borealis Polyethylene LE0592
Intended use:	Polymer raw material.
Manufacturer:	Borealis

2. Composition/information on ingredients

The product is a polyethylene copolymer. It contains carbon black (EC No 215-609-9, CAS No 1333-86-4), small amounts of stabiliser, ans small amounts of organic peroxide as cross linking agent. Contains no substance classified as hazardous, in concentrations which should be taken into account according to EC directives.

3. Hazards identification

Health: The product is not classified as a dangerous preparation. However, inhalation of dust may irritate the respiratory tract. Prolonged inhalation of high doses of decomposition products may give headache or irritation of the respiratory tract.

Health: The product is not classified as a dangerous preparation. However, inhalation of dust may irritate the respiratory tract. Prolonged inhalation of high doses of decomposition products may give headache or irritation of the respiratory tract.

Fire: The product burns, but is not classified as flammable.

Environment: The product is not considered dangerous for the environment.

4. First-aid measures

No specific instruction needed.

5. Fire-fighting measures

Suitable extinguishing media: Water in spread jet, dry chemicals, foam or carbon dioxide.

Special exposure hazard: Principal toxicant in the smoke is carbon monoxide.

6. Accidental release measures

Suck or sweep up spill. All spill of granules must be removed immediately to prevent slipping accidents.

7. Handling and storage

During processing and thermal treatment of the product, small amounts of volatile hydrocarbons may be released. Provide adequate ventilation. Local exhaust ventilation may be necessary.

Avoid inhalation of dust and decomposition fumes.

Dust from the product gives a potential risk for dust explosion. All equipment shall be grounded. No other specific storage requirements.

BOREALIS

Polyolefins
LE0592

8. Exposure controls / personal protection
Provide adequate ventilation. Local exhaust ventilation may be necessary.

9. Physical and chemical properties
Appearance: Solid granules, odourless. **Color:** Black

Melting point: 110-140 ºC Ignition temperature: > 300 ºC
Density: 1. g/cm^3 Solubility: insoluble in water.

10. Stability and reactivity
The product is a stable thermoplastic, with no chemical reactivity.

11. Toxicological information
The product is not classified as a dangerous preparation according to Directive 1999/45/EC. However, inhalation of dust may irritate the respiratory tract. Prolonged inhalation of high doses of decomposition products may give headache or irritation of the respiratory tract.
Carbon Black has a workplace exposure limit in some European countries, but is not classified as dangerous. Exposure to Carbon Black is not likely, as it is embedded in a solid polymer.

12. Ecological information
The product is not considered dangerous for the environment.

13. Disposal considerations
Reuse or recycle if not contaminated. The product may be safely used as fuel or landfilled. Proper combustion does not require any special flue gas control. No leachate is generated in landfills. Check with local regulations.

14. Transport information
The product is not regulated by ADR/RID, IMDG or IATA.

15. Regulatory information
Label; Trade name: Borealis Polyethylene LE0592

16. Other information
Issuer: Borealis Group HSE/Niri Orlien, according to directive 91/155/EEC and its amendments.

Appendix C

Diffusion equation

Diffusion equation is also known as heat equation. Below shows the derivation of the heat equation as it is easier to understand the equation in terms of heat transfer.

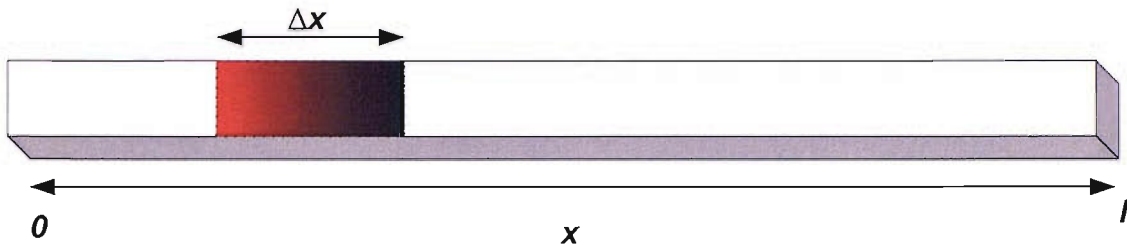Consider a thin homogeneous bar of length l as shown in figure 1.

Figure 1: Thin bar of length l.

Assume that the thickness of the sample is much smaller the length, we can postulate that temperature of the bar does not vary with thickness. The temperature of the bar at position x and time t can be described as:

$\tau(x,t)$ where $0 \leq x \geq l$ and $t \geq 0$

Assuming that at each point of the bar the energy density per unit volume e is proportional to the temperature, i.e.

$$e(x,t) = c(x)\,\tau(x,t) \tag{1}$$

where $c(x)$ is the heat capacity and where the mass density is assumed to be constant throughout the body and normalised to one.

In order to derive the homogeneous heat conduction equation, we assume that there are no internal sources of heating along the bar and that heat can only enter the bar through its end (i.e. we assume that the lateral surface of the bar is perfectly insulated).

By law of conservation which states that the rate of change of energy in any finite part of the bar is equal to the total amount of heat flowing into that part of the bar. Let $q(x,t)$ denote the heat flux (rate of heat flows through the body) at position x and time t and consider the portion of the bar from x to $x + \Delta x$. The rate of change of the total energy of this part of the bar equals the total amount of heat that flows into this part through its ends,

$$\frac{\partial}{\partial t} \int_{x}^{x+\Delta x} c(z)\theta(z,t)dz = -q(x+\Delta x,t) + q(x,t) \tag{2}$$

where the heat flux $q(x,t)$ is greater than zero if the flow is to the right side of the bar.

To obtain the equation that describe the heat conduction at any point x, we shall consider the limit of equation 2 as $\Delta x \rightarrow 0$. First assuming that the integrand $c(z)\theta(z,t)$ is sufficiently regular so that we are able to differentiate inside the integral. Second, dividing both sides of the equation by Δx, invoking the Mean-Value Theorem for integrals and taking $\Delta x \rightarrow 0$ we obtain the equation

$$c(x)\frac{\partial\theta}{\partial t} = -\frac{\partial q}{\partial x} \tag{3}$$

relating the rate of change of temperature with the gradient of the heat flux. Further assume that the heat flows at the rate directly proportional to the (spatial) rate of change of temperature and accepting that the heat flows from hot to cold we get

$$q(x,t) = -k(x)\frac{\partial\theta}{\partial x} \tag{4}$$

where $k(x) > 0$ is the thermal conductivity. The choice of the sign in the definition of the heat flux guarantees that if the temperature is increasing with x the heat flux is negative and the heat flows from right to left (or hot to cold).

Combining equations 3 and 4,

$$c(x)\frac{\partial\theta}{\partial t} = \frac{\partial}{\partial x}(k(x)\frac{\partial\theta}{\partial x}) \,, \quad 0 < x < l \tag{5}$$

which govern the heat flow in an inhomogeneous (k is point dependent) one dimensional body. However, if the bar is made of the same material throughout whereby the heat capacity c(x) and the thermal conductivity k(x) are point independent, equation 5 simplifies to

$$\frac{\partial\theta}{\partial t} = \gamma\frac{\partial^2\theta}{x^2}, \quad 0 < x < l \tag{6}$$

where $\gamma = \dfrac{k}{c}$ is known as the diffusion coefficient.

which is the one dimensional diffusion equation.

Solving the diffusion equation by separation of variables

Let $\theta(z,t) = T(t)u(x)$ \hfill (7)

Combining equations 6 and 7

$$\frac{\partial T(t)u(x)}{\partial t} = \gamma\frac{\partial^2(t)u(x)}{\partial x^2}$$
$$\frac{T(t)'}{T(t)} = \gamma\frac{u(x)''}{u(x)} = -\lambda \tag{8}$$

Let $T = Vt$

$$T(t) = V + t\frac{\partial V}{t}$$

From equation 3

$$\frac{1}{T}T(t)' = -\lambda$$

$$\frac{1}{Vt}(V + t\frac{\partial V}{\partial t}) = -\lambda$$

$$\frac{1}{t} + \frac{\partial V}{V \partial t} = -\lambda$$

$$\frac{\partial V}{V \partial t} = -\lambda - \frac{1}{t}$$

$$\int \frac{\partial V}{V} = \int (-\lambda - 1/t)\partial t$$

$$\ln V + A = -\lambda t - \ln t + C$$

taking exponential on both sides

$$AV = \frac{C}{t}\exp(-\lambda t)$$

Since $V = \dfrac{T}{t}$

$$AT = C\exp(-\lambda t)$$

Taking the initial condition $T(0) = 1$

$$AT(0) = C\exp(-0.\lambda)$$
$$\therefore A = C$$

Hence

$$T(t) = \exp(-\lambda t) \tag{9}$$

Substitute equation 9 into equation 7

$$\theta(x,t) = u(x)\exp(-\lambda t) \tag{10}$$

From equation 8

$$\gamma \frac{u(x)''}{u(x)} = -\lambda$$

$$u(x)'' = -\frac{\lambda}{\gamma} u(x)$$

$$u(x)'' + w^2 u(x) = 0$$

where $w^2 = \frac{\lambda}{\gamma}$

which is a simple harmonic motion equation and has the general solution

$$u(x) = a\cos(wx) + b\sin(wx) \tag{11}$$

Therefore the solution for the diffusion equation can be obtained by substituting (11) into (10)

$$\theta(x,t) = [a\cos(wx) + b\sin(wx)]\exp(-\lambda t) \tag{12}$$

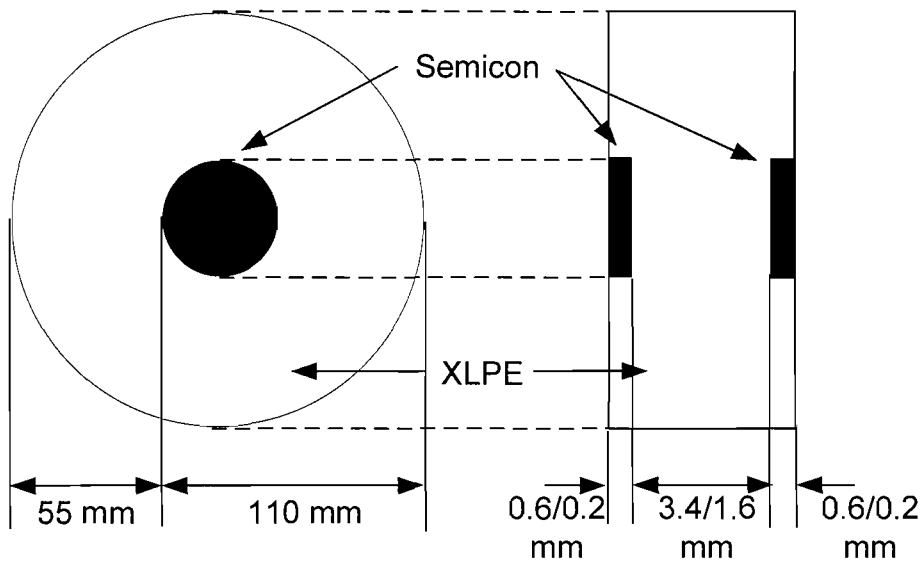The geometry of XLPE planar sample used is shown in figure 2

Figure 2: Geometry of XLPE sample

For the purpose of modeling the diffusion process of crosslinked by-products, the sample can be categorized into two parts, namely, with and without semicon electrodes. Both has to be solved individually and the multiply by factors according to their volume proportion. As seen in figure 2, the surface area of the sample is big

compared to its thickness, thus diffusion of crosslinked by-products through the sides is assumed to be relatively insignificant.

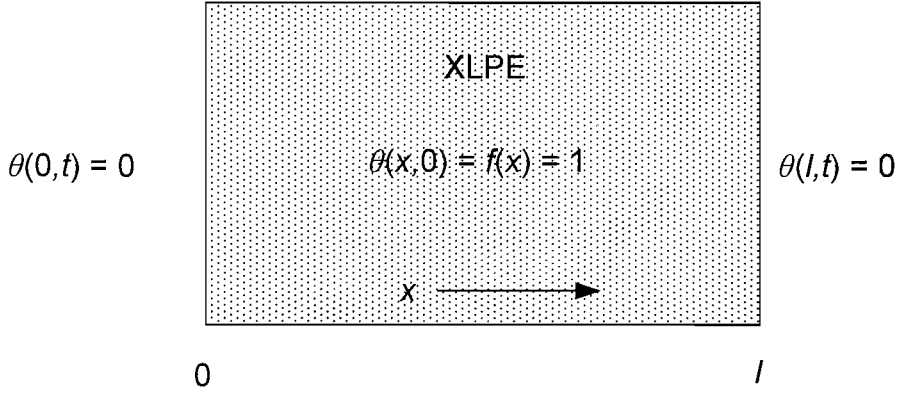First, consider the part without semicon electrodes.

$\theta(0,t) = 0$ ⟨XLPE⟩ $\theta(x,0) = f(x) = 1$ $\theta(l,t) = 0$

Figure 3: Part of XLPE sample without semicon electrodes

As $\theta(0,t) = \theta(l,t) = 0$, $t \geq 0$,

For this to hold true,

$u(0) = u(l) = 0$

from equation 11

$u(x) = a\cos(wx) + b\sin(wx) = 0$

Consider $u(0) = 0$

$u(0) = a\cos(0) + b\sin(0) = 0$

$\therefore a = 0$

Consider $u(l) = 0$

$u(l) = 0\cos(wl) + b\sin(wl) = 0$

$u(l) = \sin(wl) = 0$ wl must be multiple integer of π

$\therefore ui(l) = \sin\dfrac{n\pi}{l}x$ where $n = 1,2,3,4,....$

Linear superposition of these basic solution into the diffusion equation yields

$$\theta(x,t) = \sum_{n=0}^{\infty} B_n \sin \frac{n\pi}{l}x \ \exp -\frac{\gamma n^2 \pi^2}{l^2}t \tag{13}$$

Applying the initial condition

$$\theta(x,0) = \sum_{n=0}^{\infty} B_n \sin \frac{n\pi}{l} x = f(x) = 1$$

which is a Fourier sine series where

$$B_n = \frac{2}{l} \int_0^l f(x) \sin \frac{k\pi}{l} x dx \tag{14}$$

From equation 14

$$
\begin{aligned}
B_n &= \frac{2}{l} \int_0^l f(x) \sin \frac{k\pi}{l} x.dx \\
&= \frac{2}{l} \int_0^l \sin \frac{k\pi}{l} x.dx \\
&= \frac{2}{l} \left[-\frac{l}{n\pi} \cos \frac{n\pi}{l} x \right]_0^l \\
&= -\frac{2}{n\pi} \left[\cos(n\pi) - 1 \right]
\end{aligned}
$$

$$\therefore B_n = \frac{2}{n\pi} \left[1 - \cos(n\pi) \right]$$

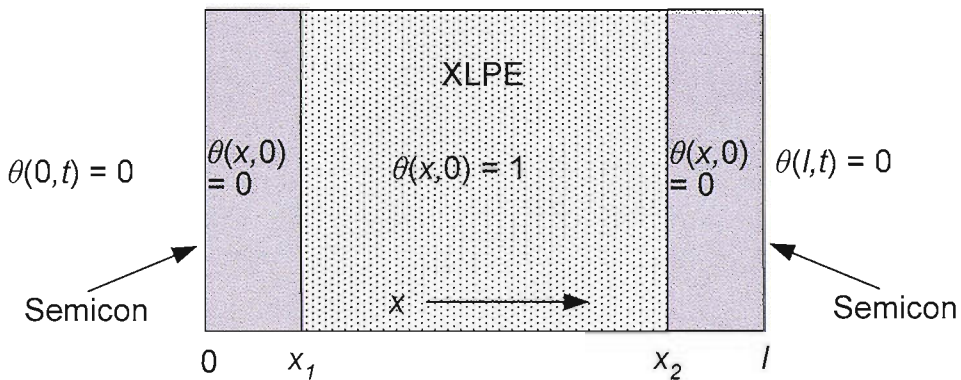Next consider the part of the sample with semicon electrodes

Figure 4: Part of XLPE sample with semicon electrodes

For simplicity, two assumptions were made

1)   diffusion coefficient γ of semicon and XLPE are equal

2)   amount of byproducts in semicon before hotpressed into XLPE is negligible

Using the general solution of the diffusion equation as used before

$$\theta(x,t) = \sum_{n=0}^{\infty} B_n \sin \frac{n\pi}{l} x \ \exp \ -\frac{\gamma n^2 \pi^2}{l^2} t$$

However, due to the semicon electrodes, the B_n now becomes

$$Bn = \frac{2\{x_1 \cos x_1 n\pi - x_2 \cos x_2 n\pi\}}{n\pi}$$